



Ben-Gurion University of the Negev
The Faculty of Natural Sciences
The Department of Geological and Environmental Sciences

Modeling the Excavation Sequence with the Numerical Manifold Method (NMM)

Thesis Submitted in Partial Fulfillment of the Requirements for the
M.Sc. Degree in the Faculty of Natural Sciences

By Yuval Tal

February 6, 2012

יג בשבט, תשע"ב

Ben-Gurion University of the Negev
The Faculty of Natural Sciences
The Department of Geological and Environmental Sciences

Modeling the Excavation Sequence with the Numerical Manifold Method (NMM)

Thesis Submitted in Partial Fulfillment of the Requirements for the
M.Sc. Degree in the Faculty of Natural Sciences

Yuval Tal

Under the Supervision of Prof. Yossef Hodara Hatzor

Signature of student:_____

Date:_____

Signature of supervisor:_____

Date:_____

Signature of chairperson of the
committee for graduate studies:_____

Date:_____

February 2012

Abstract

This research focuses on the application and modification of the numerical manifold method (NMM) for the purpose of enhancing the analysis capability of underground openings embedded in discontinuous rock masses. As a hybrid method between numerical methods from the continuum (FEM) and discontinuum (DDA) approaches, the NMM is capable of modeling dynamic problems involving the interaction of multiple blocks including the stress distribution and deformations inside those blocks.

The NMM is verified using four analytical solutions. In three static problems, the NMM program capability of accurately solving the stresses and displacements in a homogeneous elastic domain (circular hole in an infinite plate and beam under concentrate load and volumetric force) and in inhomogeneous elastic domain (layered plate) is verified. In one dynamic problem, the NMM program ability to model frictional contacts between two blocks (block on an incline) is verified. A good agreement between the NMM and the analytical solutions is obtained.

In this work the original NMM is modified in order to improve its capability of analyzing the stability of underground openings in blocky rock masses. An algorithm for a two-stage procedure is implemented into the NMM code in order to allow tunnel excavation during the NMM simulation, after the local stresses in the medium already exist and the medium has already experienced elastic deformation due to overburden stress.

The importance of analyzing underground opening stability with the modified NMM, where the underground opening is excavated during the simulation, is demonstrated with an example of rectangular underground opening embedded in horizontally stratified and vertically jointed rock mass. When analyzed with the modified NMM, the underground opening is stable when the discontinuities' friction angle is 15° and above, while with the original NMM, stability is achieved only at friction angles of 30° and above.

The original and modified NMM are applied in this thesis to analyze the stability of the 30 m span "Freemasons hall" at Zedekiah cave which is embedded in a blocky rock mass. Stability analysis with an experimentally obtained friction angle value of 41° reveals that the rock mass above the cavern attains stable arching after small initial vertical deflection of the immediate roof. Stability analyses of the studied opening with significantly smaller values of friction angles lend support to the conclusion that cavern is stable in its current configuration: with the modified NMM the cavern is stable when the discontinuities' friction angle is 15° and above, while with the original NMM the cavern is stable when the discontinuities' friction angle is 25° and above.

Acknowledgements

Prof. Yossi Hatzor is thanked for his appreciated mentoring, personal involvement, and for being patient and open minded to every idea.

Dr. Gen-hua Shi is thanked for providing his latest version of NMM (2010) with its open computer code.

Dagan Bakun-Mazor is thanked for helping with computer softwares such as Endnote and Grapher, and also for some good advices.

Avishay Krif is thanked for solving any computer problem I had.

My colleagues in the lab Gony, Elchannan, Guy, Ksenia and Yael are thanked for enjoyable lunches together, and for giving help when needed.

Part of this project was funded by Israel Science Foundation through contract No. ISF – 2201- 556/08.

Finally, I would like to thank to my wife Irit, for her love, support and care, and for her patient throughout the long hours I spent in front of the computer.

Table of contents

Abstract.....	1
Acknowledgements	2
Chapter 1- Introduction	11
1.1 Observational methods	11
1.2 Numerical methods.....	11
1.2.1 Continuum methods.....	12
1.2.2 Discrete Element Methods (DEM)	13
1.3 The Numerical Manifold Method.....	14
1.4 Research Objectives	15
1.5 Thesis organization.....	16
Chapter 2- Scientific Background: Review of NMM principals.....	17
2.1 NMM finite cover system.....	17
2.1.1 Mathematical cover and weighting functions:.....	17
2.1.2 Physical cover and local function	19
2.1.3 Manifold elements and global displacement function	21
2.2 Global equations of equilibrium	23
2.3 Continuous material contribution to the global equations of equilibrium.....	23
2.3.1 Stiffness matrix:.....	23
2.3.2 Initial stress matrix:	25
2.3.3 Point load matrix	26
2.3.4 Body force matrix	26
2.3.5 Inertia force matrix	27
2.3.6 Fixed point matrix	29
2.4 Adding discontinuities to the global equations of equilibrium.....	29
2.4.1 Contacts detection and definition	30
2.4.2 Entrance Lines of Contacts.....	31
2.4.3 Shear Contact Matrix.....	35
2.4.4 Friction force matrix	38
2.5 Two dimensional simplex integration	39
2.6 Equation solver and open-close iteration for equilibrium equations	40
2.7 NMM numeric implementation	41
Chapter 3- Numerical code verification	42
3.1 Layered plate subjected to gravity	42
3.1.1 Analytical solution:	43
3.1.2 Analytical versus NMM solution	45
3.2 Kirsch solution.....	48
3.2.1 Analytical solution.....	49

3.2.2 Analytical versus NMM solutions	49
3.3 Beam under concentrate load and volumetric force	53
3.3.1 Analytical solution.....	53
3.3.2 Analytic versus NMM solutions.....	54
3.4 Dynamic sliding of a block on an incline	57
3.4.1 Analytical solution.....	58
3.4.2 Analytical versus NMM solutions.....	58
3.4.3 Average number of iterations per time step and total time of simulation	62
3.5 Summary and conclusions	64
Chapter 4- Simulating the excavation sequence.....	67
4.1 Model geometry and mechanical properties.....	67
4.2 Numerical control parameters calibration	68
4.2.1 Accuracy of the numerical results at the end of the first static stage	69
4.2.2 Average number of open-close iterations per time step	73
4.2.3 Computing time (CPU time)	74
4.2.4 Final selection of the numerical control parameters.....	75
4.3 Results	76
4.3.1 Original versus modified NMM	76
4.3.2 Analysis of a single block behavior during the simulation	79
4.4 Summary.....	82
Chapter 5- The Zedekiah cave case study	84
5.1 Site description	84
5.2 NMM model	86
5.3 NMM simulations.....	87
5.3.1 Friction angle value of 41°	88
5.3.2 Required friction angle for stability.....	89
5.4 Summary.....	92
Chapter 6- Discussion and conclusions	93
6.1 Verification and calibration of the NMM.....	93
6.2 Simulating the excavation sequence with NMM.....	94
6.3 Recommendations for further research.....	95
References	96

List of Figures

Figure 1.1. Suitability of different numerical methods for an excavation in a rock mass: a) continuum method; b) either continuum with fracture elements or discrete method; c) discrete method; and d) continuum method with equivalent properties (Jing, 2003).....	12
Figure 2.1. The mathematical cover based on triangular finite elements mesh (a) and the weight function of a hexagonal mathematical cover (b) (after Chen et al. (1998)).	18
Figure 2.2. Triangular element divided to three sub triangles (after An (2010)).	19
Figure 2.3. An example of manifold problem: Rectangular body with vertical discontinuity (a); and NMM model of the problem with triangular finite elements mesh (b).	20
Figure 2.4. Generation of two mathematical covers from a single mathematical cover which holds a discontinuity.	22
Figure 2.5. Types of block contacts: a) angle to angle; b) angle to edge; c) edge to edge; (Modified after Shi (1996a)).	30
Figure 2.6. Contacts in the example problem. The stars represent contacts of physical boundary vertices, and the dots represent contacts of the intersection points of the triangular mesh with physical boundaries.....	30
Figure 2.7. Illustration of overlapping angle: a) angle to angle; b) angle to edge; (Modified after Shi (1996a)).	31
Figure 2.8. Penetration criterion: vertex entrance line relationship in the beginning of the time step (left hand side), and in the end of the time step (right hand side); (Modified after (Shi, 1996a))......	33
Figure 2.9. Illustration of the shear spring insertion procedure in NMM: contact configuration at a) the beginning of the time step; and b) the end of the time step. The dashed line represents the location of vertex P_1 if a shear spring is not added (Modified after Shi (1996a))......	36
Figure 2.10. Triangulation of manifold element with the sign convection: positive- counterclockwise, negative- clockwise (Modified after Shi (1996b)).	39
Figure 3.1. Layout of the modeled problem consisting of an elastic plate divided into n layers and constrained between stiff boundaries at sides and bottom.	42

Figure 3.2. Layout of the modeled problem consisting of a continuous elastic plate constrained between stiff boundaries at sides and bottom.	43
Figure 3.3. NMM model of Elastic plate divided into 3 sub-layers at the end of the simulation. Typical stress distribution result with scaled principal stress trajectories delineated in red.....	46
Figure 3.4. Comparison between results of analytical and numerical approaches: Vertical and horizontal stresses as a function of measurement point depth.	46
Figure 3.5. Relative errors of the stresses as a function of measurement point depth. The relative error at depth of 0.1 m is absent due figure scale.....	47
Figure 3.6. Comparison between results of analytical and numerical approaches: Vertical displacement as a function of measurement point depth.	47
Figure 3.7. Relative errors of the vertical displacement as a function of measurement point depth. The relative error at the bottom of the model is absent due to figure scale.	48
Figure 3.8. Sign convention for Kirsch solution; (after Brady and Brown (1993)).	48
Figure 3.9. NMM model for continuous elastic plate with a hole in the center with mesh density of 30.....	49
Figure 3.10. Layout of model for continuous elastic plate with a hole in the center under remote vertical stress and vertical stiff boundaries.	50
Figure 3.11 Comparison between results of analytical and numerical approaches: Vertical and horizontal stresses as a function of the vertical distance above the center of the hole normalized by the hole's radius.	51
Figure 3.12. Relative errors of the stresses as a function of the vertical distance above the center of the hole normalized by the hole's radius. The relative error for vertical stress at distance 0f 1 radius above the center is absent due to figure scale.	51
Figure 3.13. Comparison between results of analytical (blue line) and numerical approaches: Vertical displacement due to cavity as a function of the vertical distance above the center of the hole normalized by the hole's radius. The orange diamonds indicate the two simulation procedure, while the purple squares indicate the two stages procedure.	52
Figure 3.14. Relative errors of the vertical displacement with 2 simulation procedure (orange diamonds) and 2 stages procedure (purple squares) as a function of the vertical distance above the center of the hole normalized by the hole's radius.....	53

Figure 3.15. Beam under concentrate load and volumetric force.....	53
Figure 3.16. NMM models of the beams at the end of the simulation for mesh densities of 5, 10, 20 and 40.....	55
Figure 3.17. Comparison between results of analytical (dashed blue line) and NMM: Horizontal stresses as a function of x for mesh densities of 5, 10, 20 and 40.....	56
Figure 3.18. Relative errors of the horizontal stresses as a function of X for densities of 10, 20 and 40 at 7 measurement points (two points at the ends are absent due to figure scale).	56
Figure 3.19. Comparison between results of analytical (dashed blue line) and NMM: Vertical displacements as a function of X for mesh densities of 5, 10, 20 and 40.	57
Figure 3.20. Relative errors of the vertical displacements as a function of X for mesh densities of 10, 20 and 40.....	57
Figure 3.21. Schematic presentation of the forces acting on a single block lying on an incline.	58
Figure 3.22. NMM model of a block on an incline	59
Figure 3.23. Comparison between results of analytical (blue line) and NMM: Block displacement as a function of time for the case of $g_1 = 0.00025$, $g_2 = 0.001$, and $g_0 =$ $5E$	60
Figure 3.24. Relative errors of the displacemen as a function of time for the case of $g_1 =$ 0.00025 s, $g_2 = 0.001$, and $g_0/ E = 5$	60
Figure 3.25. Relative errors of the vertical displacement at $t = 1$ s as a function of g_1 , g_0 , g_2 . The empty symbols represent simulations where the total time of the simulation is lower than 1 s.	61
Figure 3.26. average number of open-close iterations per time step as a function of g_1/ g_2 ratio in all 49 combinations of g_2 and g_1	63
Figure 3.27. Total time of simulation as a function of g_1/ g_2 ratio in all 49 combinations of g_2 and g_1	64
Figure 3.28. Evolution of time step size during the simulation for the case of $g_1 = 0.005$ s, g_2 $= 0.0001$ and $g_0/E = 1$	64
Figure 3.29. Relative location of the three central measurement points (orange dots) inside the elements for mesh densities of $e=10$ and $e=20$	65

Figure 4.1. NMM model of the analyzed opening: a) modified NMM model at the beginning of the simulation; and b) original NMM model at the beginning of the simulation.	68
Figure 4.2. Comparison between results of analytical (dashed blue line) and NMM solutions: horizontal stresses as a function of measurement point depth for assumed maximum displacement ratio of $g_2 = 0.0001$, and g_0/E ratios of 0.1, 0.5, 1, 5 and 10.	70
Figure 4.3. Comparison between results of analytical (dashed blue line) and NMM solutions: vertical stresses as a function of measurement point depth for assumed maximum displacement ratio of $g_2 = 0.0001$, and g_0/E ratios of 0.1, 0.5, 1, 5 and 10.	70
Figure 4.4. Comparison between results of analytical (dashed blue line) and NMM solutions: vertical displacements as a function of measurement point depth for assumed maximum displacement ratio of $g_2 = 0.0001$, and g_0/E ratios of 0.1, 0.5, 1, 5 and 10.	71
Figure 4.5. Root mean square of the horizontal stresses as a function of the ratio g_0/E for maximum displacement ratios of $g_2=0.0001$, $g_2=0.00025$, and $g_2=0.0005$	72
Figure 4.6. Root mean square of the vertical stresses as a function of the ratio g_0/E for maximum displacement ratios of $g_2=0.0001$, $g_2=0.00025$, and $g_2=0.0005$	72
Figure 4.7. Root mean square of the vertical displacements as a function of the ratio g_0/E for maximum displacement ratios of $g_2=0.0001$, $g_2=0.00025$, and $g_2=0.0005$	73
Figure 4.8. Average open-close iterations per time step as a function of g_0/E ratio for maximum displacement ratios of $g_2=0.0001$, $g_2=0.00025$, and $g_2=0.0005$	74
Figure 4.9. Total time of simulation normalized by the planed total time (12.5 s) as a function of g_0/E ratio for maximum displacement ratios of $g_2=0.0001$, $g_2=0.00025$, and $g_2=0.0005$	74
Figure 4.10. Simulation computing time as a function of g_0/E ratio for maximum displacement ratios of $g_2=0.0001$, $g_2=0.00025$, and $g_2=0.0005$	75
Figure 4.11. The analyzed opening at the end of the modified NMM simulations (left hand side), and at the end of the original NMM simulations (right hand side) for friction angles of 10°, 15°, 20°, 25°, 30°, 35° and 40°.....	76
Figure 4.12. The modified NMM model at the end of the simulation with the locations of the analyzed block, and the two measurement points. Typical stress distribution result with scaled principal stress trajectories delineated in red.	80
Figure 4.13. Horizontal stresses at the upper (red) and lower (blue) measurement points as a function of time for simulation with friction angle of $\phi = 30^\circ$ at all discontinuities.....	81

Figure 4.14. Analysis of the three central blocks of the crown at the end of the simulation, including: horizontal stresses distribution and displacements at the central block, and displacements at the lower part of its neighboring blocks.	81
Figure 4.15. Vertical stresses at the upper (red) and lower (blue) measurement points as a function of time for simulation with friction angle of $\phi = 30^\circ$ at all discontinuities.	82
Figure 4.16. Vertical displacements at the upper (red) and lower (blue) points as a function of time for simulation with friction angle of $\phi = 30^\circ$ at all discontinuities.	82
Figure 5.1. The 2000 year old cave of Zedekiah underneath the old city of Jerusalem. a) Layout of Zedekiah cave superimposed on the old city of Jerusalem, b) plan of Zedekiah cave, "Freemasons' Hall" delimited by dashed square, c) A cross section through Freemasons' Hall (after Eimermacher (2004)).	85
Figure 5.2. NMM model of the "Freemasons' Hall"	87
Figure 5.3. a) Schematic illustration of discontinuity tips in NMM mesh; and b) DDA mesh which were generated with the same input data.	87
Figure 5.4. The "Freemasons' Hall" model at the end of the modified NMM simulations (a), and at the end of the original NMM simulations (b). Typical stress distribution result with scaled principal stress trajectories delineated in red.	88
Figure 5.5. The "Freemasons' Hall" model at the end of the modified NMM simulations (left hand side), and at the end of the original NMM simulations (right hand side) for friction angles of 10° , 15° , 20° and 25°	90
Figure 5.6. Roof deflection as a function of time during modified (the graph represents only the second dynamic stage) and original NMM simulations, for friction angles of, 20° and 25°	91

List of Tables

Table 2.1 The physical covers in the NMM model.	20
Table 2.2. Definition of entrance lines in an angle to angle contact when both angles are less than 180° (modified after Shi (1996a)).	32
Table 3.1. Input parameters for NMM verification.	46
Table 3.2. Input parameters for NMM analysis.....	50
Table 3.3. Input parameters for MM analysis.	54
Table 3.4. Input parameters for NMM analysis.....	59
Table 4.1. Input Numerical parameters for NMM analysis.....	69
Table 4.2. Underground opening at the end of the simulations.....	69
Table 5.1. Rock mass structure at Zedekiah cave (after Eimermacher (2004))	86
Table 5.2. Input parameters for NMM analysis of Freemasons' Hall in Zedekiah cave, Jerusalem.....	88

Chapter 1- Introduction

Rock masses are not an ideal material, and may largely be characterized by the acronym " DIANE" (Discontinues, Inhomogeneous, Anisotropic and Non-elastic) (Harrison and Hudson, 2000). In discontinuous rock masses, the intersection of several sets of discontinuities (joints, bedding planes, faults) forms rock blocks. When analyzing the stability of an underground opening embedded in a blocky rock mass, analytical solution are rare, and observational and numerical methods are usually employed.

1.1 Observational methods

In the observational methods, the analyzed rock mass is classified and rated on the basis of mechanical and geometrical parameters such as strength of intact rock, spacing, orientation and condition of discontinuities, water content and local stresses. Then, support design is suggested, based on previous empirical data. The two rock mass classification methods which are mostly used today are the Geomechanics Classification (a.k.a. Rock Mass Rating -RMR) of Bieniawski (1973; Bieniawski, 1989) and the Rock Quality system of Barton et al., (1974). Those methods can be a valuable tool at the early stages of a project: they are simple and can be used as a check-list to ensure that all relevant information has been considered. However, they are general and ignore specific characteristic of the rock mass and project (Riedmüller and Schubert, 1999). Thus, they should be used only for preliminary, planning purposes rather than stability evaluation (Riedmüller and Schubert, 1999) or final tunnel support (Bieniawski, 1997).

1.2 Numerical methods

Numerical methods have been extensively used in the field of rock mechanics in the past several decades due to advances in computing power. An extensive and comprehensive review of techniques and advances in numerical modeling for rock mechanics and rock engineering is presented by Jing (2003), the source on which much of the material in this section is based.

The numerical methods in rock mechanics are classified into two main categories: 1) Continuum methods; and 2) Discrete methods. The choice of continuum or discrete methods depends mainly on the problem scale and fracture system geometry. Figure 1.1 illustrates the alternative choices for different fracture circumstances in rock mechanics problems. Continuum approaches should be used for rock masses with no fractures (Figure 1.1a), or with many fractures where pseudo continuous displacement field is produced (Figure 1.1d).

When a small number of discontinuities divide the medium into a small number of continuous regions (Figure 1.1b), the displacement field will be continuous inside each region but may be discontinuous across the discontinuities. If a continuum model is used, the model should be able to consider the specific discontinuities. The discrete approach is most suitable for moderately fractured rock masses where the number of fractures is too large for continuum approaches, or where large-scale displacements of individual blocks are possible (Figure 1.1c).

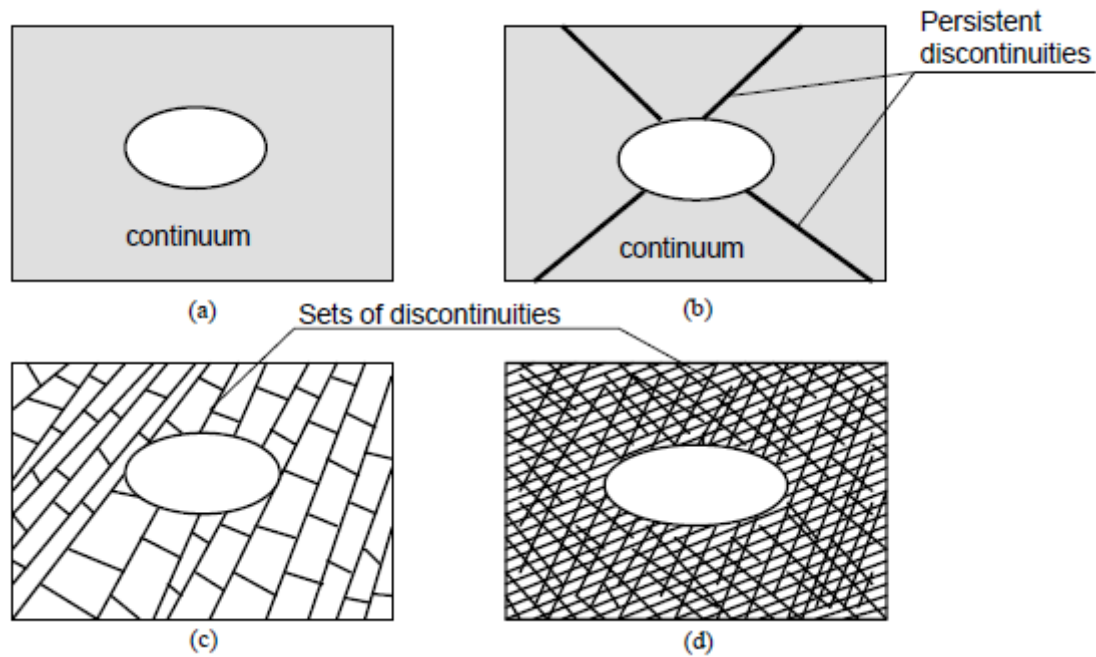


Figure 1.1. Suitability of different numerical methods for an excavation in a rock mass: a) continuum method; b) either continuum with fracture elements or discrete method; c) discrete method; and d) continuum method with equivalent properties (Jing, 2003).

1.2.1 Continuum methods

The most commonly applied continuum based numerical methods for rock mechanics are the finite difference method (FDM), the finite element method (FEM), and the boundary element method (BEM).

The FDM is a direct approximation of the governing partial differential equations (PDEs) by replacing partial derivatives with finite differences at grids imposed over problem domains, i.e. transferring the original PDEs into a system of algebraic equations in terms of unknowns at grid points. The solution of the system equation is obtained after imposing the necessary initial and boundary conditions.

The FEM is perhaps the most widely applied numerical method in engineering today because of its flexibility in handling material heterogeneity, anisotropy, non-linearity and

complex boundary conditions. The FEM requires the division of the problem domain into a collection of sub-domains (elements) of smaller sizes and standard shapes (triangle, quadrilateral, tetrahedral, etc.), with a fixed number of nodes at the vertices and/or on the sides. Trial functions, usually polynomial, are used to approximate the behavior of PDEs at the element level and generate the local algebraic equations representing the behavior of the elements. The local elemental equations are then assembled, into a global system of algebraic equations whose solution then produces the required information in the solution domain, after imposing the properly defined initial and boundary conditions.

The BEM, on the other hand, requires discretization at the boundary of the solution domains only, thus reducing the problem dimensions by one and greatly simplifying the input requirements. The information required in the solution domain is separately calculated from the information on the boundary, which is obtained by solution of a boundary integral equation, instead of direct solution of the PDEs.

Representation of discontinuities in those methods has been motivated since the late 1960's, especially in the FEM. Various joint element or interface element models like "Goodman joint element" (Goodman et al., 1968), six-node fracture element (Zienkiewicz et al., 1970), thin-layer element (Desai et al., 1984), and interface element based on contact mechanics (Katona, 1983) have been developed. Despite of these efforts, the treatment of fractures and their growth remains limited: Block rotations, complete detachment, and large-scale opening cannot be treated accurately with the FEM.

1.2.2 Discrete Element Methods (DEM)

In the DEM, the fractured medium is treated as an assemblage of rigid or deformable blocks/bodies. The theoretical foundation of the method is the formulation and solution of equations of motion of those blocks using implicit (based on FEM discretization) and explicit (using FDM discretization) formulations. The contacts between blocks are identified and continuously updated during the entire deformation/motion process. Large displacements caused by rigid body motion of individual blocks, including block rotation, fracture opening and complete detachments are straightforward in the discrete approach.

The most representative explicit DEM method is the Distinct Element Method, originally developed by Cundall (1971). It is a force method that employs an explicit time marching scheme to solve directly the Newtonian motion equations. At each time step, the kinematic quantities (velocities, displacements and accelerations) are first calculated and the contact forces or stresses, as well as the internal stresses of the elements, are then obtained via constitutive relations for contacts. This method has been developed extensively since its

introduction. The comprehensive DEM program UDEC (Universal Distinct Element Code) has powerful capabilities, which allow the modeling of variable rock deformability, non-linear joint behavior, fracture of intact rock and fluid flow.

The implicit DEM is represented mainly by the Discontinuous Deformation Analysis (DDA), originated by Shi (1988). DDA is a displacement method, where the unknowns of the equilibrium equations are displacements. The formulation is based on minimization of the total potential energy and contacts are treated using the “penalty” method. DDA has two major advantages over the explicit DEM: 1) relatively large time steps; and 2) closed form integrations for the stiffness matrices of the elements.

The DDA was applied vastly to analyze the stability of underground openings embedded in blocky rock mass (Bakun-Mazor et al., 2009; Chikahisa et al., 1997; Hatzor and Benary, 1998; Hatzor et al., 2010; Tsesarsky and Hatzor, 2006; Wu et al., 2004). However, in cases where stress distribution and deformations in the blocks themselves are critical for the solution, DDA is limited, since in DDA deformation is solved for the center of mass of every block with no stress distribution within blocks. For these cases a hybrid approach between the continuum-based and discontinuum numerical methods is required.

1.3 The Numerical Manifold Method

The numerical manifold method proposed by Shi (1996a) is a natural bridge between the continuum and discrete representations by combining the DDA and FEM methods in a united form (Jing, 2003). It consists of three main parts: block kinematics, finite covering systems, and the simplex integration method (Cheng et al., 2005).

The NMM inherits strengths of the DDA method for block kinematics analysis with its excellent contact detection algorithm, its unique open-close iteration procedure that guarantees that at the end of every time step there is no tension and no penetration between discrete blocks, and its fully dynamic formulation. Thus, it can deal with the mechanical response of a block system under general loading and moving boundary conditions when body movement and large deformation occur simultaneously.

The finite cover system is based on three basic concepts (Ma et al., 2010): the mathematical cover, the physical cover and the manifold element. The mathematical cover consists of finite covers which occupy the whole material volume. They can overlap each other and do not need to conform to neither the external boundaries nor the internal discontinuities. Thus, the meshing task in the NMM is very convenient. On each mathematical cover a weight function is defined. The physical covers are the intersection of the mathematical cover and the physical domain with its internal discontinuities and external

boundaries. The physical cover inherits the weight function from its associated mathematical cover. In addition, a local displacement function is defined on each physical cover. The common area of several physical covers forms a manifold element (Shi, 1996). The weight and local functions of each physical component in the manifold element are connected together to form a global displacement function for each element. Then, the equilibrium equations can be derived from minimizing the total potential energy.

In the NMM, numerical integration such as Gauss integration method is not needed. The NMM uses the simplex integration method (Shi, 1996b), in which an arbitrary domain of integration of a function is converted into many triangles in which the integration can be calculated analytically to ensure high precision (Cheng et al., 2005).

Most of the previous NMM researches were focused on theoretical implementations and improvements of the NMM rather than application to real case studies. Moreover, there is not even a single literature source of applying the NMM for real tunneling case. The main developments of the NMM can be categorized into three groups: 1) Improvement of the approximation accuracy (Chen et al., 1998; Cheng et al., 2002); 2) Extension of the NMM for crack propagation problems (Chiou et al., 2002; Ma et al., 2010; Tsay et al., 1999; Zhang et al., 2010); and 3) Development of 3D NMM (Cheng and Zhang, 2008; He and Ma, 2010; Jiang et al., 2009).

An important limitation of the original NMM when applied to underground mining is that in the original NMM computer program developed by Shi (1996a), tunnels are open from the beginning of the simulation. However, in reality when tunnels are excavated, compressive stresses already exist in the field, and the rock column has already experienced elastic deformation over geologic times due to overburden stress. This issue can be very important when the stability of underground opening in discontinuous rock masses is analyzed.

Miki et al., (2007) introduced a model for tunnel excavation during a NMM simulation suitable for cases where the rock mass contains only few discontinuities, and the immediate medium around the tunnel is continuous so that it can be modeled with a single NMM block.

1.4 Research Objectives

The main goal of this research is to improve the NMM suitability for analyzing the stability of underground openings in blocky rock masses by developing and programming an algorithm which will allow tunnel excavation during the NMM simulation, after the local stresses already exist and the elastic deformation has already occurred. It would be interesting to compare between the modified NMM and the original NMM assessments of the stability of underground openings embedded in blocky rock mass.

A secondary goal of this research is verification of the NMM with 3 static problems (layered plate subjected to gravity, Kirsch solution, and beam under concentrated load and volumetric force) and one dynamic problem (dynamic sliding of a block on an inclined plane).

1.5 Thesis organization

Chapter 2 reviews the theoretical background of the Numerical Manifold Method (NMM) including the finite covering systems, block kinematics, and the simplex integration method. Then, the NMM is verified with four analytical solutions: layered plate subjected to gravity, Kirsch solution, beam under concentrated load and volumetric force, and dynamic sliding of a block on an inclined plane in chapter 3.

Chapter 4 introduces a new algorithm for simulating the excavation sequence with NMM. In addition, the stability of rectangular cavern embedded in an artificial blocky rock mass is analyzed with the modified NMM (with the new algorithm) and the original NMM for various values of friction angles in order to explore the significance of the developed algorithm. In chapter 5, the stability of Zedekiah cave, a 2000 year old underground quarry below the old city of Jerusalem which embedded in blocky rock mass, is analyzed with both modified NMM and original NMM.

Finally, Chapter 6 summarizes the conclusions of this research and makes suggestions regarding future research.

Chapter 2- Scientific Background: Review of NMM principals

This chapter describes the main concepts of the NMM. The description follows the original paper of Shi (1996a), yet with additional figures, descriptions and examples. At the beginning, the NMM finite cover system is described, including construction of mathematical covers with their associated weight functions, generation of physical covers with their local functions and generation of manifold element with their displacement functions. Then, the global equations of equilibrium are derived by minimization of the potential energy, and all potential energy sources (continuous and discontinuous) and their contribution to the global equations of equilibrium are described. Finally, the method of open-close iteration is described.

2.1 NMM finite cover system

As presented at the introduction, the NMM finite cover system is based on three basic concepts: the mathematical cover, the physical cover and the manifold element. In the following three subsections, the construction of mathematical covers, physical covers, manifold elements and their associated functions are presented.

2.1.1 Mathematical cover and weighting functions:

Theoretically any shape of covers can be used in NMM. However integration of manifold elements is related to the cover shape, and a reasonable choice of cover shape is very important (Chen et al., 1998). A triangular finite element mesh is usually adopted to define the mathematical cover for manifold method. Therefore, the construction of mathematical cover that based on triangular elements is presented here.

A mathematical cover is a hexagonal composed of six triangular elements. The common node of the six triangular elements is regarded as a star (Figure 2.1a). On each mathematical cover, a weight function (shape function in the case of FEM cover) w is defined. The weight function is equal to 1 in the center and declines linearly to zero at the sides of the mathematical cover (Figure 2.1b), and has to satisfy

$$\begin{aligned} w_i(x, y) &\geq 0 & (x, y) \in C_i \\ w_i(x, y) &= 0 & (x, y) \notin C_i \end{aligned} \quad (2.1)$$

$$\sum_{i=1}^3 w_i(x, y) = 1 \quad (x, y) \in ME \quad (2.2)$$

where C_i is the mathematical cover and ME is a triangular element.

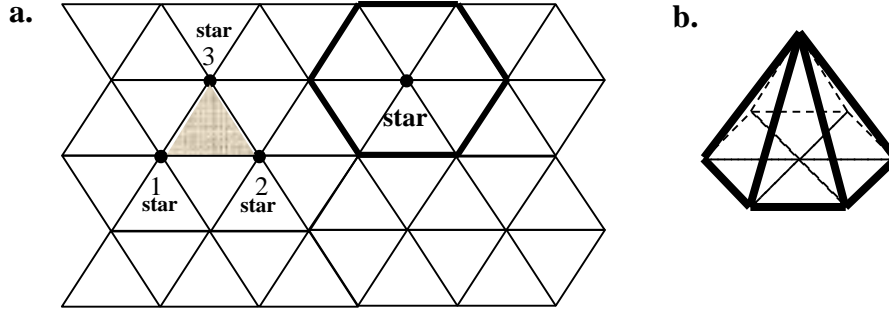


Figure 2.1. The mathematical cover based on triangular finite elements mesh (a) and the weight function of a hexagonal mathematical cover (b) (after Chen et al. (1998)).

Each triangular element (ME) is the common region of three mathematical covers ($M_{(i)}$, $i = 1,2,3$) which are located in the triangular vertexes. On each triangular element the three weight functions of the mathematical covers are:

$$w_{e(i)} = S_{(i)} / S, \quad i = 1,2,3 \quad (2.3)$$

Where $S_{(i)}$, $i = 1,2,3$ are the areas of the sub triangles created by a node (x,y) inside the triangle and two of its vertexes (Figure 2.2), and S is the area of the triangle. The following expressions denote those areas

$$S = \frac{1}{2} \begin{vmatrix} 1 & x_{(1)} & y_{(1)} \\ 1 & x_{(2)} & y_{(2)} \\ 1 & x_{(3)} & y_{(3)} \end{vmatrix} \quad (2.4)$$

$$S_{(1)} = \frac{1}{2} \begin{vmatrix} 1 & x & y \\ 1 & x_{(2)} & y_{(2)} \\ 1 & x_{(3)} & y_{(3)} \end{vmatrix} = \frac{1}{2} [(x_{(2)}y_{(3)} - x_{(3)}y_{(2)}) + (y_{(2)} - y_{(3)})x + (x_{(3)} - x_{(2)})y] \quad (2.5)$$

$$S_{(2)} = \frac{1}{2} \begin{vmatrix} 1 & x_{(1)} & y_{(1)} \\ 1 & x & y \\ 1 & x_{(3)} & y_{(3)} \end{vmatrix} = \frac{1}{2} [(x_{(3)}y_{(1)} - x_{(1)}y_{(3)}) + (y_{(3)} - y_{(1)})x + (x_{(1)} - x_{(3)})y] \quad (2.6)$$

$$S_{(3)} = \frac{1}{2} \begin{vmatrix} 1 & x_{(1)} & y_{(1)} \\ 1 & x_{(2)} & y_{(2)} \\ 1 & x & y \end{vmatrix} = \frac{1}{2} [(x_{(1)}y_{(2)} - x_{(2)}y_{(1)}) + (y_{(1)} - y_{(2)})x + (x_{(2)} - x_{(1)})y] \quad (2.7)$$

Denote:

$$\begin{pmatrix} f_{11} & f_{12} & f_{13} \\ f_{21} & f_{22} & f_{23} \\ f_{31} & f_{32} & f_{33} \end{pmatrix} = \frac{1}{2S} \begin{bmatrix} x(2)y(3) - x(3)y(2) & y(2) - y(3) & x(3) - x(2) \\ x(3)y(1) - x(1)y(3) & y(3) - y(1) & x(1) - x(3) \\ x(1)y(2) - x(2)y(1) & y(1) - y(2) & x(2) - x(1) \end{bmatrix} \quad (2.8)$$

then,

$$w_{e(i)} = \begin{cases} w_{e(1)}(x, y) \\ w_{e(2)}(x, y) \\ w_{e(3)}(x, y) \end{cases} = \begin{pmatrix} f_{11} & f_{12} & f_{13} \\ f_{21} & f_{22} & f_{23} \\ f_{31} & f_{32} & f_{33} \end{pmatrix} \begin{Bmatrix} 1 \\ x \\ y \end{Bmatrix} = \begin{pmatrix} f_{11} + f_{12}x + f_{13}y \\ f_{21} + f_{22}x + f_{23}y \\ f_{31} + f_{32}x + f_{33}y \end{pmatrix} \quad (2.9)$$

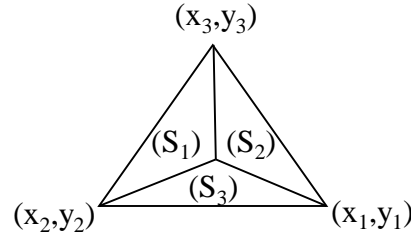


Figure 2.2. Triangular element divided to three sub triangles (after An (2010)).

2.1.2 Physical cover and local function

The physical cover is the intersection of the mathematical cover and the material volume, and it inherits the weight function from its associate mathematical cover. In addition, on each physical cover, a local cover function is defined. The cover function can be constant, linear, high order polynomials or locally series. In the original NMM, however, a constant cover function is defined as:

$$\begin{aligned} u &= u_i \\ v &= v_i \end{aligned} \quad (2.10)$$

If a mathematical cover is partially out of the physical cover, the weight function should be effective only in the region of the physical cover, and thus, a modifier, δ_i , is acting on the weight function

$$w_i(x, y) = \delta_i \cdot w_i(x, y) \quad (2.11)$$

where $\delta_i = 1$, within the problem domain, and $\delta_i = 0$ elsewhere.

In order to explain how the physical covers and manifold elements are generated, an example of a square body with vertical discontinuity is presented in Figure 2.3a, and the mathematical cover which overlaps the body is presented in Figure 2.3b. Taking node 1 as a star, two triangular elements (1,3) are included in this star, the mathematical cover M_1 is cut by the external boundary and by the vertical discontinuity into three parts. Thus two physical

cover P_1^1 and P_1^2 which are inside the problem domain are generated. The generation of all the physical covers in the problem is presented in Table 2.1.

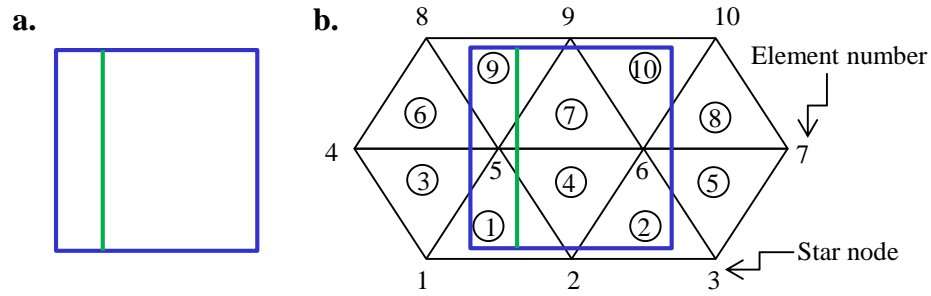
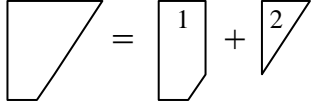
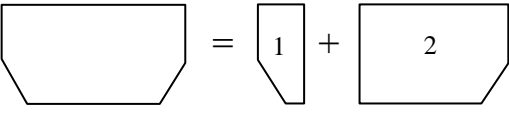
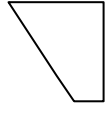


Figure 2.3. An example of manifold problem: Rectangular body with vertical discontinuity (a); and NMM model of the problem with triangular finite elements mesh (b).

Table 2.1 The physical covers in the NMM model.

Mathematical cover	Physical cover	
1	P_1^1, P_1^2	
2	P_2^1, P_2^2	
3	P_3^1	
4	P_4^1	
5	P_5^1, P_5^2	
6	P_6^1	
7	P_7^1	

8	$\mathbf{P}_8^1, \mathbf{P}_8^2$	
9	$\mathbf{P}_9^1, \mathbf{P}_9^1$	
10	\mathbf{P}_{10}^1	

2.1.3 Manifold elements and global displacement function

The elements of the manifold are the common regions of the physical covers, and thus, are also the common region of three stars. In the previous example, the common area of three physical covers P_1^1, P_2^1, P_5^2 forms one manifold element ME_1 , which is the intersection of stars 1, 2 and 5.

The linear weight function given in Eq. (2.9) and the constant local function given in Eq. (2.10) of each physical component in the manifold element are connected together to form a global linear displacement function for each manifold element which is given by:

$$\begin{Bmatrix} u(x, y) \\ v(x, y) \end{Bmatrix} = \begin{pmatrix} w_{e(1)}(x, y) & 0 & w_{e(2)}(x, y) & 0 & w_{e(3)}(x, y) & 0 \\ 0 & w_{e(1)}(x, y) & 0 & w_{e(2)}(x, y) & 0 & w_{e(3)}(x, y) \end{pmatrix} \begin{Bmatrix} u_{e(1)} \\ v_{e(1)} \\ u_{e(2)} \\ v_{e(2)} \\ u_{e(3)} \\ v_{e(3)} \end{Bmatrix} \quad (2.12)$$

where $e(1), e(2), e(3)$ are the three star nodes of the manifold element.

Denote:

$$[T_{e(i)}(x, y)] = \begin{pmatrix} w_{e(i)}(x, y) & 0 \\ 0 & w_{e(i)}(x, y) \end{pmatrix} \quad (2.13)$$

$$\{D_{e(i)}\} = \begin{pmatrix} u_{e(i)} \\ v_{e(i)} \end{pmatrix}, \quad i = 1, 2, 3 \quad (2.14)$$

the displacement becomes

$$\begin{Bmatrix} u(x, y) \\ v(x, y) \end{Bmatrix} = [T_e] \{D_e\} \quad (2.15)$$

It is important to note that when a mathematical cover is divided into two completely disconnected domains by a discontinuity boundary, the two manifold elements which are created should be able to move apart. Thus, two mathematical covers with the same shape and position are needed. In the previous example, there are four couples of manifold elements which are common region of star nodes, but are divided by the discontinuity: ME_1 and ME_2 (star 1, 2, and 5), ME_5 and ME_6 (star 2, 5, and 6), ME_9 and ME_{20} (star 5, 6, and 9), and ME_{12} and ME_{13} (star 5, 8, and 9). Therefore, each star splits into two stars with different effective region, and new stars numbering is performed (Figure 2.4).

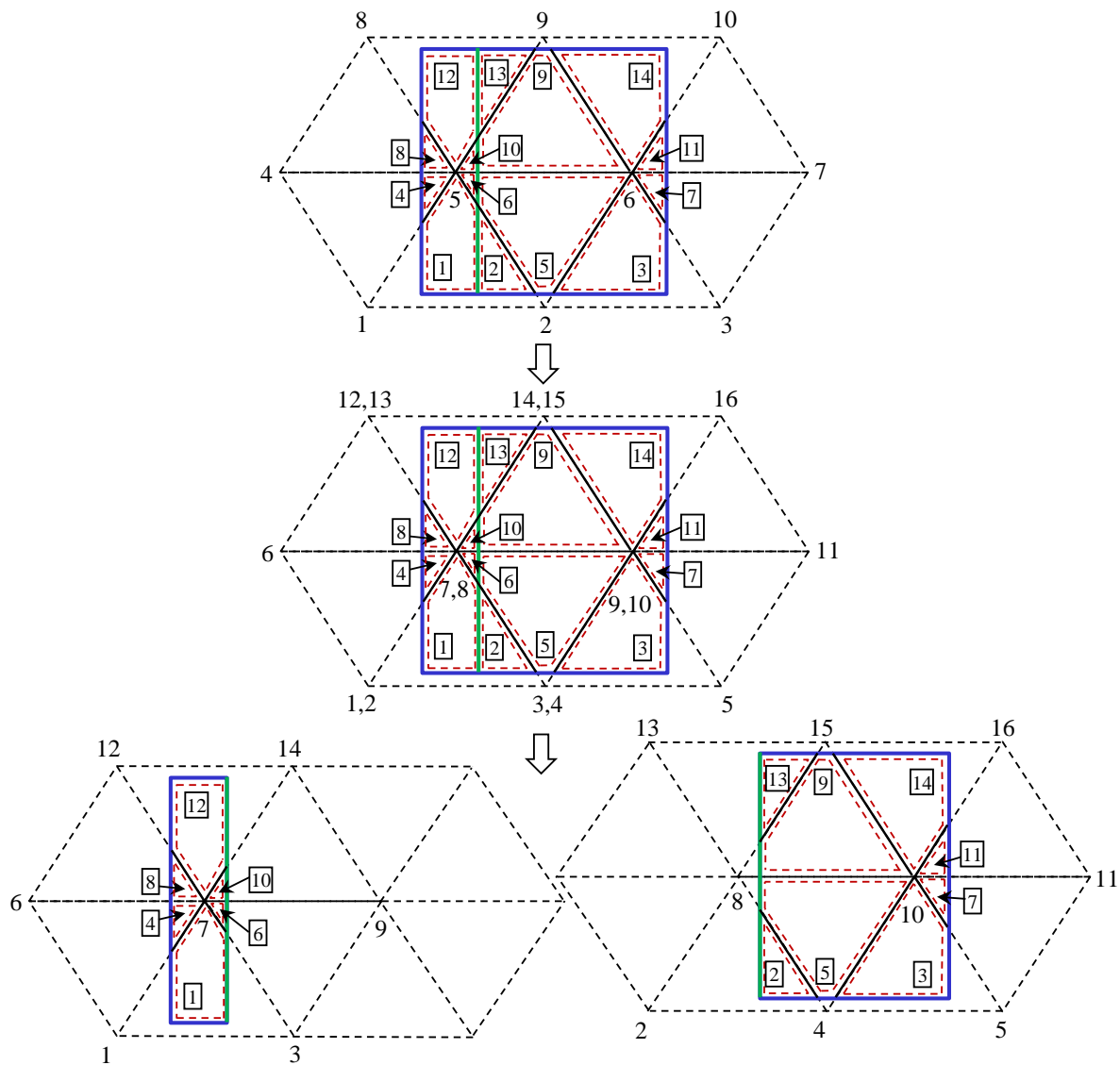


Figure 2.4. Generation of two mathematical covers from a single mathematical cover which holds a discontinuity.

2.2 Global equations of equilibrium

The global equations of equilibrium are derived using a FEM style potential energy minimization. The total potential energy Π is the summation of all the potential energy sources: 1) strain energy; 2) initial stresses; 3) point load; 4) body load; 5) inertia force; and 6) fixed points for the continuous material, and 7) contact springs; and 8) friction forces for the discontinuities. The total potential energy can be expressed as follow for a problem with n star nodes:

$$\Pi = \frac{1}{2} \begin{Bmatrix} D_1^T & D_2^T & \dots & D_n^T \end{Bmatrix} \begin{Bmatrix} K_{11} & K_{12} & \dots & K_{1n} \\ K_{21} & K_{22} & \dots & K_{2n} \\ \vdots & \vdots & \ddots & \vdots \\ K_{n1} & K_{n2} & \dots & K_{nn} \end{Bmatrix} \begin{Bmatrix} D_1 \\ D_2 \\ \vdots \\ D_n \end{Bmatrix} + \begin{Bmatrix} D_1^T & D_2^T & \dots & D_n^T \end{Bmatrix} \begin{Bmatrix} F_1 \\ F_2 \\ \vdots \\ F_n \end{Bmatrix} + C \quad (2.16)$$

where $\{D_i\}$ is a 2×1 sub-vector of the displacements $(u_i \ v_i)$ of a star node, $[K_{ij}]$ is the coefficient 2×2 sub-matrix, and $\{F_i\}$ is 2×1 loading sub-vector. Minimizing the total potential energy Π , the global equations of equilibrium are:

$$\begin{Bmatrix} K_{11} & K_{12} & \dots & K_{1n} \\ K_{21} & K_{22} & \dots & K_{2n} \\ \vdots & \vdots & \ddots & \vdots \\ K_{n1} & K_{n2} & \dots & K_{nn} \end{Bmatrix} \begin{Bmatrix} D_1 \\ D_2 \\ \vdots \\ D_n \end{Bmatrix} = \begin{Bmatrix} F_1 \\ F_2 \\ \vdots \\ F_n \end{Bmatrix} \quad (2.17)$$

In the following two sections, the potential energy sources (continuous and discontinuous), and their contribution to the global equations of equilibrium are described.

2.3 Continuous material contribution to the global equations of equilibrium

2.3.1 Stiffness matrix:

The strain energy Π_e done by the elastic stresses of element e is:

$$\Pi_e = \iint_A \frac{1}{2} \begin{pmatrix} \varepsilon_x & \varepsilon_y & \gamma_{xy} \end{pmatrix} \begin{Bmatrix} \sigma_x \\ \sigma_y \\ \tau_{xy} \end{Bmatrix} dx dy \quad (2.18)$$

where the integration is over the entire material area A of that element.

The relationship between stress and strain for plane stress condition is given by Hooke's law:

$$\begin{Bmatrix} \sigma_x \\ \sigma_y \\ \tau_{xy} \end{Bmatrix} = \frac{E}{1-\nu^2} \begin{pmatrix} 1 & \nu & 0 \\ \nu & 1 & 0 \\ 0 & 0 & \frac{1-\nu}{2} \end{pmatrix} \begin{Bmatrix} \varepsilon_x \\ \varepsilon_y \\ \tau_{xy} \end{Bmatrix} = [E] \begin{Bmatrix} \varepsilon_x \\ \varepsilon_y \\ \tau_{xy} \end{Bmatrix} \quad (2.19)$$

where E and ν are the Young's modulus and Poisson's ratio respectively. For a plane strain condition, E and ν can be replaced by

$$E_{P,\varepsilon} = E/(1-\nu^2) \quad (2.20)$$

$$\nu_{P,\varepsilon} = \nu/(1-\nu) \quad (2.21)$$

The relationship between strain and displacement is:

$$\begin{Bmatrix} \varepsilon_x \\ \varepsilon_y \\ \varepsilon_z \end{Bmatrix} = \begin{pmatrix} \frac{\partial u}{\partial x} \\ \frac{\partial v}{\partial y} \\ \frac{\partial u}{\partial y} + \frac{\partial v}{\partial x} \end{pmatrix} \quad (2.22)$$

substituting Eq. (2.12), the strain becomes:

$$\begin{Bmatrix} \varepsilon_x \\ \varepsilon_y \\ \varepsilon_z \end{Bmatrix} = \begin{pmatrix} \frac{\partial w_{e(1)}(x,y)}{\partial x} & 0 & \frac{\partial w_{e(2)}(x,y)}{\partial x} & 0 & \frac{\partial w_{e(3)}(x,y)}{\partial x} & 0 \\ 0 & \frac{\partial w_{e(1)}(x,y)}{\partial y} & 0 & \frac{\partial w_{e(2)}(x,y)}{\partial y} & 0 & \frac{\partial w_{e(3)}(x,y)}{\partial y} \\ \frac{\partial w_{e(1)}(x,y)}{\partial y} & \frac{\partial w_{e(1)}(x,y)}{\partial x} & \frac{\partial w_{e(2)}(x,y)}{\partial y} & \frac{\partial w_{e(2)}(x,y)}{\partial x} & \frac{\partial w_{e(3)}(x,y)}{\partial y} & \frac{\partial w_{e(3)}(x,y)}{\partial x} \end{pmatrix} \begin{Bmatrix} u_{e(1)} \\ v_{e(1)} \\ u_{e(2)} \\ v_{e(2)} \\ u_{e(3)} \\ v_{e(3)} \end{Bmatrix} \quad (2.23)$$

Denote:

$$[B_{e(i)}] = \begin{pmatrix} \frac{\partial w_{e(i)}(x,y)}{\partial x} & 0 \\ 0 & \frac{\partial w_{e(i)}(x,y)}{\partial y} \\ \frac{\partial w_{e(i)}(x,y)}{\partial y} & \frac{\partial w_{e(i)}(x,y)}{\partial x} \end{pmatrix}, \quad i = 1,2,3 \quad (2.24)$$

and substitute Eq. (2.14), the strain becomes:

$$\begin{Bmatrix} \varepsilon_x \\ \varepsilon_y \\ \tau_{xy} \end{Bmatrix} = [B_e] \{D_e\} \quad (2.25)$$

and the strain energy is rewritten in a matrix form as:

$$\begin{aligned}\Pi_e &= \frac{1}{2} \iint_A \{D_e\}^T [B_e]^T [E][B_e] \{D_e\} dx dy = \frac{1}{2} \{D_e\}^T \left[\iint_A [B_e]^T [E][B_e] dx dy \right] \{D_e\} \\ &= \frac{1}{2} \{D_e\}^T \left(S^e [B_e]^T [E][B_e] \right) \{D_e\}\end{aligned}\quad (2.26)$$

where S^e is the area of the element. Therefore,

$$S^e [B_{e(r)}]^T [E][B_{e(s)}] \rightarrow [K_{e(r)e(s)}] \quad r, s = 1, 2, 3 \quad (2.27)$$

is the element [6x6] stiffness matrix that composed of 9 [2x2] matrices which are assembled into the global stiffness matrix $[K_e]$ according to the element's nodes.

where $e(1)$, $e(2)$, $e(3)$ are the three star nodes of the manifold element.

2.3.2 Initial stress matrix:

The manifold method is a step by step method. The computed stresses of previous time step will be the initial stresses of the next time step. Therefore the initial stresses are essential for manifold computation.

The potential energy of the initial constant stresses for the element e is:

$$\Pi_\sigma = \iint_A \begin{pmatrix} \varepsilon_x & \varepsilon_y & \gamma_{xy} \end{pmatrix} \begin{Bmatrix} \sigma_x^0 \\ \sigma_y^0 \\ \tau_{xy}^0 \end{Bmatrix} dx dy \quad (2.28)$$

where $\begin{Bmatrix} \sigma_x^0 & \sigma_y^0 & \tau_{xy}^0 \end{Bmatrix}^T$ are the initial stresses in the element.

Denote

$$\{\sigma_e^0\} = \begin{Bmatrix} \sigma_x^0 \\ \sigma_y^0 \\ \tau_{xy}^0 \end{Bmatrix} \quad (2.29)$$

and substitute Eq. (2.25), the potential energy is rewritten in a matrix form as:

$$\Pi_\sigma = \iint_A \{D_e\}^T [B_e]^T \{\sigma_e^0\} dx dy = S^e \{D_e\}^T [B_e]^T \{\sigma_e^0\} \quad (2.30)$$

Therefore,

$$S^e [B_{e(r)}]^T \{\sigma_e^0\} \rightarrow \{F_{e(r)}\}, \quad r = 1, 2, 3 \quad (2.31)$$

is the element $\{6 \times 1\}$ load vector composed of 3 $\{2 \times 1\}$ vectors which are assembled into the global loading vector $\{F_e\}$ according to the element's nodes.

2.3.3 Point load matrix

The potential energy due to point loading is:

$$\Pi_p = -(u(x_0, y_0) \quad v(x_0, y_0)) \begin{Bmatrix} F_x \\ F_y \end{Bmatrix} = -\{D_e\}^T [T_e(x_0, y_0)]^T \begin{Bmatrix} F_x \\ F_y \end{Bmatrix} \quad (2.32)$$

where $\begin{Bmatrix} F_x & F_y \end{Bmatrix}^T$ is the loading force which acts on points (x_0, y_0) of element e .

Therefore,

$$[T_{e(r)}(x_0, y_0)]^T \begin{Bmatrix} F_x \\ F_y \end{Bmatrix} \rightarrow \{F_{e(r)}\}, \quad r = 1, 2, 3 \quad (2.33)$$

is the element $\{6 \times 1\}$ point load vector composed of 3 $\{2 \times 1\}$ vectors which are assembled into the global loading vector $\{F_e\}$ according to the element's nodes.

2.3.4 Body force matrix

The potential energy due to body force loading is:

$$\Pi_w = -\iint_A (u(x, y) \quad v(x, y)) \begin{Bmatrix} f_x \\ f_y \end{Bmatrix} dx dy = -\{D_e\}^T \left[\iint_A [T_e(x, y)] dx dy \right] \begin{Bmatrix} f_x \\ f_y \end{Bmatrix} \quad (2.34)$$

where $\begin{Bmatrix} f_x & f_y \end{Bmatrix}^T$ is a constant body force acting on the area of element e .

Substituting Eq. (2.13) and (2.9), the potential energy becomes:

$$\begin{aligned} \Pi_w &= -\{D_e\}^T \left[\iint_A \begin{bmatrix} w_{e(i)}(x, y) & 0 \\ 0 & w_{e(i)}(x, y) \end{bmatrix} dx dy \right] \begin{Bmatrix} f_x \\ f_y \end{Bmatrix} \\ &= -\{D_e\}^T \left[\iint_A \begin{bmatrix} f_{r1} + f_{r2}x + f_{r3}y & 0 \\ 0 & f_{r1} + f_{r2}x + f_{r3}y \end{bmatrix} dx dy \right] \begin{Bmatrix} f_x \\ f_y \end{Bmatrix} \\ &= -\{D_e\}^T \begin{pmatrix} f_{r1}S^e + f_{r2}S_x^e + f_{r3}S_y^e & 0 \\ 0 & f_{r1}S^e + f_{r2}S_x^e + f_{r3}S_y^e \end{pmatrix} \begin{Bmatrix} f_x \\ f_y \end{Bmatrix}, \quad r = 1, 2, 3 \end{aligned} \quad (2.35)$$

where

$$S_x^e = \iint_A x dx dy \quad (2.36)$$

$$S_y^e = \iint_A y dx dy \quad (2.37)$$

Therefore,

$$\begin{pmatrix} f_{r1}S^e + f_{r2}S_x^e + f_{r3}S_y^e & 0 \\ 0 & f_{r1}S^e + f_{r2}S_x^e + f_{r3}S_y^e \end{pmatrix} \begin{Bmatrix} f_x \\ f_y \end{Bmatrix} \rightarrow \{F_{e(r)}\}, \quad r = 1, 2, 3 \quad (2.38)$$

is the element $\{6 \times 1\}$ body loading vector composed of 3 $\{2 \times 1\}$ vectors which are assembled into the global loading vector $\{F_e\}$ according to the element's nodes.

2.3.5 Inertia force matrix

The potential energy of the inertia force of element e is:

$$\Pi_i = - \iint_A (u \quad v) \begin{Bmatrix} f_x \\ f_y \end{Bmatrix} dx dy \quad (2.39)$$

where the inertia force is:

$$\begin{Bmatrix} f_x \\ f_y \end{Bmatrix} = -M \frac{\partial^2}{\partial t^2} \begin{Bmatrix} u(t) \\ v(t) \end{Bmatrix} = -M [T_e] \frac{\partial^2 \{D_e(t)\}}{\partial t^2} \quad (2.40)$$

and $\{u(t) \quad v(t)\}^T$ is the time dependent displacement of any point (x, y) of element e in the current time step, and M is the mass per unit area.

Substituting Eq. (2.40) into Eq. (2.39), the potential energy is rewritten in a matrix form as:

$$\Pi_i = - \iint_A M \{D_e\}^T [T_e]^T [T_e] \frac{\partial^2 \{D_e(t)\}}{\partial t^2} dx dy \quad (2.41)$$

The displacement at the end of the time step can be expressed as a Taylor series as:

$$\begin{aligned} \{D_e\} &= \{D_e(\Delta(t))\} = \{D_e(0)\} + \Delta(t) \frac{\partial \{D_e(0)\}}{\partial t} + \Delta(t)^2 \frac{\partial^2 \{D_e(0)\}}{2\partial t^2} \\ &= \Delta(t) \frac{\partial \{D_e(0)\}}{\partial t} + \Delta(t)^2 \frac{\partial^2 \{D_e(0)\}}{2\partial t^2} \end{aligned} \quad (2.42)$$

where $\{D_e(0)\} = \{0\}$ is the element displacement at the beginning of the time step, $\{D_e(\Delta(t))\} = \{D_e\}$ is the displacement at the end of the time step, and $\Delta(t)$ is the time interval of this time step.

Manipulation on Eq. (2.42) gives:

$$\frac{\partial^2 \{D_e(0)\}}{\partial t^2} = \frac{2}{\Delta(t)^2} \{D_e\} - \frac{2}{\Delta(t)} \frac{\partial \{D_e(0)\}}{\partial t} = \frac{2}{\Delta(t)^2} \{D_e\} - \frac{2}{\Delta(t)} \{V_e(0)\} \quad (2.43)$$

where

$$\{V_e(0)\} = \frac{\partial \{D_e(0)\}}{\partial t}$$

is the velocity at the beginning of the time step.

The potential energy is therefore,

$$\Pi_i = M \{D_e\}^T \left[\iint_A [T_e]^T [T_e] dx dy \right] \left(\frac{2}{\Delta(t)^2} \{D_e\} - \frac{2}{\Delta(t)} \{V_e(0)\} \right) \quad (2.44)$$

Substituting Eq. (2.9), the integration part can be computed as:

$$\begin{aligned} \iint_A [T_e]^T [T_e] dx dy &= \iint_A \begin{pmatrix} w_{e(r)(s)} & 0 \\ 0 & w_{e(r)(s)} \end{pmatrix} dx dy \\ &= \iint_A \begin{pmatrix} (f_{r1} + f_{r2}x + f_{r3}y)(f_{s1} + f_{s2}x + f_{s3}y) & 0 \\ 0 & (f_{r1} + f_{r2}x + f_{r3}y)(f_{s1} + f_{s2}x + f_{s3}y) \end{pmatrix} dx dy \end{aligned} \quad (2.45)$$

Denote:

$$\begin{aligned} t_{e(r)e(s)} &= \iint_A (f_{r1} + f_{r2}x + f_{r3}y)(f_{s1} + f_{s2}x + f_{s3}y) dx dy \\ &= f_{r1}f_{s1}S^e + (f_{r1}f_{s2} + f_{r2}f_{s1})S_x^e + (f_{r1}f_{s3} + f_{r3}f_{s1})S_y^e + f_{r2}f_{s2}S_{xx}^e \\ &\quad + f_{r3}f_{s3}S_{yy}^e + (f_{r2}f_{s3} + f_{r3}f_{s2})S_{xy}^e \end{aligned} \quad (2.46)$$

where

$$S_{xx}^e = \iint_A x^2 dx dy \quad (2.47)$$

$$S_{yy}^e = \iint_A y^2 dx dy \quad (2.48)$$

$$S_{xy}^e = \iint_A xy dx dy \quad (2.49)$$

and substitute Eq. (2.46) into Eq. (2.44), the potential energy becomes:

$$\Pi_i = M \{D_e\}^T \begin{pmatrix} t_{e(r)e(s)} & 0 \\ 0 & t_{e(r)e(s)} \end{pmatrix} \left(\frac{2}{\Delta(t)^2} \{D_e\} - \frac{2}{\Delta(t)} \{V_e(0)\} \right) \quad (2.50)$$

Therefore,

$$\frac{2}{\Delta(t)^2} M \begin{pmatrix} t_{e(r)e(s)} & 0 \\ 0 & t_{e(r)e(s)} \end{pmatrix} \rightarrow [K_{e(r)e(s)}] \quad r, s = 1, 2, 3 \quad (2.51)$$

is the element [6x6] stiffness matrix composed of 9 [2x2] matrices which are assembled into the global stiffness matrix $[K_e]$ according to the element's nodes, and

$$\frac{2}{\Delta(t)} M \begin{pmatrix} t_{e(r)e(s)} & 0 \\ 0 & t_{e(r)e(s)} \end{pmatrix} \{V_{e(s)}(0)\} \rightarrow \{F_{e(r)}\}, \quad r, s = 1, 2, 3 \quad (2.52)$$

is the element {6x1} inertia force vector composed of 3 {2x1} vectors which are assembled into the global loading vector $\{F_e\}$ according to the element's nodes.

2.3.6 Fixed point matrix

As a boundary condition, some of the elements are fixed at specific points. The constraint can be applied by using two very stiff springs. The strain energy of the spring is:

$$\Pi_f = \frac{k}{2} \begin{pmatrix} u(x_0, y_0) & v(x_0, y_0) \end{pmatrix} \begin{Bmatrix} u(x_0, y_0) \\ v(x_0, y_0) \end{Bmatrix} = \frac{k}{2} \{D_e\}^T [T_e(x_0, y_0)]^T [T_e(x_0, y_0)] \{D_e\} \quad (2.53)$$

where (x_0, y_0) are the fixed point coordinates, and k is the stiffness of the two springs which are along the x and y directions respectively ($k_x = k_y$).

Therefore,

$$p[T_e(x_0, y_0)]^T [T_e(x_0, y_0)] = p w_{e(r)}(x_0, y_0) w_{e(s)}(x_0, y_0) \begin{pmatrix} 1 & 0 \\ 0 & 1 \end{pmatrix} \rightarrow [K_{e(r)e(s)}] \quad r, s = 1, 2, 3 \quad (2.54)$$

is the element [6x6] stiffness matrix that composed of 9 [2x2] matrices which are assembled into the global stiffness matrix $[K_e]$ according to the element's nodes.

2.4 Adding discontinuities to the global equations of equilibrium

The main advantage of the NMM approach is its capability of modeling the behavior of discontinues materials. Thus, it is necessary to connect the individual discontinuous boundaries into the global equations system. The approach is based on the condition of no tension and no penetration between the two contact sides of a discontinuity, mathematically described by two inequalities. Coloumb's friction law is another inequality which has to be satisfied. The NMM is an incremental approach. The time steps should be chosen small enough so that the displacements of all points in the problem domain are less than a pre-

defined limit ρ . Due to the small time steps, the displacements are small too, and the three inequalities can be simplified to linear inequalities of $\{D_i\}$.

2.4.1 Contacts detection and definition

At the beginning of each time step, a two-stage contact detecting process is performed: the first stage is a global search for blocks that might be in contact during the time step. Two blocks can be in contact during the time step only if the minimum distance between any pair of points, $P_1(x_1, y_1)$ of block i and $P_2(x_2, y_2)$ of block j , is less than a numerical control parameter 2ρ . The second stage is a local search for three types of contacts: 1) angle to angle; 2) angle to edge; and 3) edge to edge (Figure 2.5). The edge to edge contacts are transferred into angle to edge contacts. On the contrary to DDA, the angles in the NMM are also the intersection points of the triangular mesh elements with block boundaries or joints, and not only the vertices of physical boundaries. For example, in the problem described in section 2.1.2, there are two angle to edge contacts at the ends of the vertical discontinuity which are the vertices of the blocks, and three more angle to edge contacts along the vertical discontinuity which are the intersection of the triangular mesh with block boundaries (Figure 2.6).

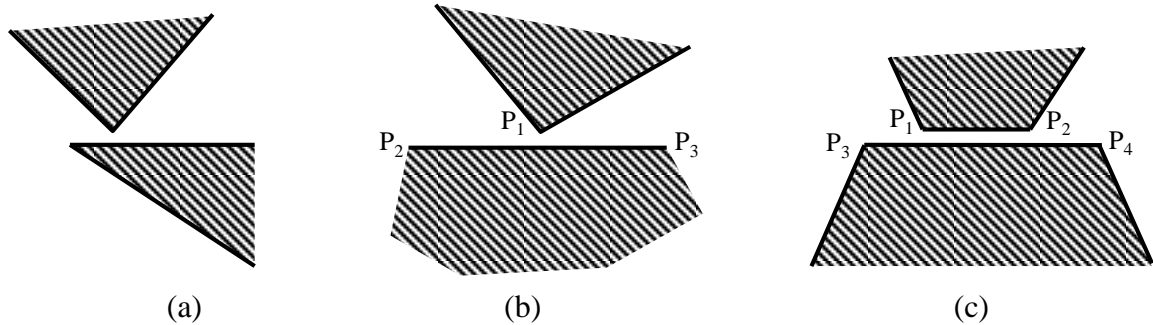


Figure 2.5. Types of block contacts: a) angle to angle; b) angle to edge; c) edge to edge; (Modified after Shi (1996a)).

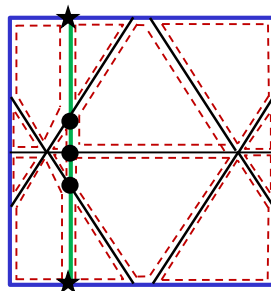


Figure 2.6. Contacts in the example problem. The stars represent contacts of physical boundary vertices, and the dots represent contacts of the intersection points of the triangular mesh with physical boundaries.

The angle to angle contact is defined to be a contact if the minimum distance of two angle vertices of the contacts is less than 2ρ , and the maximum overlapping angle of the two angles is less than 2δ when one angle vertex translates to the vertex of other angle without rotation. In the computer program, $\delta = 1.5^\circ$. An illustration of the overlapping angle of the two angles is shown in Figure 2.7a.

The angle to edge contact is defined to be a contact if the minimum distance of the angle vertex to the edge of the contacts is less than 2ρ , and the maximum overlapping angle of the angle and the edge is less than 2δ when the angle vertex translates to the edge without rotation. An illustration of the overlapping angle of the angle and the edge is shown in Figure 2.7b.

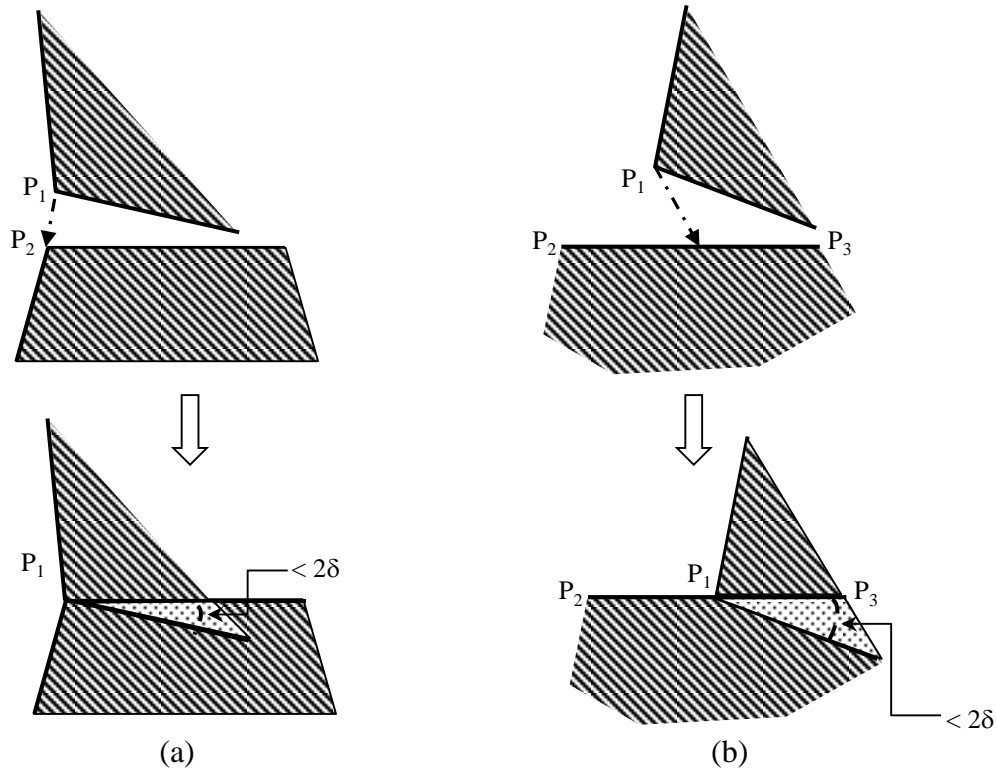


Figure 2.7. Illustration of overlapping angle: a) angle to angle; b) angle to edge; (Modified after Shi (1996a)).

2.4.2 Entrance Lines of Contacts

At the end of each time step, the condition of no tension and no penetration between the two contact sides of a discontinuity must be satisfied. In order to be able to describe mathematically the no penetration condition, an entrance line is defined. Generally, a penetration occurs when a vertex crosses the entrance line. The definition of entrance lines

and the conditions for penetrations in the three different contact configurations are as following:

1. For the case of angle to angle contact, if both angles are less than 180° , there are two entrance lines which are defined according to Table 2.2. The penetration occurs when the two entrance lines are passed simultaneously by the vertex of the other angle.
2. For the case of angle to angle contact, if one of the two associated angles is greater than 180° , there are two entrance lines which are the two edges of the angle which is greater than 180° . The penetration occurs when one of the two entrance line is passed by the vertex of the other angle.
3. For the case of angle to edge contact, the edge is defined as the entrance line. The penetration occurs when the entrance line is passed by the angle vertex.

Table 2.2. Definition of entrance lines in an angle to angle contact when both angles are less than 180° (modified after Shi (1996a)).

	Associated angles		Entrance lines		Figures
angle to angle contact: both angles are less than 180°	$\alpha \leq 180^\circ$	$\beta \leq 180^\circ$	OE ₃	OE ₂	
	$\alpha \leq 180^\circ$	$\beta > 180^\circ$	OE ₃	OE ₄	
	$\alpha > 180^\circ$	$\beta \leq 180^\circ$	OE ₁	OE ₂	
	$\alpha > 180^\circ$	$\beta > 180^\circ$	OE ₁	OE ₄	

Note: OE₁ and OE₂ are two sides of angle 1, and OE₃ and OE₄ are two sides of angle 2.

α is the angle from OE₁ to OE₃, and β is the angle from OE₂ to OE₄.

The bold lines in the figures are the entrance lines.

A vertex P_1 penetrates the entrance line P_2P_3 (points P_1, P_2, P_3 rotate anticlockwise) if the area of the triangle which is formed by the 3 points in the end of the time step is negative (Figure 2.8). Thus, the criterion for penetration is an inequality, defined as:

$$\Delta = \begin{vmatrix} 1 & x_1 + u_1 & y_1 + v_1 \\ 1 & x_2 + u_2 & y_2 + v_2 \\ 1 & x_3 + u_3 & y_3 + v_3 \end{vmatrix} < 0 \quad (2.55)$$

where (x_i, y_i) and (u_i, v_i) are the coordinates and displacements of P_i ($i = 1, 2, 3$), respectively.

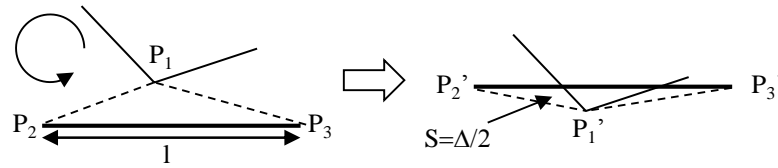


Figure 2.8. Penetration criterion: vertex entrance line relationship in the beginning of the time step (left hand side), and in the end of the time step (right hand side); (Modified after (Shi, 1996a)).

In order to prevent the penetration of the two sides of the contacts, normal stiff springs are applied to push the vertex away from the entrance line as follows:

- 1) For the case of angle to angle contact, if both angles are less than 180, a single stiff spring is inserted between a vertex and its corresponding entrance line, where the passing distance between the vertex and its corresponding entrance line is smallest.
- 2) For the case of angle to angle contact with an angle larger than 180, if only one of the two entrance lines has been passed by the corresponding vertex of another angle, a single stiff spring is inserted along the normal to this edge. If two entrance lines have been passed, two stiff springs are applied to the two entrance edges.
- 3) For angle to edge contact, a single stiff spring is applied where the passing distance between the vertex and the edge is smallest.

There are three possible modes for a contact: one open ($\Delta > 0$) and two close modes ($\Delta \leq 0$): sliding and lock. For an open contact no springs are applied. For a sliding angle to edge contact, a normal stiff spring, and a pair of shear sliding forces are applied. For a lock angle to edge contact, a normal stiff spring is applied and another shear stiff spring is applied in order to avoid the tangential displacement between the vertex and the edge. For a sliding and lock angle to angle contacts, only normal spring is applied.

2.4.2.1 Normal Contact Matrices

The strain energy of the normal spring is:

$$\Pi_n = \frac{k_n d_n^2}{2} \quad (2.56)$$

where k_n is the spring stiffness, and d_n is the entrance distance.

Considering inequality (2.55), the entrance distance d_n between a vertex P_1 of element i to its corresponding entrance line P_2P_3 of element j (element i and element j are located in different sides of the discontinuity) is:

$$d_n = \frac{\Delta}{l} = \frac{1}{l} \begin{vmatrix} 1 & x_1 + u_1 & y_1 + v_1 \\ 1 & x_2 + u_2 & y_2 + v_2 \\ 1 & x_3 + u_3 & y_3 + v_3 \end{vmatrix} = \frac{1}{l} \left(\begin{vmatrix} 1 & x_1 & y_1 \\ 1 & x_2 & y_2 \\ 1 & x_3 & y_3 \end{vmatrix} + \begin{vmatrix} 1 & u_1 & y_1 \\ 1 & u_2 & y_2 \\ 1 & u_3 & y_3 \end{vmatrix} + \begin{vmatrix} 1 & x_1 & v_1 \\ 1 & x_2 & v_2 \\ 1 & x_3 & v_3 \end{vmatrix} + \begin{vmatrix} 1 & u_1 & v_1 \\ 1 & u_2 & v_2 \\ 1 & u_3 & v_3 \end{vmatrix} \right) \quad (2.57)$$

where l is the distance between P_2 and P_3 (see Figure 2.8).

The displacement (u, v) in each time step is small due to the small time step. Therefore, every multiply

$$u_k \cdot v_l \quad k, l = 1, 2, 3$$

is a second order infinitely small.

Denote:

$$s_0 = \begin{vmatrix} 1 & x_1 & y_1 \\ 1 & x_2 & y_2 \\ 1 & x_3 & y_3 \end{vmatrix} \quad (2.58)$$

and neglecting second order infinitely small components, Δ can be expressed as

$$\begin{aligned} \Delta &= s_0 + (y_2 - y_3 \quad x_3 - x_2) \begin{Bmatrix} u_1 \\ v_1 \end{Bmatrix} + (y_3 - y_1 \quad x_1 - x_3) \begin{Bmatrix} u_2 \\ v_2 \end{Bmatrix} + (y_1 - y_2 \quad x_2 - x_1) \begin{Bmatrix} u_3 \\ v_3 \end{Bmatrix} \\ &= s_0 + (y_2 - y_3 \quad x_3 - x_2) [T_i(x_1, y_1)] \{D_i\} \\ &\quad + (y_3 - y_1 \quad x_1 - x_3) [T_j(x_2, y_2)] \{D_j\} \\ &\quad + (y_1 - y_2 \quad x_2 - x_1) [T_j(x_3, y_3)] \{D_j\} \end{aligned} \quad (2.59)$$

Denote:

$$\{H\} = \frac{1}{l} [T_i(x_1, y_1)]^T \begin{Bmatrix} y_2 - y_3 \\ x_3 - x_2 \end{Bmatrix} \quad (2.60)$$

$$\{G\} = \frac{1}{l} [T_j(x_2, y_2)]^T \begin{Bmatrix} y_3 - y_1 \\ x_1 - x_3 \end{Bmatrix} + \frac{1}{l} [T_j(x_3, y_3)]^T \begin{Bmatrix} y_1 - y_2 \\ x_2 - x_1 \end{Bmatrix} \quad (2.61)$$

the entrance distance becomes:

$$d_n = \frac{s_0}{l} + \{H\}^T \{D_i\} + \{G\}^T \{D_j\} \quad (2.62)$$

and the strain energy becomes:

$$\begin{aligned} \Pi_n &= \frac{k_n}{2} \left(\frac{s_0}{l} + \{H\}^T \{D_i\} + \{G\}^T \{D_j\} \right)^2 \\ &= \frac{k_n}{2} [\{D_i\}^T \{H\} \{H\}^T \{D_i\} + \{D_j\}^T \{G\} \{G\}^T \{D_j\} + 2\{D_i\}^T \{H\} \{G\}^T \{D_j\} \\ &\quad + 2\frac{s_0}{l} \{D_i\}^T \{H\} + 2\frac{s_0}{l} \{D_j\}^T \{G\} + \left(\frac{s_0}{l} \right)^2] \end{aligned} \quad (2.63)$$

Therefore,

$$\begin{aligned} k_n \{H_{i(r)}\} \{H_{i(s)}\}^T &\rightarrow [K_{i(r)i(s)}] & r, s = 1, 2, 3 \\ k_n \{H_{i(r)}\} \{G_{j(s)}\}^T &\rightarrow [K_{i(r)j(s)}] & r, s = 1, 2, 3 \\ k_n \{G_{j(r)}\} \{H_{i(s)}\}^T &\rightarrow [K_{j(r)i(s)}] & r, s = 1, 2, 3 \\ k_n \{G_{j(r)}\} \{G_{j(s)}\}^T &\rightarrow [K_{j(r)j(s)}] & r, s = 1, 2, 3 \end{aligned} \quad (2.64)$$

are the element [6x6] matrices composed of 9 [2x2] matrices which are assembled into the global stiffness matrix $[K_e]$ according to the elements' nodes, and

$$\begin{aligned} -k_n \left(\frac{s_0}{l} \right) \{H_{i(r)}\} &\rightarrow \{F_{i(r)}\} & r = 1, 2, 3 \\ -k_n \left(\frac{s_0}{l} \right) \{G_{j(r)}\} &\rightarrow \{F_{j(r)}\} & r = 1, 2, 3 \end{aligned} \quad (2.65)$$

are the element {6x1} load vectors composed of 3 {2x1} vectors which are assembled into the global loading vector $\{F\}$ according to the elements' nodes

2.4.3 Shear Contact Matrix

For the case of lock contact, in addition to the normal spring, a shear spring is added in order to prevent tangential displacement between the vertex P_1 of element i to its corresponding entrance line P_2P_3 of element j (element i and element j are located in different sides of the discontinuity). An illustration of the procedure of adding shear spring is shown in Figure 2.9.

The strain energy of the shear spring is:

$$\Pi_s = \frac{k_s d_s^2}{2} \quad (2.66)$$

where d_s is the sliding distance, and k_s is the shear springs stiffness which is formulated in the computer program to $\frac{2}{5}k_n$.

Assume $P_0 (x_0, y_0)$ is the projection point of vertex P_1 on entrance line P_2P_3 (Figure 2.9), its coordinates and displacements expressed as:

$$\begin{aligned} x_0 &= (1-t_0)x_2 + t_0x_3 \\ y_0 &= (1-t_0)y_2 + t_0y_3 \\ u_0 &= (1-t_0)u_2 + t_0u_3 \\ v_0 &= (1-t_0)v_2 + t_0v_3 \end{aligned} \quad (2.67)$$

where $t_0 \{0 < t_0 < 1\}$ is the distance P_2P_0 normalized by l .

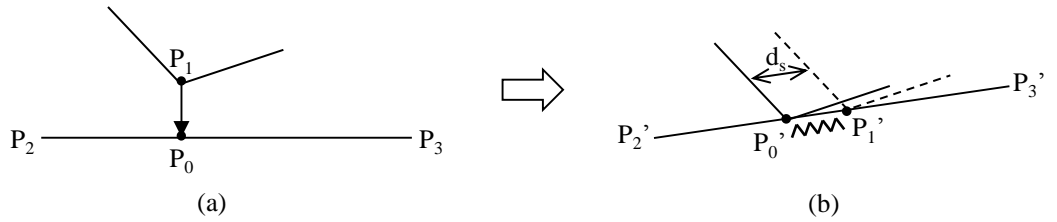


Figure 2.9. Illustration of the shear spring insertion procedure in NMM: contact configuration at a) the beginning of the time step; and b) the end of the time step. The dashed line represents the location of vertex P_1 if a shear spring is not added (Modified after Shi (1996a)).

The shear displacement of P_0 and P_1 along line P_2P_3 is

$$\begin{aligned} d_s &= \frac{1}{l} \overline{P_0'P_1'} \cdot \overline{P_2'P_3'} \\ &= \frac{1}{l} (x_1 + u_1 - (x_0 + u_0) \quad y_1 + v_1 - (y_0 + v_0)) \begin{Bmatrix} x_3 + u_3 - (x_2 + u_2) \\ y_3 + v_3 - (y_2 + v_2) \end{Bmatrix} \end{aligned} \quad (2.68)$$

Denote:

$$\tilde{S}_o = (x_1 - x_0 + y_1 - y_0) \begin{Bmatrix} x_3 - x_2 \\ y_3 - y_2 \end{Bmatrix} \quad (2.69)$$

neglecting second order infinitesimally small multiplies

$$u_1 \cdot (u_3 - u_2), v_1 \cdot (v_3 - v_2)$$

and substituting expression (2.67) for (x_0, y_0) and (u_0, v_0) gives

$$\begin{aligned}
d_s = & \frac{\tilde{S}_0}{l} + \frac{1}{l} \begin{pmatrix} x_3 - x_2 & y_3 - y_2 \end{pmatrix} \begin{Bmatrix} u_1 \\ v_1 \end{Bmatrix} \\
& + \frac{1}{l} \begin{pmatrix} -x_1 + 2(1-t_0)x_2 - (1-2t_0)x_3 & -y_1 + 2(1-t_0)y_2 - (1-2t_0)y_3 \end{pmatrix} \begin{Bmatrix} u_2 \\ v_2 \end{Bmatrix} \\
& + \frac{1}{l} \begin{pmatrix} x_1 + (2t_0-1)x_2 - 2t_0x_3 & y_1 + (2t_0-1)y_2 - 2t_0y_3 \end{pmatrix} \begin{Bmatrix} u_3 \\ v_3 \end{Bmatrix}
\end{aligned} \quad (2.70)$$

Denote:

$$\{\tilde{H}\} = \frac{1}{l} [T_i(x_1, y_1)]^T \begin{Bmatrix} x_3 - x_2 \\ y_3 - y_2 \end{Bmatrix} \quad (2.71)$$

$$\begin{aligned}
\{\tilde{G}\} = & \frac{1}{l} [T_j(x_2, y_2)]^T \begin{Bmatrix} -x_1 + 2(1-t_0)x_2 - (1-2t_0)x_3 \\ -y_1 + 2(1-t_0)y_2 - (1-2t_0)y_3 \end{Bmatrix} \\
& + \frac{1}{l} [T_j(x_3, y_3)]^T \begin{Bmatrix} x_1 + (2t_0-1)x_2 - 2t_0x_3 \\ y_1 + (2t_0-1)y_2 - 2t_0y_3 \end{Bmatrix}
\end{aligned} \quad (2.72)$$

the sliding distance becomes:

$$d_s = \frac{S_0}{l} + \{\tilde{H}\}^T \{D_i\} + \{\tilde{G}\}^T \{D_j\} \quad (2.73)$$

and the strain energy of the shear springs becomes:

$$\begin{aligned}
\Pi_s = & \frac{k_s}{2} \left(\frac{s_0}{l} + \{\tilde{H}\}^T \{D_i\} + \{\tilde{G}\}^T \{D_j\} \right)^2 \\
= & \frac{k_s}{2} [\{D_i\}^T \{\tilde{H}\} \{\tilde{H}\}^T \{D_i\} + \{D_j\}^T \{\tilde{G}\} \{\tilde{G}\}^T \{D_j\} + 2\{D_i\}^T \{\tilde{H}\} \{\tilde{G}\}^T \{D_j\} \\
& + 2\frac{s_0}{l} \{D_i\}^T \{\tilde{H}\} + 2\frac{s_0}{l} \{D_j\}^T \{\tilde{G}\} + \left(\frac{s_0}{l}\right)^2]
\end{aligned} \quad (2.74)$$

Therefore,

$$\begin{aligned}
k_s \{\tilde{H}_{i(r)}\} \{\tilde{H}_{i(s)}\}^T & \rightarrow [K_{i(r)i(s)}] & r, s = 1, 2, 3 \\
k_s \{\tilde{H}_{i(r)}\} \{\tilde{G}_{j(s)}\}^T & \rightarrow [K_{i(r)j(s)}] & r, s = 1, 2, 3 \\
k_s \{\tilde{G}_{j(r)}\} \{\tilde{H}_{i(s)}\}^T & \rightarrow [K_{j(r)i(s)}] & r, s = 1, 2, 3 \\
k_s \{\tilde{G}_{j(r)}\} \{\tilde{G}_{j(s)}\}^T & \rightarrow [K_{j(r)j(s)}] & r, s = 1, 2, 3
\end{aligned} \quad (2.75)$$

are the element [6x6] matrices composed of 9 [2x2] matrices which are assembled into the global stiffness matrix $[K_e]$ according to the elements' nodes, and

$$\begin{aligned}
-k_s \left(\frac{s_0}{l} \right) \{ \tilde{H}_{i(r)} \} &\rightarrow \{ F_{i(r)} \}, & r = 1, 2, 3 \\
-k_s \left(\frac{s_0}{l} \right) \{ \tilde{G}_{j(r)} \} &\rightarrow \{ F_{j(r)} \}, & r = 1, 2, 3
\end{aligned} \tag{2.76}$$

are the element $\{6 \times 1\}$ load vectors composed of 3 $\{2 \times 1\}$ vectors which are assembled into the global loading vector $\{F\}$ according to the elements' nodes

2.4.4 Friction force matrix

According to Coulomb's law, when sliding between two sides of the boundary contacts is allowed, in addition to the normal spring a pair of frictional forces is added. Based on Coulomb's law, the frictional force is calculated as:

$$f = \text{sign} \cdot k_n d_n \tan(\phi) \tag{2.77}$$

where $\tan(\phi)$ is the friction coefficient, and sign is assigned as “+” or “-” according to the direction of the relative sliding (positive when the vertex P_1 slides in the direction P_2 to P_3).

The potential energy due to friction force f at P_1 on element i is:

$$\Pi_{fi} = f(u_1 \quad v_1) \frac{1}{l} \begin{Bmatrix} x_3 - x_2 \\ y_3 - y_2 \end{Bmatrix} \tag{2.78}$$

and the potential energy due to friction force f at P_0 on element j is:

$$\Pi_{fj} = -f(u_0 \quad v_0) \frac{1}{l} \begin{Bmatrix} x_3 - x_2 \\ y_3 - y_2 \end{Bmatrix} \tag{2.79}$$

where $\frac{1}{l} \begin{Bmatrix} x_3 - x_2 \\ y_3 - y_2 \end{Bmatrix}$ is the unit vector of $\overline{P_2 P_3}$.

Denote:

$$\{\overline{H}\} = \frac{1}{l} [T_i(x_1, y_1)]^T \begin{Bmatrix} x_3 - x_2 \\ y_3 - y_2 \end{Bmatrix} \tag{2.80}$$

$$\{\overline{G}\} = \frac{1}{l} [T_i(x_0, y_0)]^T \begin{Bmatrix} x_3 - x_2 \\ y_3 - y_2 \end{Bmatrix} \tag{2.81}$$

the potential energy becomes:

$$\Pi_f = f \{D_i\}^T \{\overline{H}\} - f \{D_i\}^T \{\overline{G}\} \tag{2.82}$$

Therefore,

$$\begin{aligned}
 f\{\bar{H}_{i(r)}\} &\rightarrow \{F_{i(r)}\}, & r = 1, 2, 3 \\
 -f\{\bar{G}_{j(r)}\} &\rightarrow \{F_{j(r)}\}, & r = 1, 2, 3
 \end{aligned}
 \tag{2.83}$$

are the element $\{6 \times 1\}$ load vectors composed of 3 $\{2 \times 1\}$ vectors which are assembled into the global loading vector $\{F\}$ according to the elements' nodes

2.5 Two dimensional simplex integration

For the manifold method, the manifold elements with their arbitrary shape are the integration zones. Therefore, the integration scheme of FEM which is suitable for triangular and rectangular elements are not applicable, and the analytical simplex integration of Shi (Shi, 1996b), where the arbitrary domain of integration is converted into several oriented (positive or negative) triangles, is adopted. An illustration of triangulation of manifold element with the sign convention is shown in Figure 2.10.

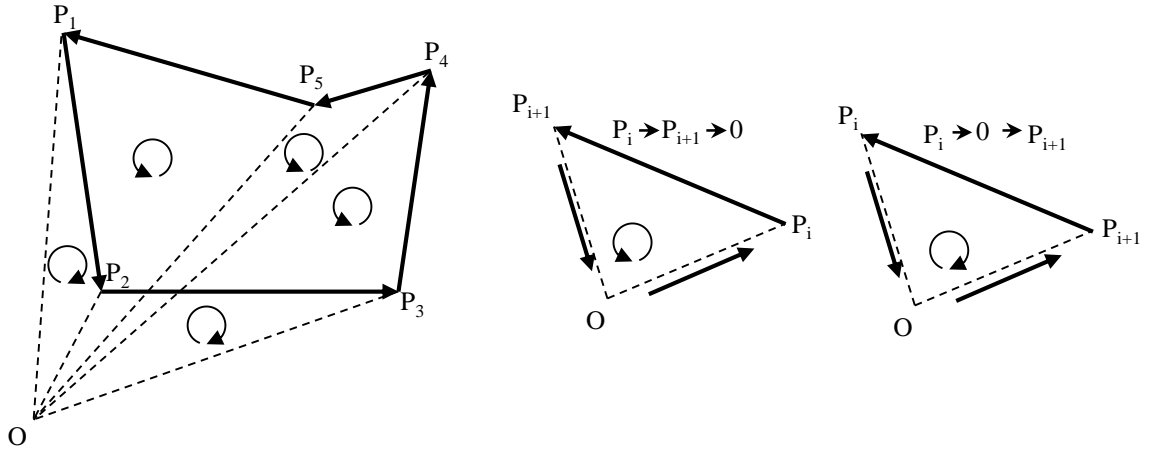


Figure 2.10. Triangulation of manifold element with the sign convection: positive-counterclockwise, negative- clockwise (Modified after Shi (1996b)).

The analytical solutions for the six integrations which are required in the manifold method are as following:

$$S^e = \iint_A dx dy = \frac{1}{2} \sum_{i=1}^m \begin{vmatrix} 1 & x_0 & y_0 \\ 1 & x_i & y_i \\ 1 & x_{i+1} & y_{i+1} \end{vmatrix}
 \tag{2.84}$$

$$S_x^e = \iint_A x dx dy = \frac{s^e}{3} \sum_{i=1}^m (x_0 + x_i + x_{i+1})
 \tag{2.85}$$

$$S_y^e = \iint_A y dx dy = \frac{s^e}{3} \sum_{i=1}^m (y_0 + y_i + y_{i+1}) \quad (2.86)$$

$$S_{xx}^e = \iint_A x^2 dx dy = \frac{s^e}{6} \sum_{i=1}^m (x_0^2 + x_i^2 + x_{i+1}^2 + x_i x_0 + x_{i+1} x_0 + x_i x_{i+1}) \quad (2.87)$$

$$S_{yy}^e = \iint_A y^2 dx dy = \frac{s^e}{6} \sum_{i=1}^m (y_0^2 + y_i^2 + y_{i+1}^2 + y_i y_0 + y_{i+1} y_0 + y_i y_{i+1}) \quad (2.88)$$

$$S_{xy}^e = \iint_A xy dx dy = \frac{s^e}{12} \sum_{i=1}^m (2x_0 y_0 + 2x_i y_i + 2x_{i+1} y_{i+1} + x_i y_0 + x_{i+1} y_0 + x_0 y_i + x_0 y_{i+1} + x_i y_{i+1} + x_{i+1} y_i) \quad (2.89)$$

where x_0 and y_0 are the coordinates of the arbitrary chosen point O , and m is the number of the vertices in the manifold element.

2.6 Equation solver and open-close iteration for equilibrium equations

The manifold method computations follow a time step marching scheme. For each time step the following stages are applied:

- 1) Several physical and geometrical parameters are inherited from the previous time step:
 - a) stresses of each element; b) strains of each element; c) velocities of each element (only for dynamic simulation); d) geometry of the joint boundaries and elements; and e) all closed contacts parameters, i.e. i) the contact vertex and edge; ii) the position of contact point; iii) the normal displacement and normal force; iv) the shear displacement and shear force; and v) locking or sliding as contact state.
- 2) Calculation of the continuous material contribution to general equilibrium equation.
- 3) Open-close iterations which includes 3 stages:
 - a) Calculation of the discontinuities contribution to general equilibrium equation.
 - b) The global equation is solved by the “SOR” (successive over relaxation method), which is a numeric method for solving linear equations.
 - c) A check that two conditions are fulfilled in all contacts: i) no-penetrations in the open contacts; ii) no-tensions in the contacts with normal springs. If the two conditions are fulfilled the computation proceeds to the next time step. Otherwise, the equilibrium equation is updated (stage 3b), i.e. if a contact has a tensile contact force from the normal spring, the two sides will separate after the removal of this stiff spring, if the vertex penetrated the edge in other side of the contact, a stiff spring is applied. Then, the equilibrium equation is solved again (stage 3b). If the

two conditions are not fulfilled after six times of open-close iterations, the time step will be reduced to one third, and the procedure continues from stage 2.

- 4) A check that the maximum displacements of all points in the problem domain (d_{max}) at a given time step are less than a pre-defined limit ρ . If this condition is not fulfilled, the time step size ($\Delta(t)$) is reduced according to the following equation:

$$\Delta(t) = \frac{\Delta(t)}{\sqrt{\frac{d_{max}}{\rho}}} \quad (2.90)$$

and the procedure continues from stage 2.

2.7 NMM numeric implementation

Computer implementation of NMM allows control over the analysis procedure through a set of user specified control parameters:

- 1) Dynamic control parameter (k01) – defines the type of the analysis required, from static to fully dynamic. For static analysis the velocity of each element is set to zero at the beginning of each time step, k01=0. In the case of the dynamic analysis the velocity of each element at the end of a time step is fully transferred to the next time step, k01=1.
- 2) Upper limit of time step size (g1) – The maximum time interval that can be used in a time step, should be chosen small enough so that the second order displacements can be neglected, that the SOR iteration will converge in less than 30 iterations, and that the open-close iterations will converge in less than 6 iterations.
- 3) Assumed maximum displacement ratio (g2) – The calculated maximum displacement within a time step is limited to an assumed maximum displacement in order to ensure infinitesimal displacement within a time step. The maximum displacement within a time step is limited to $g2*H$ ($g2*H = \rho$), where H is half the height of the analysis domain. If $g2$ is too large there are too many unnecessary contacts, if $g2$ is too small unrealistic inter-block penetration can occur.
- 4) Penalty value (g0) – is the stiffness of contact springs ($g0=k_n$), used to enforce contact constraints between blocks.
- 5) Mesh density (e) – defined as the higher number between the following two options:
 - 1) number of triangular element layers in half domain height, or
 - 2) number of triangular elements in half domain width.

Chapter 3- Numerical code verification

In this chapter, the NMM is verified using four analytical solutions. In three static problems, the NMM program capability of accurately solving the stresses and displacements in a homogeneous elastic domain (circular hole in an infinite plate and beam under concentrate load and volumetric force) and in inhomogeneous elastic domain (layered plate) is examined. In one dynamic problem, the NMM program ability to model frictional contacts between two blocks (block on an incline) is examined. At this problem, the influence of three numerical control parameters on the accuracy of the NMM results is examined too.

3.1 Layered plate subjected to gravity

The first verification is for the case of a layered plate subjected to gravity. The plate resembles a layered geological medium which experienced deformation over geologic times due to overburden stress. The analytical solution for the horizontal and the vertical stresses and the vertical displacements under plane stress conditions is developed. A plane strain solution can be obtained when the elastic constants, E and ν , in the plane stress solution are modified by equations (2.20) and (2.21). The solution is performed for a special case where lateral strain is assumed to be zero ($\varepsilon_{xx} = 0$), due to the typically infinite extent of the geological strata at depth in the field. The layout of the problem is illustrated in Figure 3.1 where γ is the unit weight [kN/m^3] of the material. Regarding the geometry of the model (x - horizontal axis, y - vertical axis, z - out of plane axis), y is the vertical distance from the origin, located at midsection at the bottom of the plate. An analytical solution for the case of continuous plate (Figure 3.2) is developed first, and is generalized later for the case of a layered plate.

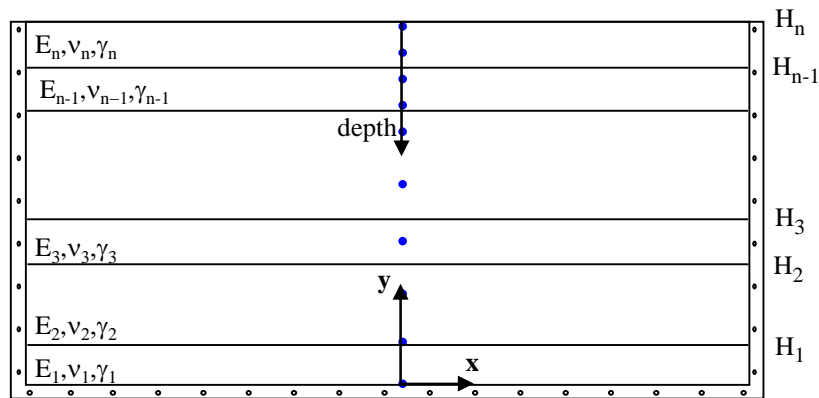


Figure 3.1. Layout of the modeled problem consisting of an elastic plate divided into n layers and constrained between stiff boundaries at sides and bottom.

3.1.1 Analytical solution:

3.1.1.1 Continuous plate subjected to gravity:

The increase of vertical stress with depth is:

$$\sigma_{yy} = \gamma h = \gamma(H - y) \quad (3.1)$$

From Hooke's law, the relationship between stress and strain is:

$$\varepsilon_{xx} = \frac{\sigma_{xx} - \nu(\sigma_{yy} + \sigma_{zz})}{E} = \frac{\sigma_{xx} - \nu\sigma_{yy}}{E} = 0 \Rightarrow \sigma_{xx} = \nu \cdot \sigma_{yy} \quad (3.2)$$

The vertical strain is:

$$\frac{dV}{dy} = \varepsilon_{yy} = \frac{\sigma_{yy} - \nu\sigma_{xx}}{E} = \frac{\sigma_{yy}}{E} \cdot (1 - \nu^2) = \frac{1 - \nu^2}{E} \cdot \gamma(H - y) \quad (3.3)$$

and the total vertical displacement is therefore,

$$V = \int_0^Y \frac{(1 - \nu^2)}{E} \gamma(H - y) dy = \frac{(1 - \nu^2)}{E} \gamma \int_0^y (H - y) dy = \frac{(1 - \nu^2)}{E} \gamma \left(Hy - \frac{y^2}{2} \right) \quad (3.4)$$

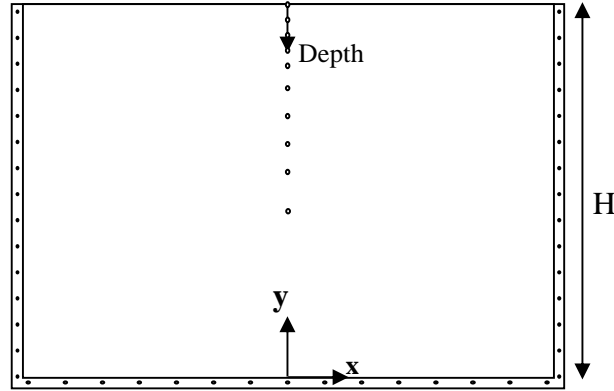


Figure 3.2. Layout of the modeled problem consisting of a continuous elastic plate constrained between stiff boundaries at sides and bottom.

3.1.1.2 Generalization for a layered medium

For the case of a plate with n layers the vertical stress can be expressed incrementally as:

$$\sigma_{yy} = \begin{cases} \gamma_n(H_n - H_{n-1}) + \gamma_{n-1}(H_{n-1} - H_{n-2}) + \dots + \gamma_1(H_1 - y) & , y < H_1 \\ \vdots & \\ \gamma_n(H_n - H_{n-1}) + \gamma_{n-1}(H_{n-1} - y) & , H_{n-2} < H_{n-1} \\ \gamma_n(H_n - y) & , H_{n-1} < H_n \end{cases} \quad (3.5)$$

and the horizontal stress can be expressed as:

$$\sigma_{xx} = \begin{cases} \nu_1 [\gamma_n (H_n - H_{n-1}) + \gamma_{n-1} (H_{n-1} - H_{n-2}) + \dots + \gamma_1 (H_1 - y)] & , y < H_1 \\ \vdots & \\ \nu_{n-1} [\gamma_n (H_n - H_{n-1}) + \gamma_{n-1} (H_{n-1} - y)] & , H_{n-2} < H_{n-1} \\ \nu_n [\gamma_n (H_n - y)] & , H_{n-1} < H_n \end{cases} \quad (3.6)$$

The vertical strain is therefore:

$$\frac{dV}{dy} = \begin{cases} \frac{1-\nu_1^2}{E_1} [\gamma_n (H_n - H_{n-1}) + \gamma_{n-1} (H_{n-1} - H_{n-2}) + \dots + \gamma_1 (H_1 - y)] & , y < H_1 \\ \vdots & \\ \frac{1-\nu_{n-1}^2}{E_{n-1}} [\gamma_n (H_n - H_{n-1}) + \gamma_{n-1} (H_{n-1} - y)] & , H_{n-2} < H_{n-1} \\ \frac{1-\nu_n^2}{E_n} [\gamma_n (H_n - y)] & , H_{n-1} < H_n \end{cases} \quad (3.7)$$

and finally, the total vertical displacement is:

$$V = \begin{cases} \frac{1-\nu_1^2}{E_1} \int_0^y [\gamma_n (H_n - H_{n-1}) + \gamma_{n-1} (H_{n-1} - H_{n-2}) + \dots + \gamma_1 (H_1 - s)] ds & , y < H_1 \\ \vdots & \\ \frac{1-\nu_1^2}{E_1} \int_0^{H_1} [\gamma_n (H_n - H_{n-1}) + \gamma_{n-1} (H_{n-1} - H_{n-2}) + \dots + \gamma_1 (H_1 - s)] ds + \dots \\ \quad + \frac{1-\nu_{n-1}^2}{E_{n-1}} \int_{H_{n-2}}^y [\gamma_n (H_n - H_{n-1}) + \gamma_{n-1} (H_{n-1} - s)] ds & , H_{n-2} < y < H_{n-1} \\ \frac{1-\nu_1^2}{E_1} \int_0^{H_1} [\gamma_n (H_n - H_{n-1}) + \gamma_{n-1} (H_{n-1} - H_{n-2}) + \dots + \gamma_1 (H_1 - s)] ds + \dots \\ \quad + \frac{1-\nu_n^2}{E_n} \int_{H_{n-1}}^y [\gamma_n (H_n - s)] ds & , H_{n-1} < H_n \end{cases}$$

$$\begin{aligned}
& \left\{ \begin{aligned} & \frac{1-\nu_1^2}{E_1} \left[\gamma_n(H_n - H_{n-1}) + \gamma_{n-1}(H_{n-1} - H_{n-2}) + \dots + \gamma_1 H_1 \right] s - \gamma_1 \frac{s^2}{2} \Bigg|_0^y, y < H_1 \\ & \vdots \\ & \frac{1-\nu_1^2}{E_1} \left[\gamma_n(H_n - H_{n-1}) + \gamma_{n-1}(H_{n-1} - H_{n-2}) + \dots + \gamma_1 H_1 \right] s - \gamma_1 \frac{s^2}{2} \Bigg|_0^{H_1} + \dots \\ & + \frac{1-\nu_{n-1}^2}{E_{n-1}} \left[\gamma_n(H_n - H_{n-1}) + \gamma_{n-1} H_{n-1} \right] s - \gamma_{n-1} \frac{s^2}{2} \Bigg|_{H_{n-2}}^y, H_{n-2} < y < H_{n-1} \\ & \frac{1-\nu_1^2}{E_1} \left[\gamma_n(H_n - H_{n-1}) + \gamma_{n-1}(H_{n-1} - H_{n-2}) + \dots + \gamma_1 H_1 \right] s - \gamma_1 \frac{s^2}{2} \Bigg|_0^{H_1} + \dots \\ & + \frac{1-\nu_n^2}{E_n} \left[\gamma_n H_n s - \gamma_n \frac{s^2}{2} \right]_{H_{n-1}}^y, H_{n-1} < H_n \end{aligned} \right. \\
& \tag{3.8}
\end{aligned}$$

where s is a variable for the specific integral.

3.1.2 Analytical versus NMM solution

In order to verify the NMM for the case of a layered plate, the case of an elastic plate divided into 3 sub-layers is simulated with NMM. The plate is constrained between three fixed blocks at the sides and bottom. Fixed points are distributed along those three blocks (one per element) in order to eliminate any displacement of the blocks. The mechanical parameters of the layers and the numerical parameters in the simulation are presented in Table 3.1. The NMM model at the end of a simulation with scaled principal stress trajectories delineated in red, measurement points location, and the dimension of the model are shown in Figure 3.3. The agreement between the analytical and numerical solutions is determined by the numerical relative error, which is defined in a conventional manner as:

$$E_N = \left| \frac{d - d_N}{d} \right| \cdot 100 \tag{3.9}$$

where d and d_N are analytical and numerical solutions, respectively.

The comparisons between analytically derived and numerically obtained principal stresses are shown in Figure 3.4. A good agreement is obtained, with relative errors below 2% at 8 measurements points, and with relative error of 6.5% at depth of 100 m (Figure 3.5). At the surface of the model, the absolute values of the stresses are very small, and therefore, the relative error is much greater. The comparisons between analytically derived and numerically obtained vertical settlement are shown in Figure 3.6. A very good agreement is obtained, with

relative errors below 0.32% at 9 measurements points (Figure 3.7). At the bottom of the model, the vertical displacement is very small, and therefore, the relative error is much greater.

Table 3.1. Input parameters for NMM verification.

$K01$	$g2$	$g1$ [s]	$g0$ [kN/m]	E	E [GPa]	ν	γ [kN/m ³]
0	0.005	0.0005	50000000	20	$E_1=2$ $E_2=0.5$ $E_3=10$	$\nu_1=0.26$ $\nu_2=0.3$ $\nu_3=0.2$	$\gamma_1=16$ $\gamma_2=18$ $\gamma_3=21$

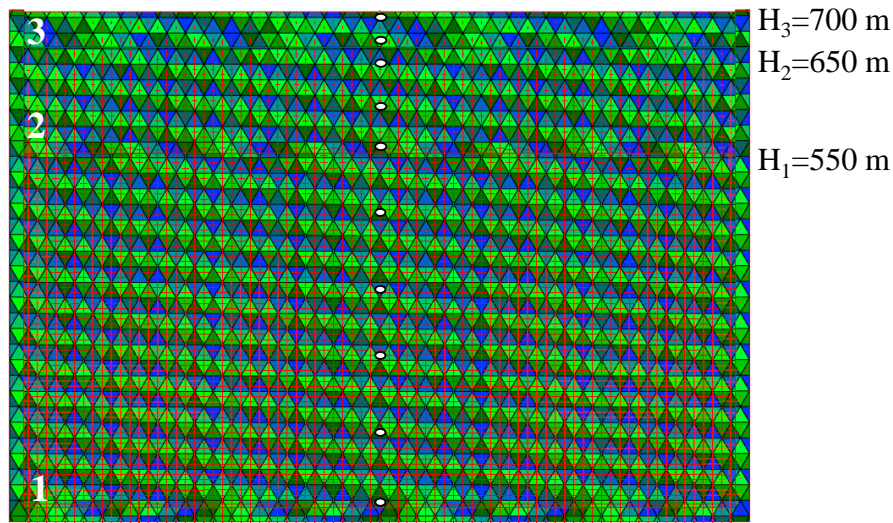


Figure 3.3. NMM model of Elastic plate divided into 3 sub-layers at the end of the simulation. Typical stress distribution result with scaled principal stress trajectories delineated in red.

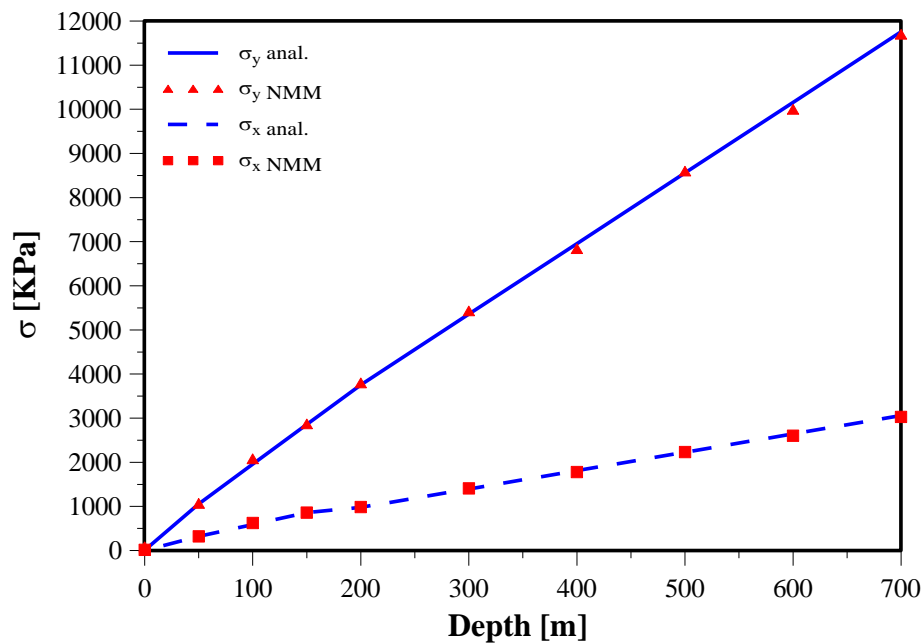


Figure 3.4. Comparison between results of analytical and numerical approaches: Vertical and horizontal stresses as a function of measurement point depth.

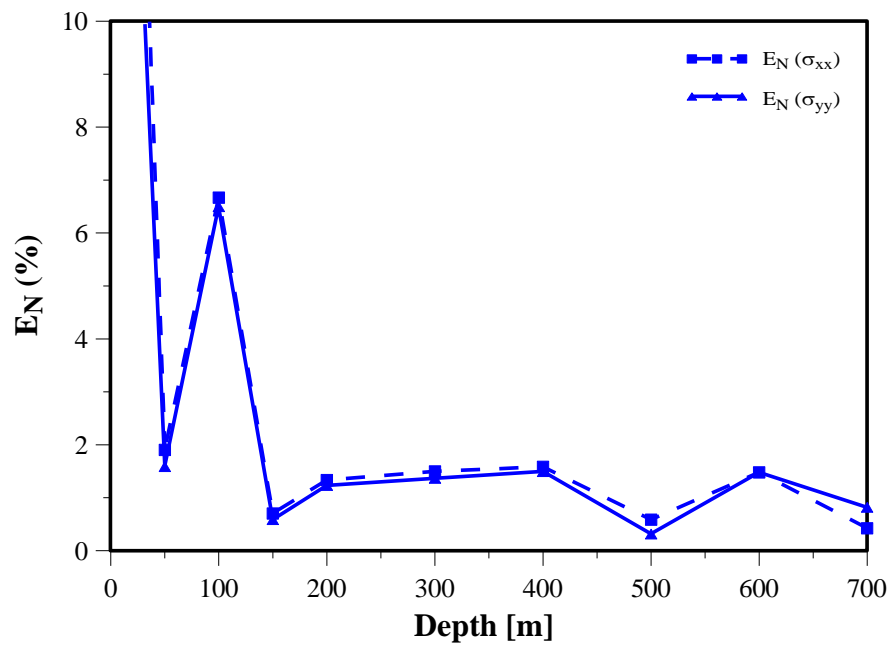


Figure 3.5. Relative errors of the stresses as a function of measurement point depth. The relative error at depth of 0.1 m is absent due figure scale.

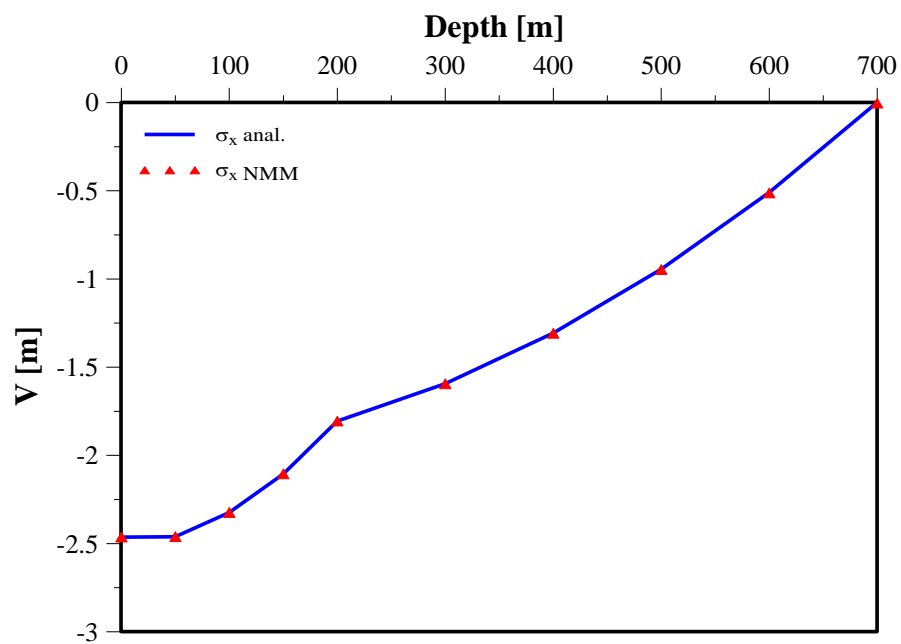


Figure 3.6. Comparison between results of analytical and numerical approaches: Vertical displacement as a function of measurement point depth.

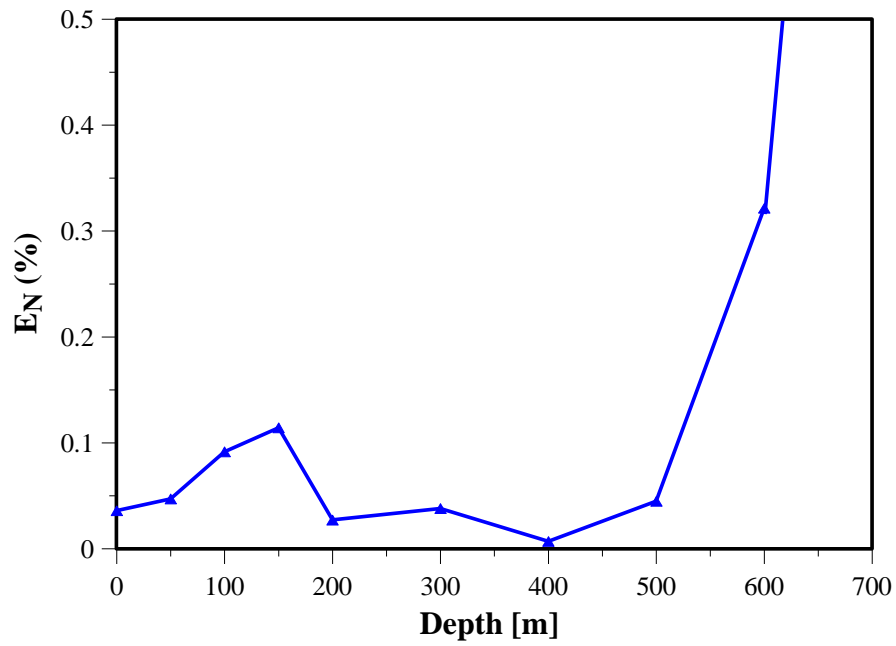


Figure 3.7. Relative errors of the vertical displacement as a function of measurement point depth. The relative error at the bottom of the model is absent due to figure scale.

3.2 Kirsch solution

In order to verify the NMM suitability for mining problems, the Kirsch solution (Kirsch, 1898) is adopted. Kirsch solution was developed for a circular hole in an infinite plate subjected to remote and constant principal stresses p and Kp as shown in Figure 3.8. It is used widely in tunneling applications, and assumes continuous, homogeneous, and linear elastic medium. (An, 2010) verified Kirsch solution for the stresses near the hole in a plate under uniaxial tension. However, She used a high mesh density (diameter of the hole contains 10 elements), which demands a long simulation. In this verification, a relatively sparse mesh (diameter contains 5 elements) is examined (Figure 3.9). In addition, the vertical displacements are examined too.

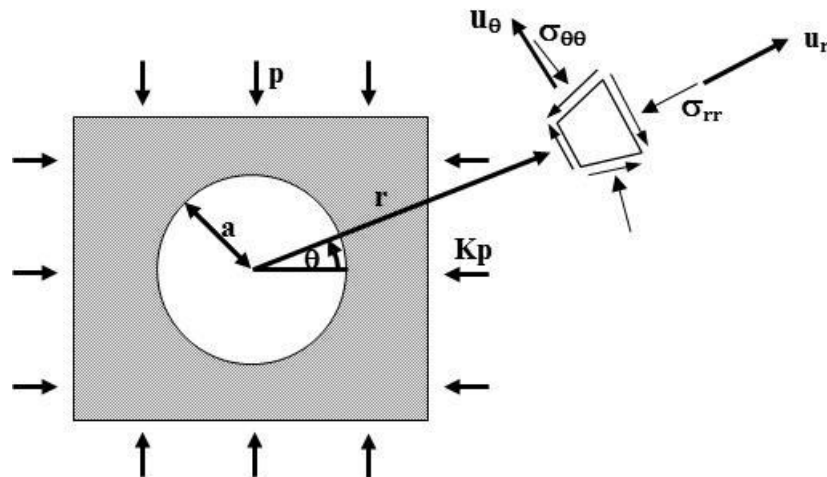


Figure 3.8. Sign convention for Kirsch solution; (after Brady and Brown (1993)).

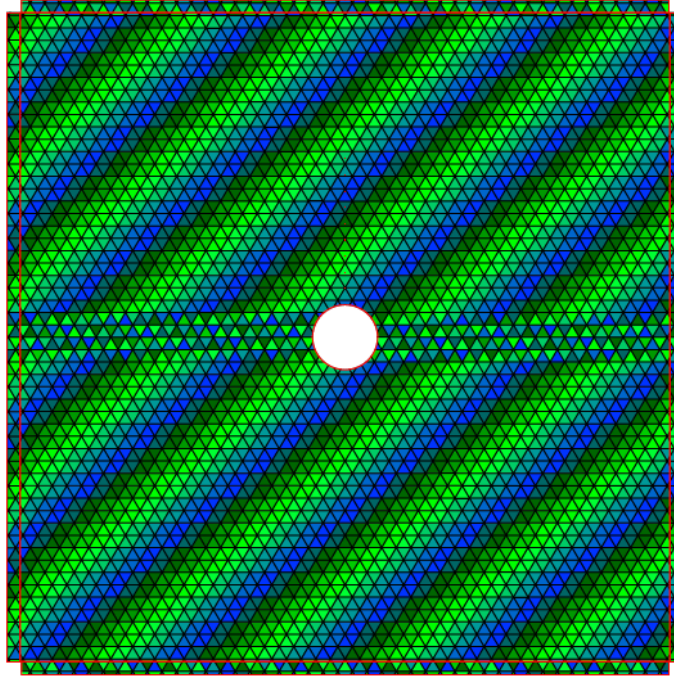


Figure 3.9. NMM model for continuous elastic plate with a hole in the center with mesh density of 30.

3.2.1 Analytical solution

Kirsch solution is expressed here in polar coordinates, and provides the stress (σ_θ , σ_r) and displacements (u_r , u_θ) components around the cavern as a function of r , θ and a , under plane strain conditions (for definition of r , θ and a see Figure 3.8):

$$\sigma_{rr} = \frac{P}{2} \left[(1+k) \cdot \left(1 - \frac{a^2}{r^2}\right) - (1-k) \cdot \left(1 - 4\frac{a^2}{r^2} + 3\frac{a^4}{r^4}\right) \cos 2\theta \right] \quad (3.10)$$

$$\sigma_{\theta\theta} = \frac{P}{2} \left[(1+k) \cdot \left(1 + \frac{a^2}{r^2}\right) + (1-k) \cdot \left(1 + 3\frac{a^4}{r^4}\right) \cos 2\theta \right] \quad (3.11)$$

$$u_r = -\frac{Pa^2}{4Gr} \left[(1+k) - (1-k) \cdot \left(4(1-\nu) - \frac{a^2}{r^2}\right) \cos 2\theta \right] \quad (3.12)$$

$$u_\theta = -\frac{Pa^2}{4Gr} \left[(1-k) \cdot \left(2(1-2\nu) + \frac{a^2}{r^2}\right) \sin 2\theta \right] \quad (3.13)$$

3.2.2 Analytical versus NMM solutions

The layout of the numerical model is shown in Figure 3.10. As in the previous verification, the horizontal stresses are generated due to the stiff boundaries at the sides of the model ($\varepsilon_{xx} = 0$). The mechanical and numerical parameters in the simulation are presented in Table 3.2 .

The comparisons between analytically derived and numerically obtained horizontal and vertical stresses are shown in Figure 3.11. The relative errors at the 9 measurement points are plotted in Figure 3.12. At the measurement point near the hole, the vertical stress is very small, and therefore, the relative error is much greater, and cannot be presented at the scale of the figure. The relative errors decrease with increasing distance from the center of the hole, and reach values below 9 % at distance of 2.5 radii from the center of the hole.

Table 3.2. Input parameters for NMM analysis.

$K01$	$g2$	$g1$ [s]	$g0$ [kN/m]	e	E [GPa]	ν	γ [kN/m ³]
0	0.005	0.0005	50000000	30	10	0.3	0

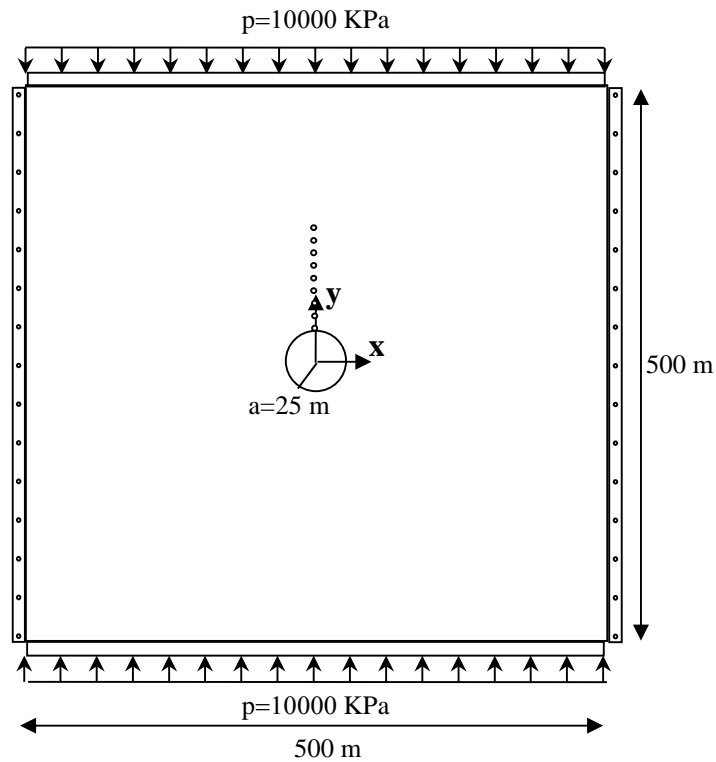


Figure 3.10. Layout of model for continuous elastic plate with a hole in the center under remote vertical stress and vertical stiff boundaries.

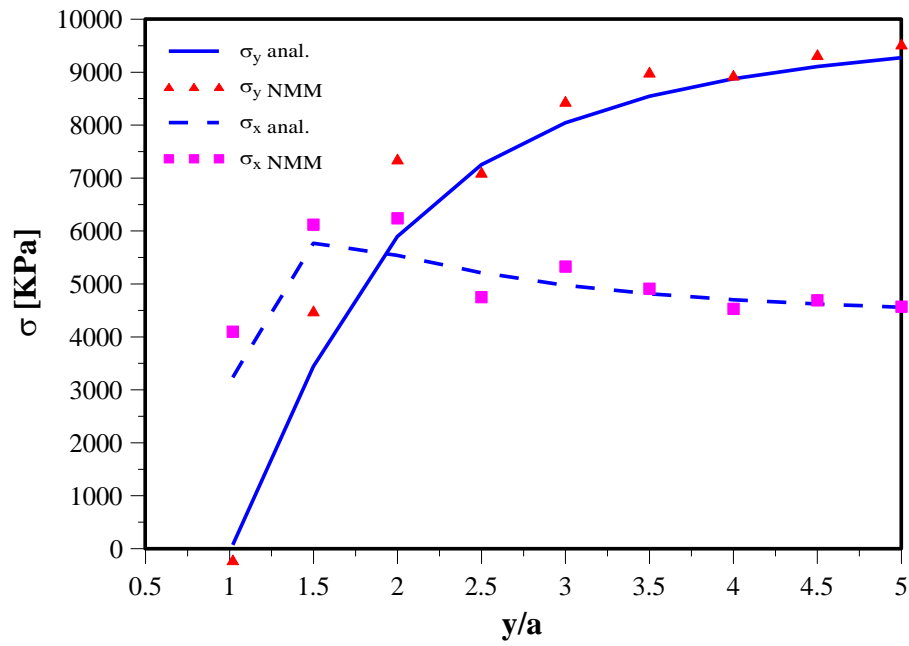


Figure 3.11 Comparison between results of analytical and numerical approaches: Vertical and horizontal stresses as a function of the vertical distance above the center of the hole normalized by the hole's radius.

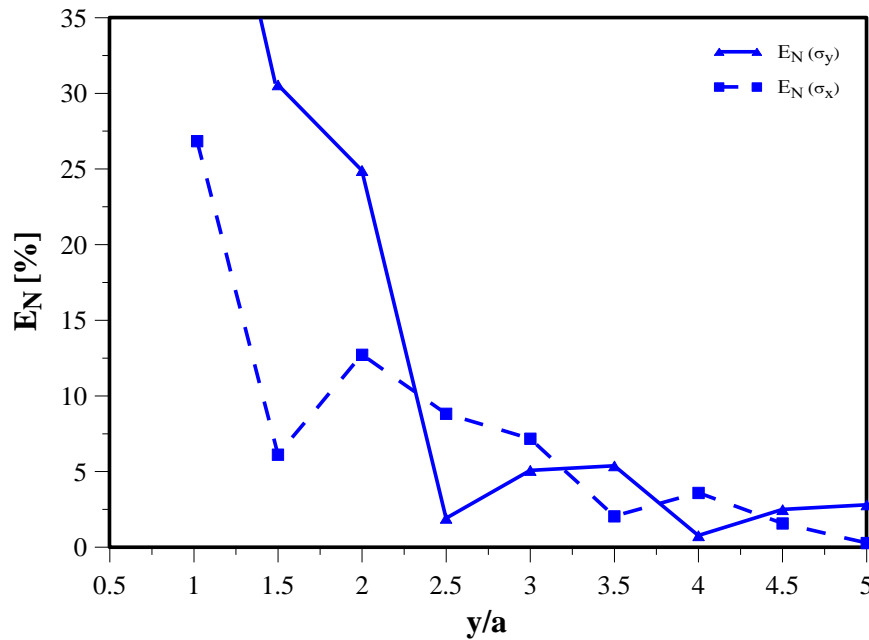


Figure 3.12. Relative errors of the stresses as a function of the vertical distance above the center of the hole normalized by the hole's radius. The relative error for vertical stress at distance 0f 1 radius above the center is absent due to figure scale.

The NMM solution for the vertical displacements above the hole contain two processes: the elastic deformation due to the vertical stress, which resembles the compaction of the rock column over geologic times due to overburden stress, and the vertical displacements due to the cavity only (as obtained with Kirsch solution). In order to compute only vertical displacements due to the cavity with NMM, two procedures can be applied:

1. Two simulations procedure: Subtraction of the elastic vertical displacements computed with NMM for a plate without a cavity from the vertical displacements computed with NMM for a plate containing a cavity.
2. Two stages procedure: The cavity is opened during the simulation, after the elastic vertical displacements have already been achieved, and subtraction of the elastic vertical displacements of the first stage from the vertical displacements at the end of the simulation. In order to apply this procedure with NMM, the original NMM was modified in this thesis to allow cavity excavation during the simulation. At the beginning of the simulation, a single block which possesses the same elastic properties as its surrounding replaces the cavity and simulation is performed until elastic vertical displacements are achieved (tunnel excavation). Then, the block is removed (tunnel excavation), and the simulation proceeds with the same loads as in the first stage.

The comparisons between analytically derived and numerically obtained (with the two procedures above) vertical displacements due to cavity are shown in Figure 3.13. A good agreement between analytic and numeric results is obtained, with relative errors below 8.2% Figure 3.14. Moreover, a very good agreement is achieved also between the two procedures, where the 2 simulation procedure is more accurate near the hole, and the 2 stages procedure is more accurate from a distance of 4 radii from the hole.

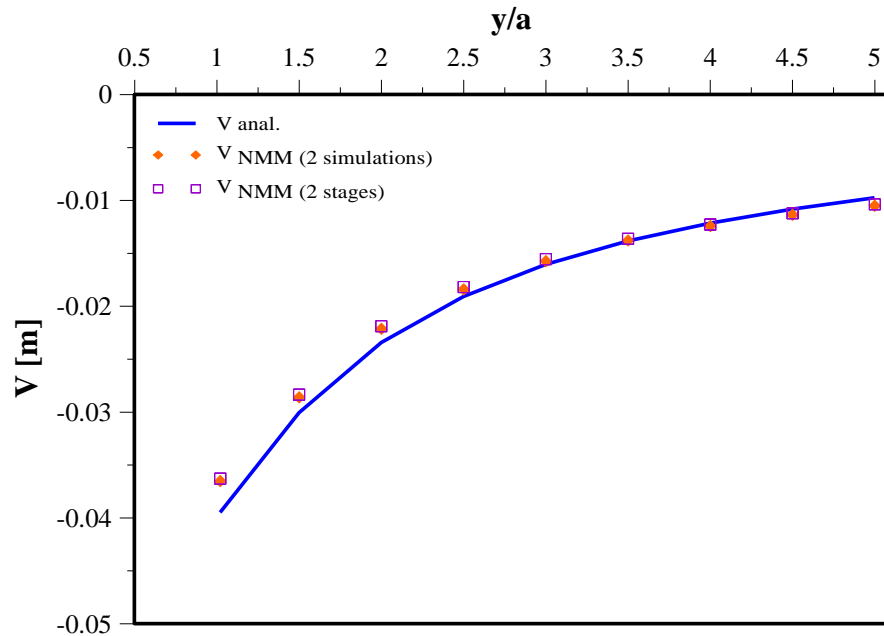


Figure 3.13. Comparison between results of analytical (blue line) and numerical approaches: Vertical displacement due to cavity as a function of the vertical distance above the center of the hole normalized by the hole's radius. The orange diamonds indicate the two simulation procedure, while the purple squares indicate the two stages procedure.

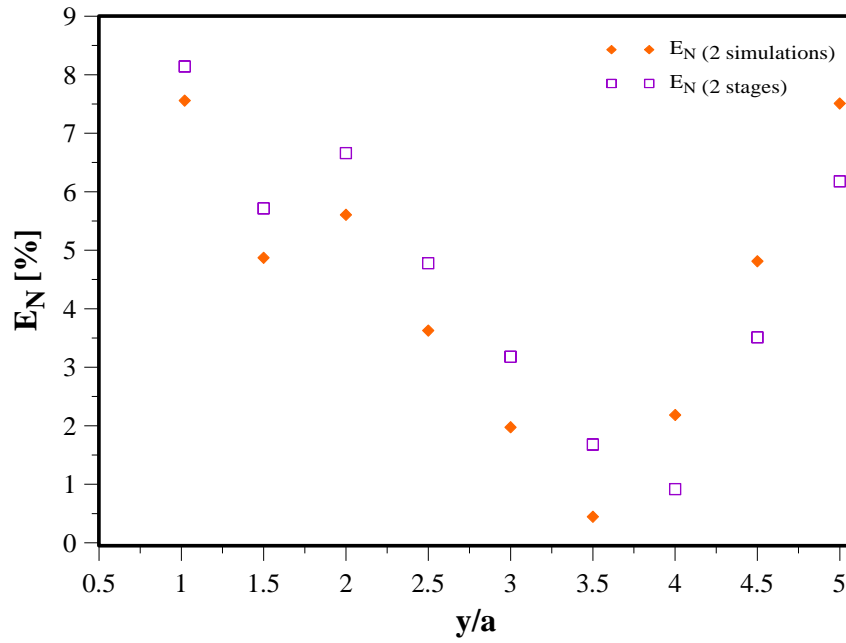


Figure 3.14. Relative errors of the vertical displacement with 2 simulation procedure (orange diamonds) and 2 stages procedure (purple squares) as a function of the vertical distance above the center of the hole normalized by the hole's radius.

3.3 Beam under concentrate load and volumetric force

In this static verification, the vertical displacements and the horizontal stresses along a beam are verified in order to test the NMM suitability for cases where long blocks are created due to the intersection of discontinuities. The layout of the beam with the measurement points is presented in Figure 3.15. The bases beneath the beam eliminate it only from downward displacement.

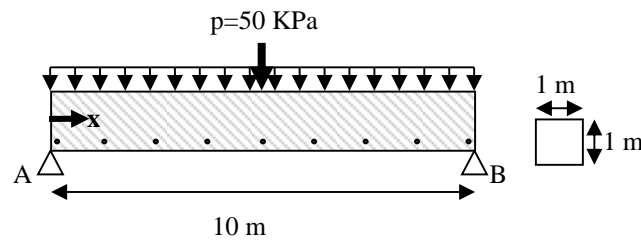


Figure 3.15. Beam under concentrate load and volumetric force.

3.3.1 Analytical solution

Equilibrium in the vertical direction and the symmetry of the problem give:

$$\sum F_y : A_y + B_y = 10\gamma + P \Rightarrow A_y = B_y = \frac{10\gamma + P}{2} \quad (3.14)$$

where A_y and B_y are the vertical forces [kN] of the foundations, and P is a concentrated load [kN].

From beam theory, the forth derivative of the vertical settlement is:

$$\frac{d^2V}{dx^2} \left(EI_{zz} \frac{d^2V}{dx^2} \right) = q(x) = \frac{P+10\gamma}{2} \langle x \rangle^{(-1)} - P \langle x-5 \rangle^{-1} - \gamma \langle x \rangle^0 + B \gamma \langle x-10 \rangle^{-1} \quad (3.15)$$

where I_{zz} is the second moment, x is the horizontal coordinate, and $\langle \rangle^n$ denote singularity function.

Two integrations give the internal moment as:

$$M(x) = \frac{P+10\gamma}{2} x^1 - P \langle x-5 \rangle^1 - \gamma \frac{x^2}{2} \quad (3.16)$$

The stress is expressed as:

$$\sigma_x = \frac{M(x) \cdot \bar{y}}{I_{zz}} \quad (3.17)$$

Where \bar{y} is the vertical distance from the neutral line.

Two more integrations give the vertical deflection as:

$$V = \left[\frac{P+10\gamma}{12} x^3 - \frac{P}{6} \langle x-5 \rangle^3 - \gamma \frac{x^4}{24} - \frac{75P+500\gamma}{12} x + \frac{125P}{6} \right] \cdot \frac{1}{EI_{zz}} \quad (3.18)$$

3.3.2 Analytic versus NMM solutions

In order to examine the influence of the mesh density on the results, four simulations with different mesh density ($e = 5, 10, 20$ and 40) are performed. The four NMM beams (at the end of the simulations) are presented in Figure 3.16. The bases beneath the beam are fixed, and eliminate the beam from downward displacement. The mechanical and numerical parameters in the simulations are presented in Table 3.3.

Table 3.3. Input parameters for MM analysis.

$K01$	$g2$	$g1$ [s]	$g0$ [kN/m]	e	E [GPa]	ν	γ [kN/m ³]
0	0.005	0.0005	5000000	5,10,20,40	1	0.2	25.48

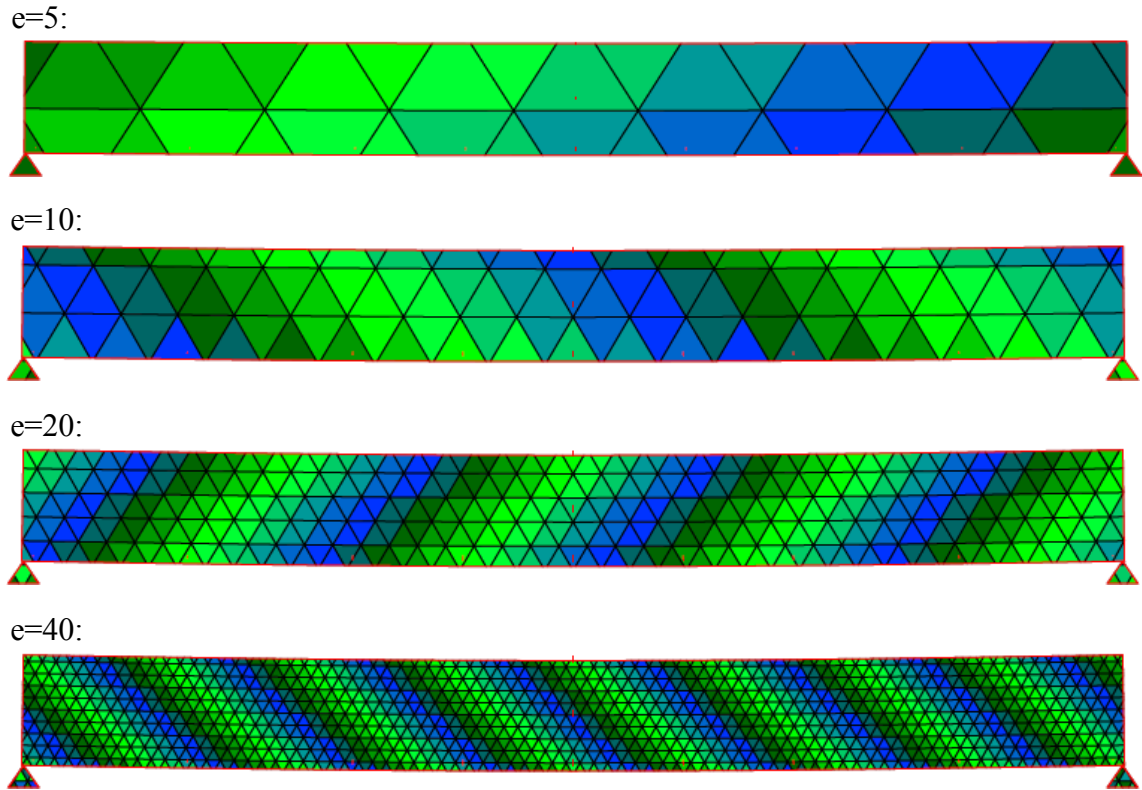


Figure 3.16. NMM models of the beams at the end of the simulation for mesh densities of 5, 10, 20 and 40.

The comparisons between analytically derived and numerically obtained horizontal stresses are shown in Figure 3.17. The relative errors at 7 measurement points for mesh densities of 10, 20 and 40 are plotted in Figure 3.18. At the ends of the beam, the stresses are very small, and therefore, the relative errors are much greater, and cannot be presented at the scale of the Figure. Generally, the accuracy increases with increasing mesh density from average relative error of 91% at mesh density of 5 (not plotted due to figure scale), to average relative error of 18% at mesh density of 10, to average relative error of 9% at mesh density of 40. At mesh density of 20, however, the results at the three central measurement points are less accurate than the results in mesh density of 10, but at other 4 points, the results are even more accurate than the results at mesh density of 40.

The comparisons between analytically derived and numerically obtained vertical deflection are shown in Figure 3.19. The relative errors for mesh densities of 10, 20 and 40 are plotted in Figure 3.20. The accuracy increases with increasing mesh density from average relative error of 62% at mesh density of 5 (not plotted due to figure scale), to average relative error of 29% at mesh density of 10, to average relative error of 7.7% at mesh density of 20 and to average relative error of 0.7% at mesh density of 40.

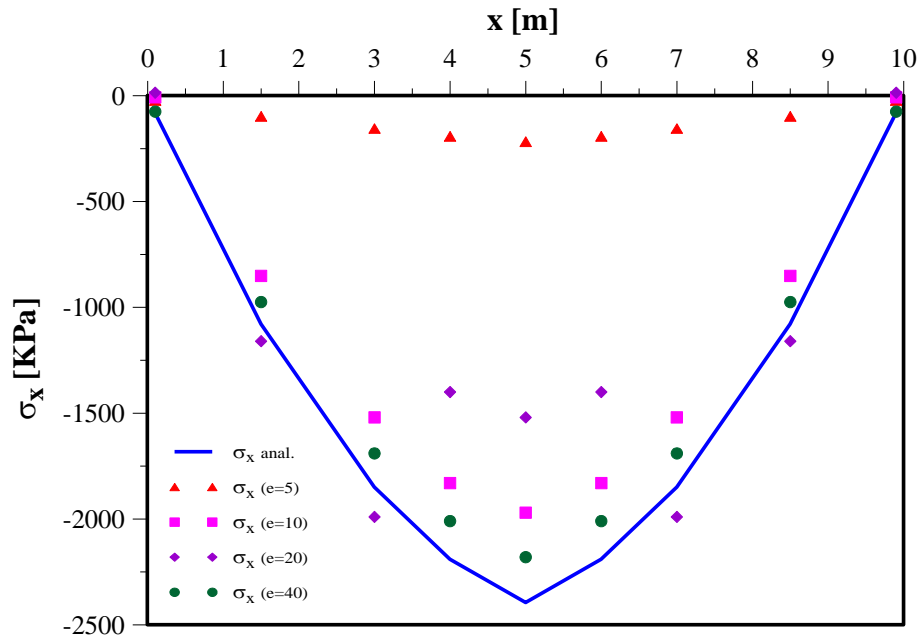


Figure 3.17. Comparison between results of analytical (dashed blue line) and NMM: Horizontal stresses as a function of x for mesh densities of 5, 10, 20 and 40.

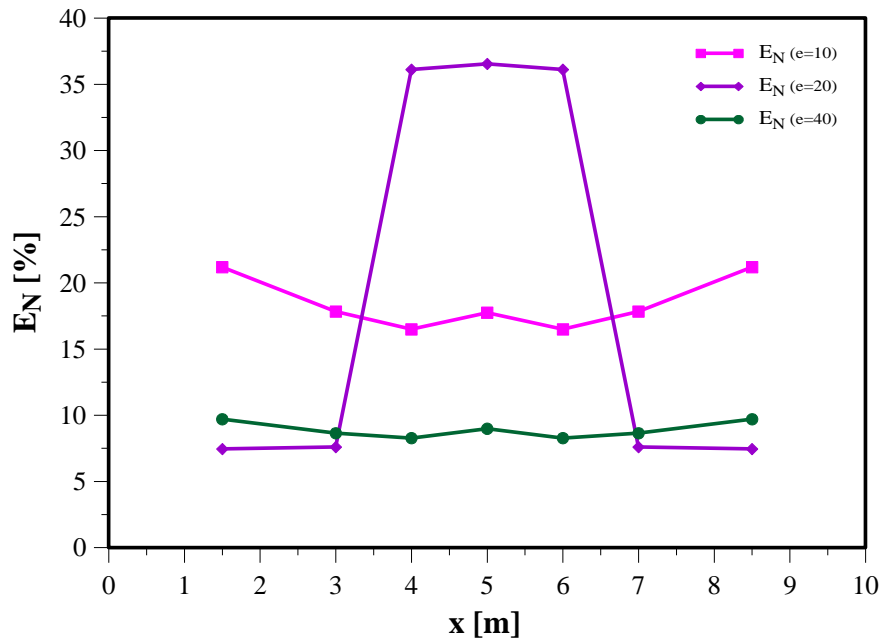


Figure 3.18. Relative errors of the horizontal stresses as a function of X for densities of 10, 20 and 40 at 7 measurement points (two points at the ends are absent due to figure scale).

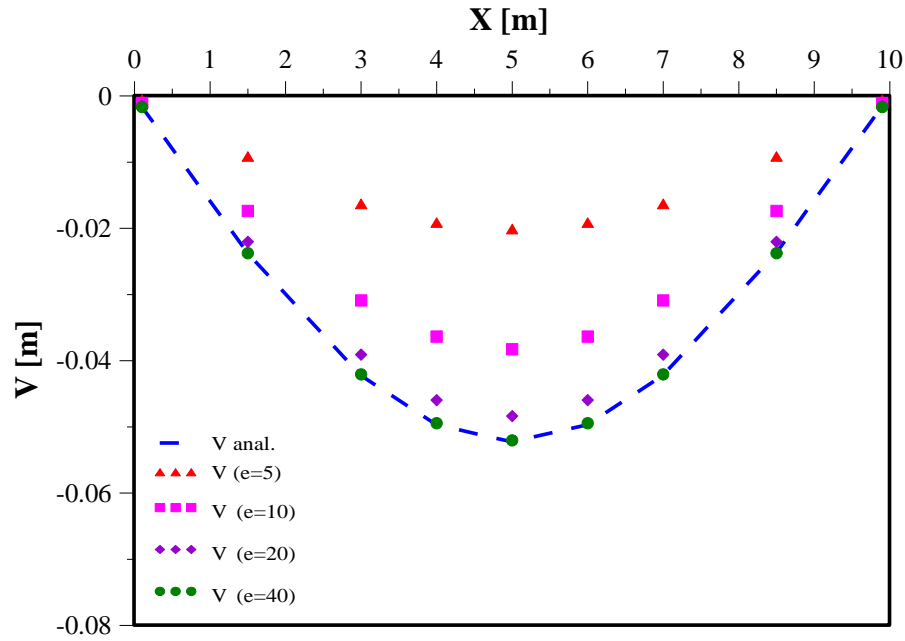


Figure 3.19. Comparison between results of analytical (dashed blue line) and NMM: Vertical displacements as a function of X for mesh densities of 5, 10, 20 and 40.

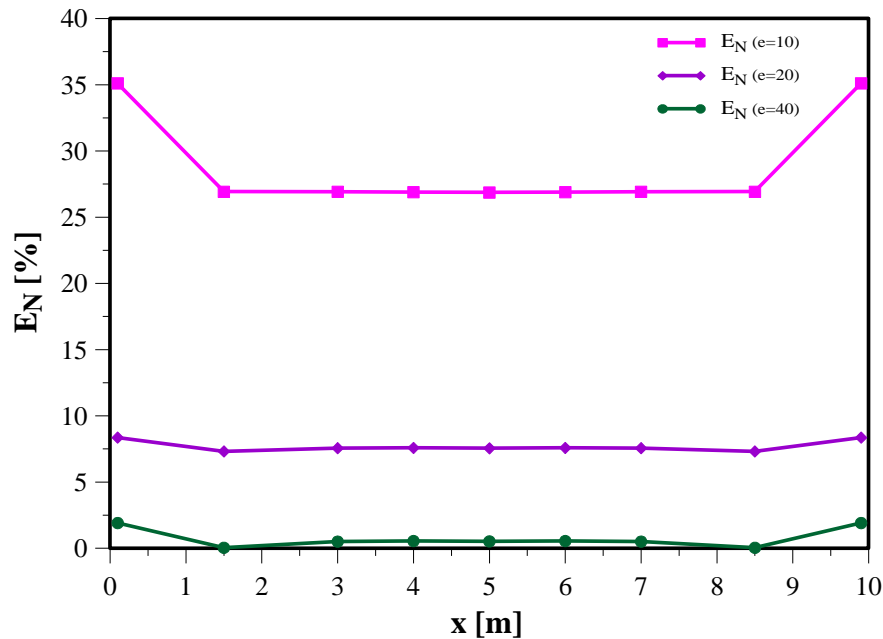


Figure 3.20. Relative errors of the vertical displacements as a function of X for mesh densities of 10, 20 and 40.

3.4 Dynamic sliding of a block on an incline

In order to verify the NMM for dynamic deformation, the case of a block on an inclined plane under gravity is re-examined following previous DDA works. The case of dynamic sliding of block on an incline was verified with DDA by Kamai and Hatzor (2008). In contrast to DDA, where during sliding in this special case the contacts between blocks remain unchanged because they are located only at the vertices of the blocks, in the NMM

contacts are updated during sliding because they are located also at intersections between the mathematical mesh and the boundaries (see 2.1.3). The dynamic verification is performed here also for calibration purposes. The influence of the numerical parameters g_1 , g_2 and g_0 on the NMM accuracy is examined.

3.4.1 Analytical solution

For a single block resting on a plane inclined at an angle α with friction along the interface $\tan\phi$, and subjected to gravitational acceleration g (Figure 3.21), the displacement time history $d(t)$ can be derived based on Newton's second law as:

$$d(t) = \frac{1}{2}at^2 = \frac{1}{2}(g \sin \alpha - g \cos \alpha \tan \phi)t^2 \quad (3.19)$$

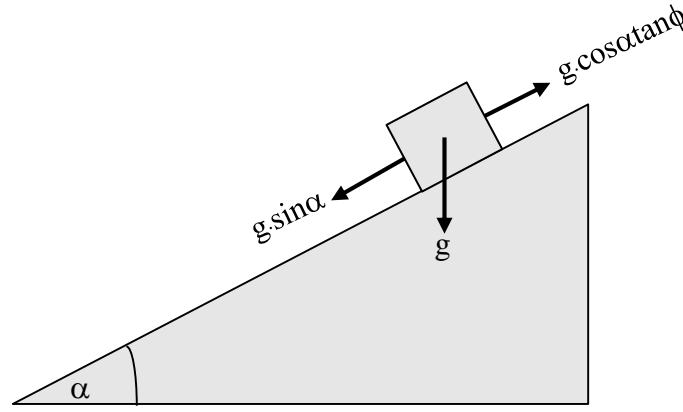


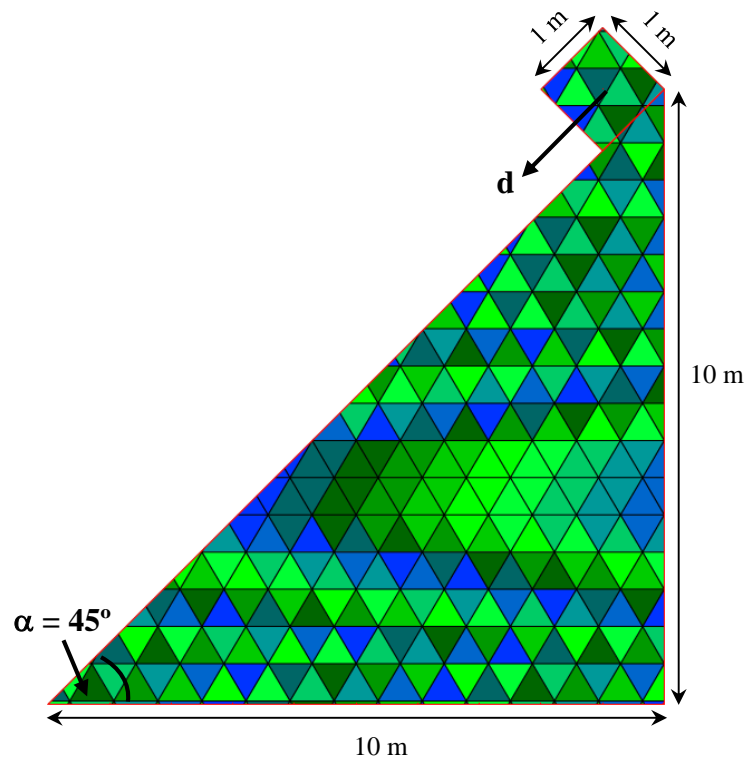
Figure 3.21. Schematic presentation of the forces acting on a single block lying on an incline.

3.4.2 Analytical versus NMM solutions

The layout of the numerical model is shown in Figure 3.22 . In order to examine the influence of the time step size (g_1), spring's stiffness (g_0) and assumed maximum displacement ratio (g_2) on the results, 343 simulations with different combinations of those three numerical control parameters (Table 3.4) are performed automatically by a self-developed C code program (each numerical control parameter had seven values). However, the model dimension, mechanical parameters and the mesh density remained constant in all simulations. The number of time steps was updated according to the time step size in order to ensure a total time of 1 s in all simulations.

Table 3.4. Input parameters for NMM analysis.

$K01$	E	E [GPa]	ν	γ [kN/m ³]	ϕ	$g2$	$g1$ [s]	$g0/E$
1	10	10	0.25	19.6	30°	0.0001	0.0001	0.1
						0.00025	0.00025	0.25
						0.0005	0.0005	0.5
						0.001	0.001	1
						0.0025	0.0025	2.5
						0.005	0.005	5
						0.01	0.01	10

**Figure 3.22. NMM model of a block on an incline**

A comparison between analytically derived and numerically obtained displacements for the case of $g1 = 0.00025$ s, $g2 = 0.001$, and $g0/E = 5$ is shown in Figure 3.23. A very good agreement is obtained, with relative errors decreasing from 1.77% at $t = 0.1$ s to 0.22% at $t = 1$ s (Figure 3.24).

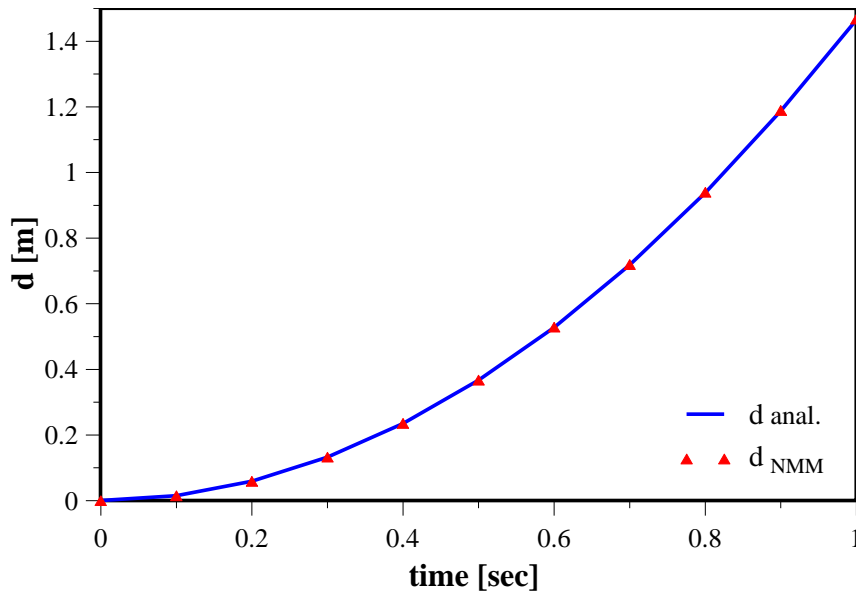


Figure 3.23. Comparison between results of analytical (blue line) and NMM: Block displacement as a function of time for the case of $g_1 = 0.00025$, $g_2 = 0.001$, and $g_0 = 5E$.

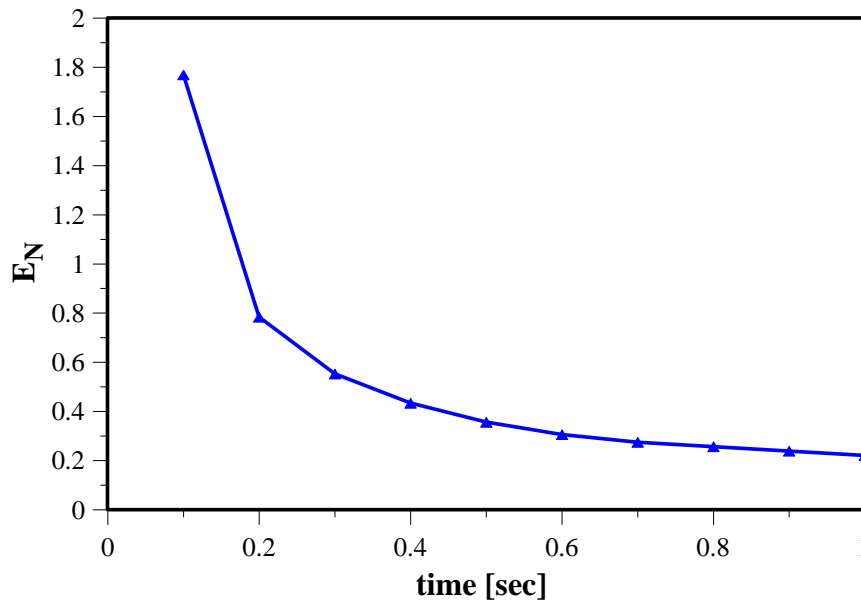


Figure 3.24. Relative errors of the displacements as a function of time for the case of $g_1 = 0.00025$ s, $g_2 = 0.001$, and $g_0/E = 5$.

A summary of the relative errors at the ends of all 343 simulations is presented in Figure 3.25. Generally, a good agreement is obtained where the relative errors are less than 0.5 % in 62 % of the combinations, less than 1.5 % in 83 % of the combinations, less than 5 % in 90 % of the combinations, and never exceed 10 %. Examination of the numerical parameters influence on the results accuracy shows that:

- 1) For the time step size (g_1), it has no significant influence on the results accuracy, except for time step size of $g_1 = 0.01$ s where most of the numerical errors are greater than 5 %. An optimum of the results accuracy is obtained at $g_1 = 0.0005$ s.

- 2) For the spring's stiffness (g_0), there is an influence only at the smallest time step size ($g_1 = 0.0001$) where the relative errors increase with increasing stiffness. However, even at this time step size the relative errors are greater than 3 % only in 5 out of 49 simulations.
- 3) For the assumed maximum displacement ratio (g_2), it has no influence on the results accuracy.

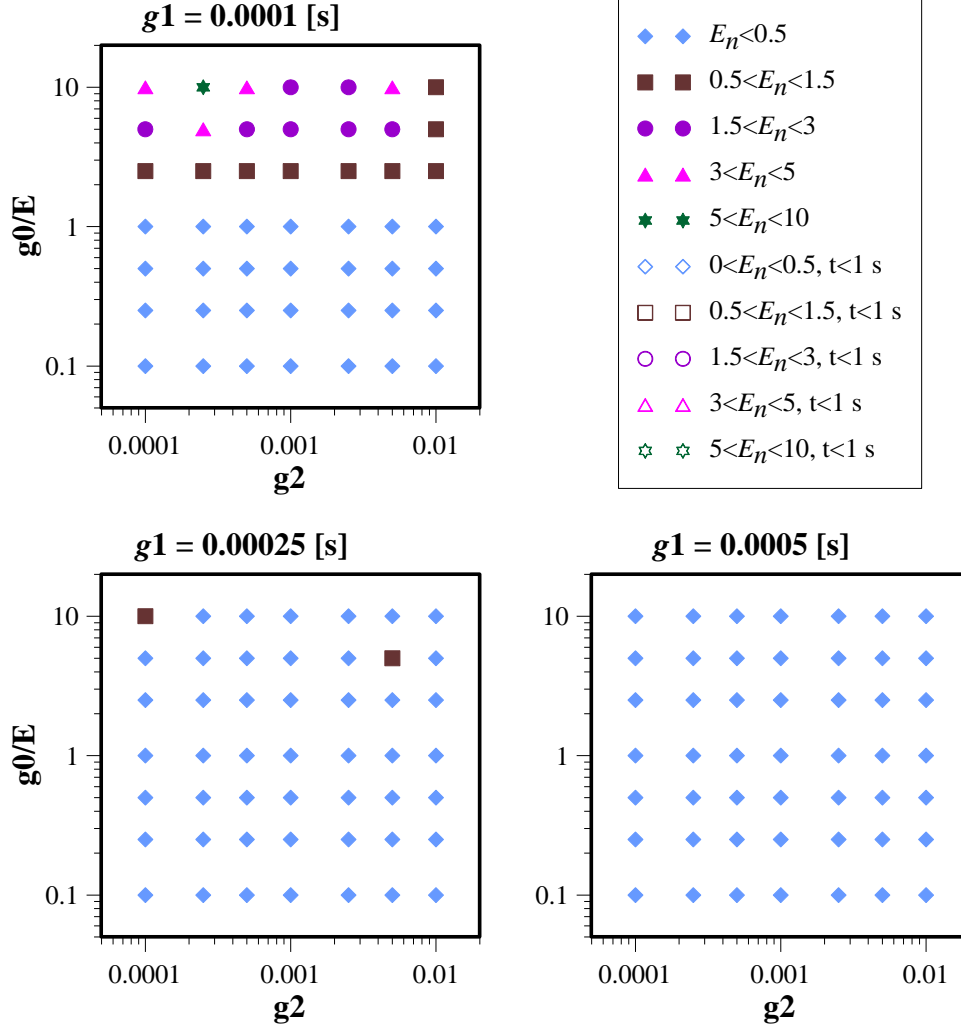


Figure 3.25. Relative errors of the vertical displacement at $t = 1$ s as a function of g_1 , g_0 , g_2 . The empty symbols represent simulations where the total time of the simulation is lower than 1 s.

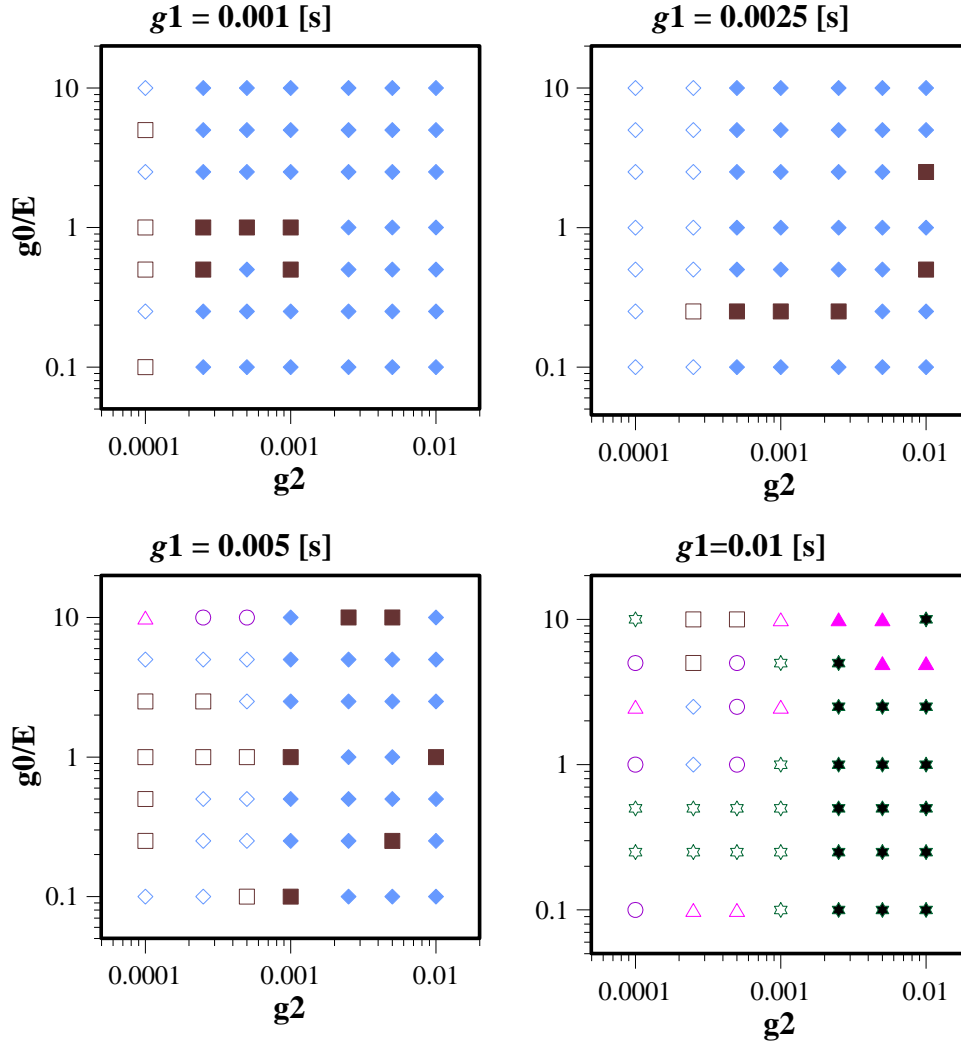


Figure 3.25 (cont.). Relative errors of the vertical displacement at $t = 1$ s as a function of g_1 , g_0 , g_2 . The empty symbols represent simulations where the total time of the simulation is lower than 1 s.

3.4.3 Average number of iterations per time step and total time of simulation

Figure 3.26 shows the average number of open-close iterations per time step (i_{av}) as a function of g_2/g_1 ratio in all 49 combinations of g_2 and g_1 . Since seven simulations are performed for each combination of g_2 and g_1 (seven different values g_0), the average value of i_{av} in all seven simulations is taken. When g_2/g_1 ratio is larger than 0.1, i_{av} remains stable with values never exceeding 1.1. When g_2/g_1 ratio is 0.1 and below however, i_{av} increases with decreasing g_2/g_1 ratio to value of 2.77 at g_2/g_1 ratio of 0.01.

Figure 3.27 shows the total time of simulation as a function of g_2/g_1 ratio in all 49 combinations of g_2 and g_1 . When g_2/g_1 ratio is 0.1 and less, the total time of the simulations is lower than planned (1 s), and decreases with decreasing g_2/g_1 ratio to minimum value of 0.35 s at g_2/g_1 ratio of 0.01. A lower total time of simulation than planned is a result of reduction of the real time step size ($\Delta(t)$) during the simulation due to two possible options

(section 2.6c)): 1) the condition of no penetration/no tension in all contacts is not fulfilled after six open-close iterations; and 2) the condition that the displacements of all points in the problem domain during the current step are less than a pre-defined limit ρ ($\rho = g2*H$) is not fulfilled (H is half the height of the analysis domain size). In the case of dynamic sliding, the second condition is relevant because reduction of $\Delta(t)$ is observed in i_{av} values of 1.25 – 2.77 (significantly smaller than 6). Moreover, most of the additional iterations are due to nonfulfillment of the second condition rather than the no penetration/no tension condition.

The evolution of $\Delta(t)$ during the simulation is plotted in Figure 3.28. In the beginning of the simulation, the block velocity and displacement are small, and $\Delta(t)$ remains stable. After 32 time steps the displacements are higher than the pre-defined limit ρ (in the problem of a block on an incline the velocity and displacement increase with time), and $\Delta(t)$ decreases sharply to 0.0035 s. Then, $\Delta(t)$ decreases continuously to a value of 0.25 s after 85 time steps. Another sharp reduction of $\Delta(t)$ occurs after 86 time steps. At this stage, there are two reductions of $\Delta(t)$ in each step because of the large displacements. At the end of the simulation $\Delta(t) = 0.0013$ s, only 25 % the planned value.

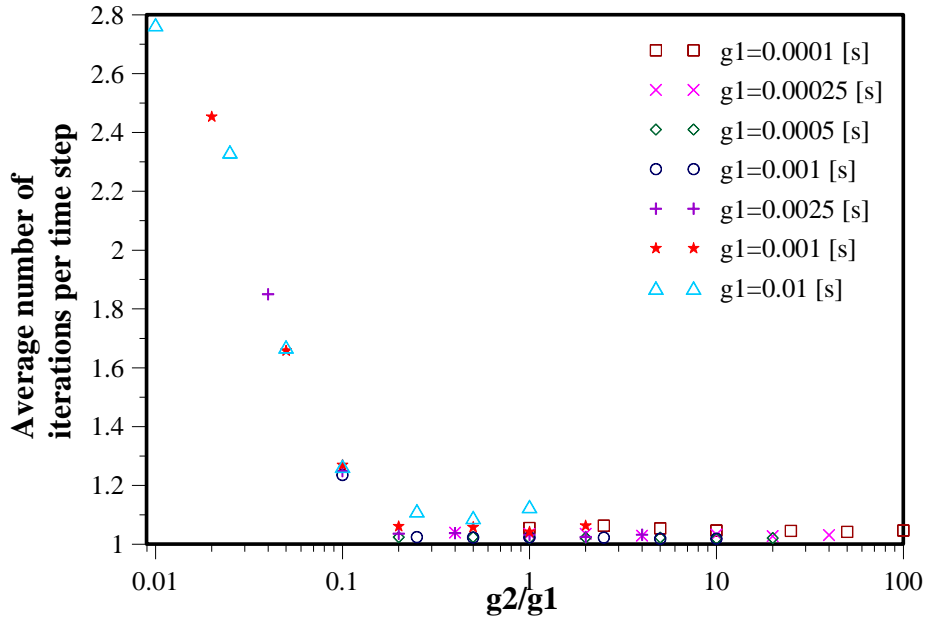


Figure 3.26. average number of open-close iterations per time step as a function of $g1/g2$ ratio in all 49 combinations of $g2$ and $g1$.

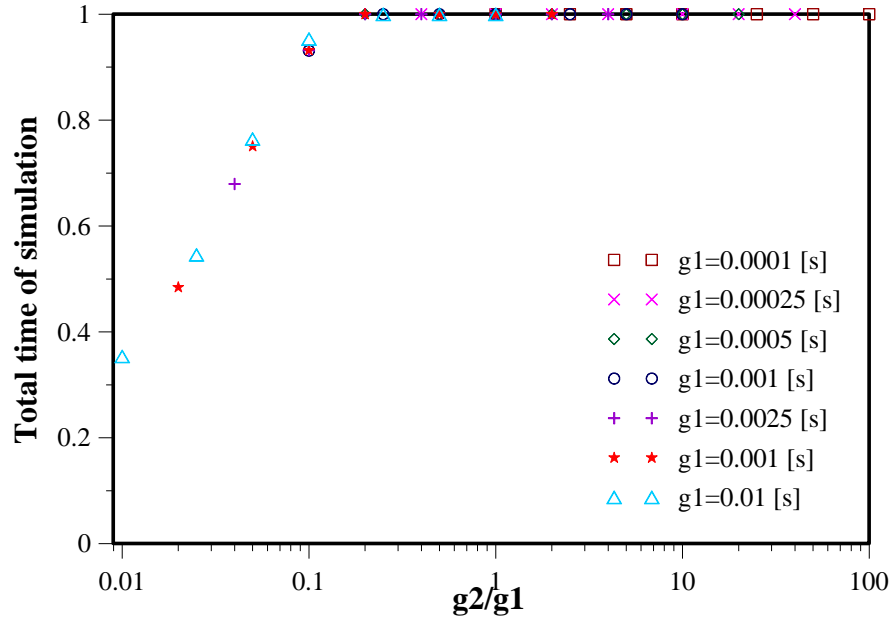


Figure 3.27. Total time of simulation as a function of g_1/g_2 ratio in all 49 combinations of g_2 and g_1 .

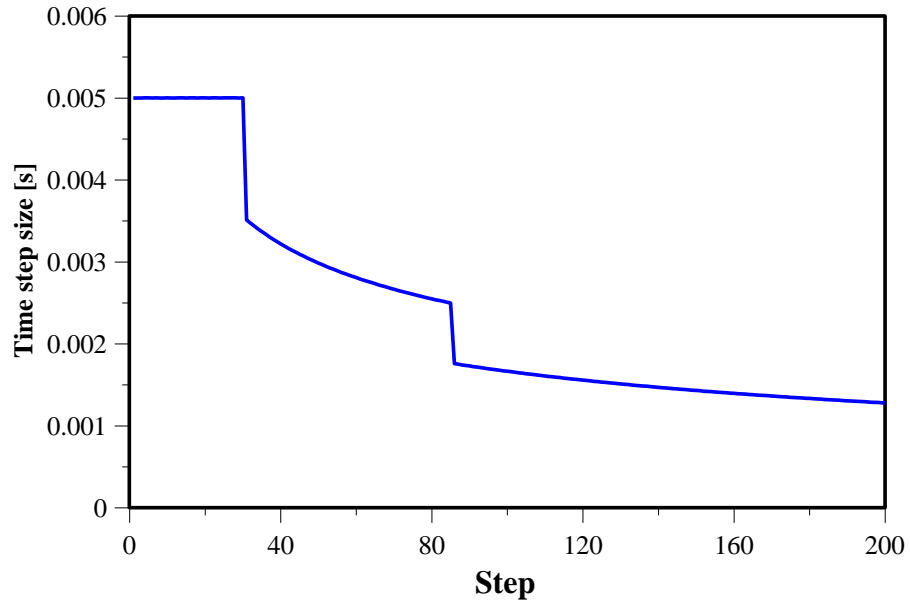


Figure 3.28. Evolution of time step size during the simulation for the case of $g_1 = 0.005$ s, $g_2 = 0.0001$ and $g_0/E = 1$.

3.5 Summary and conclusions

The accuracy of the NMM program is verified using three static problems (layered plate under gravity, Kirsch solution and beam under concentrate load and volumetric force), and one dynamic problem (block on an incline). A good agreement is obtained between the numerical and the analytical solutions.

In the static problems, both stresses and displacements are examined. The NMM results for the displacements are always much more accurate than the NMM results for the stresses. This observation can be explained by the fact that the NMM aims for the

displacements. The displacements are solved first, then by interpolation and derivation of the displacements the strains are obtained, and by Hooke's law the stresses are obtained. For each element, a linear displacement function is defined, while the stresses are constant.

The influence of the mesh density on the NMM results is examined for the case of beam under concentrate load and volumetric force. The accuracy of the NMM results for the displacements increases with increasing mesh density as expected from method with linear displacement function. However, the accuracy of the NMM results for the stresses does not always increase with increasing mesh density. Since the stresses are constant in each element and are the average of the contributions from each node of the triangle, the accuracy of the numerical solution for the stresses depends on the relative location of the measurement point inside the element, i.e. the accuracy increases when the measurement points are located at the center of the element. The relative location of the measurement points changes when the mesh changes. Consequently, the accuracy of the numerical solution for the stresses does not always increase with increasing mesh density. For example, in the case of a beam with mesh density of $e=20$, the three central measurement points are located near the lower node of the element (Figure 3.29) while the center of the element is slightly higher. Therefore, the numerical solution for the stresses is lower than the analytical solution, and is not accurate. This issue should be kept in the mind by any NMM user when placing measurement points for stress analysis.

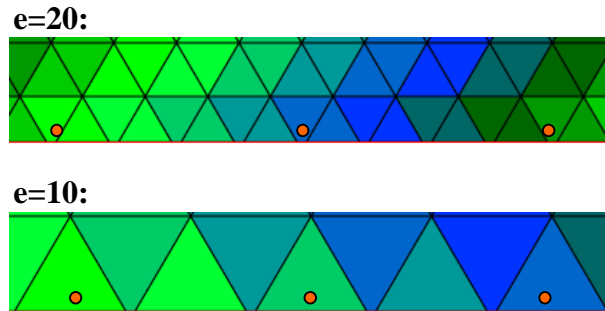


Figure 3.29. Relative location of the three central measurement points (orange dots) inside the elements for mesh densities of $e=10$ and $e=20$.

The influence of the numerical control parameters g_0 , g_1 and g_2 on the NMM results is examined only for the dynamic verification of block on an incline where the solution is determined by the displacement along block boundaries. Accurate results are obtained for time step sizes smaller than $g_1 = 0.01$ s. The total time of the simulation however is lower than planned in simulations where the ratio g_2/g_1 is 0.1 and below, as a result of automatic time step size reduction performed by the code during the simulation. The time step size is

reduced in order to fulfill the condition that displacements of all points in the problem domain during the current step are less than a pre-defined limit ρ ($\rho = g2^*H$).

Chapter 4- Simulating the excavation sequence

In the original NMM code developed by Shi (1996a), tunnels exist from the beginning of the simulation. However, in reality when tunnels are excavated, compressive stresses already exist in the field, and the rock column has already experienced an elastic deformation over geologic times due to overburden stress. This issue can be very important when the stability of underground opening in discontinuous rock mass is analyzed.

In this thesis, the original NMM code is modified for tunnel excavation during the NMM simulation, after the local stresses already exist and the elastic deformation has already occurred. The modified NMM code contains two stages: 1) at the beginning of the simulation a single block replaces the tunnel and static simulation ($KOI = 0$) is executed until equilibrium is attained. Then, 2) the tunnel block is removed (simulating tunnel excavation), and a dynamic computation ($KOI = 1$) is executed. The block removal process includes the removal of manifold elements inside this block and their corresponding star nodes, and the detachment of contacts with neighboring blocks. Because manifold elements are the intersection between the physical domain and the mathematical cover, the removal of an existing block enables realistic modeling of the excavation sequence without splitting existing manifold elements.

In order to examine the significance of opening the underground openings during the simulation rather than from the beginning of the simulation, the stability of rectangular underground openings excavated in horizontally stratified and vertically jointed rock masses is examined.

4.1 Model geometry and mechanical properties

The layout of the numerical model is presented in Figure 4.1. The analysis domain is 30 m high and 30 m wide, and is constrained between stiff boundaries at sides and bottom. The opening geometry is of a rectangular shaped tunnel with span $B = 12$ m and height $h_t = 6$ m located at a depth of 17 m (center). Two joint sets are generated: a set of horizontal bedding planes and a set of vertical joints, each with average spacing of $S_j = 2$ m. The displacements and stresses within the rock mass are measured at eight measurement points along a vertical line rising from the excavation crown. The mechanical properties of the rock mass are: $E = 10$ [GPa], $\nu = 0.2$, and $\gamma = 24.5$ [kN/m³]. The simulations are performed under plane strain conditions.

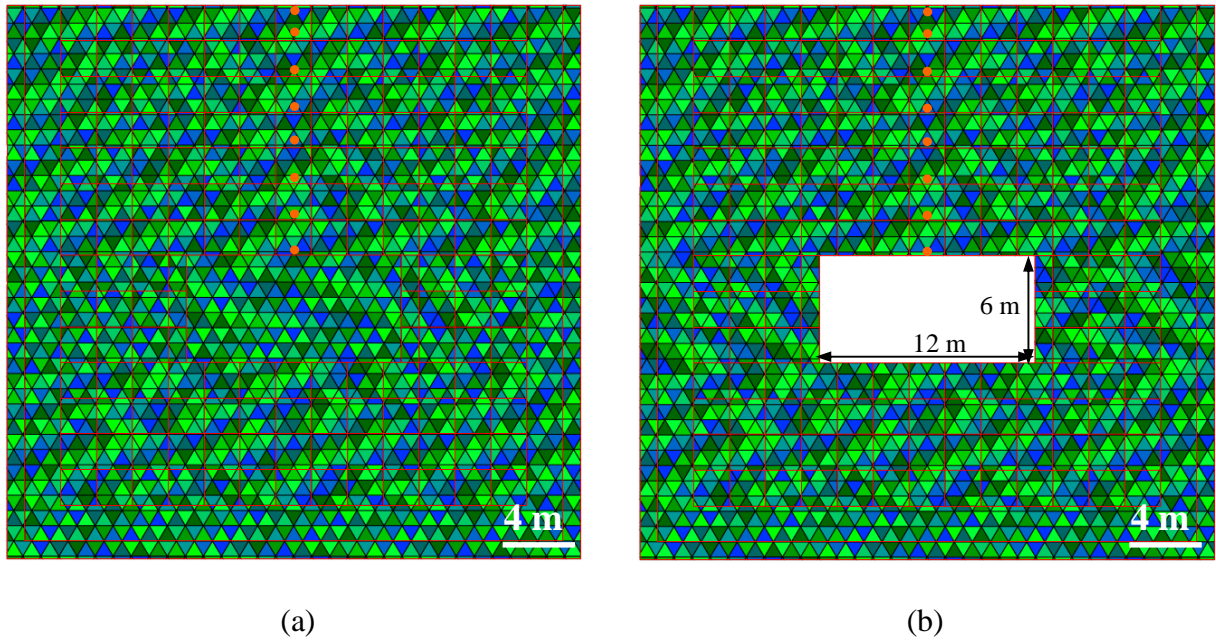


Figure 4.1. NMM model of the analyzed opening: a) modified NMM model at the beginning of the simulation; and b) original NMM model at the beginning of the simulation.

4.2 Numerical control parameters calibration

For a blocky rock mass under dynamic simulation, a proper selection of numerical control parameters is essential. The density of the mesh ($e = 20$) is chosen to be sufficiently dense so that each layer of the rock mass contains approximately two layers of elements, to enable more degrees of freedom for every block in the system without increasing the simulation time. Moreover, here the numerical parameters that control the relationship between the blocks are more important than the mesh density that affects the solution with respect to the continuous medium inside the blocks. The size of the time step is set to $g1 = 0.00025$ in order to allow small displacements in a single time step, but to avoid exceedingly long simulations. In order to select proper spring's stiffness ($g0$) and assumed maximum displacement ratio ($g2$), 15 simulations are performed, each simulation with different combination of spring's stiffness and assumed maximum displacement ratio (Table 4.1). In all 15 simulations, the first static stage is 5 s long (20,000 steps), and the second dynamic stage is 7.5 s long (30,000 steps). The importance of choosing the right numerical control parameter can be demonstrated by the different evolutions of the underground openings during the simulations (Table 4.2), which change from stable, to significant roof displacement, to unstable, and in one case to severe penetration between blocks.

Table 4.1. Input Numerical parameters for NMM analysis.

$K01$	$g2$	$g1$ [s]	$g0/E$	e
1	0.0001 0.00025 0.0005	0.00025	0.1 0.5 1 5 10	20

Table 4.2. Underground opening at the end of the simulations.

		$g2$		
		0.0001	0.00025	0.0005
$g0/E$	0.1	penetration	stable	unstable
	0.5	unstable	stable	stable
	1	stable	stable	significant roof displacement
	5	stable	stable	significant roof displacement
	10	stable	stable	significant roof displacement

In the following three sections, the spring's stiffness and the assumed maximum displacement ratio are examined on the basis of three criteria: 1) accuracy of the numeric results at the end of the first stage (before the excavation) of the simulation; 2) average number of open-close iterations per time step; and 3) computing time (CPU time).

4.2.1 Accuracy of the numerical results at the end of the first static stage

In this section, a comparison between analytically derived and numerically obtained stresses and displacements, at the end of the first static stage of the simulation, is performed. At the end of the first stage the tunnel is not excavated yet, the rock mass is subjected to compressive stresses only, and blocks are constrained kinematically. Thus, the blocky rock mass behavior is quasi continuous, and the numerical results can be compared to the analytical results developed for a continuous medium in section 3.1.1.

The comparisons between analytically derived and numerically obtained horizontal stresses, vertical stresses and vertical displacements for assumed maximum displacement ratio of $g2=0.0001$ are shown in Figure 4.2, Figure 4.3 and Figure 4.4 respectively. The spring's stiffness ranges from one order below the young's modulus to one order above it ($g0/E = 0.1, 0.5, 1, 5$ and 10). Generally, a trend of increasing accuracy of the numerical results with increasing spring stiffness is seen. A decrease of the springs stiffness causes an under estimate of the stresses predicted by NMM compared to the analytical results, and an over estimate of the vertical displacements predicted by NMM compared to the analytical results.

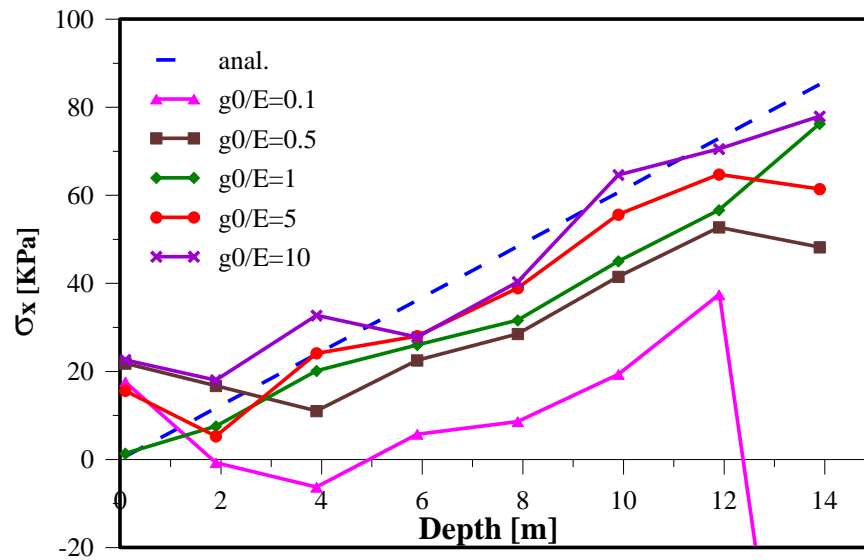


Figure 4.2. Comparison between results of analytical (dashed blue line) and NMM solutions: horizontal stresses as a function of measurement point depth for assumed maximum displacement ratio of $g_2 = 0.0001$, and g_0/E ratios of 0.1, 0.5, 1, 5 and 10.

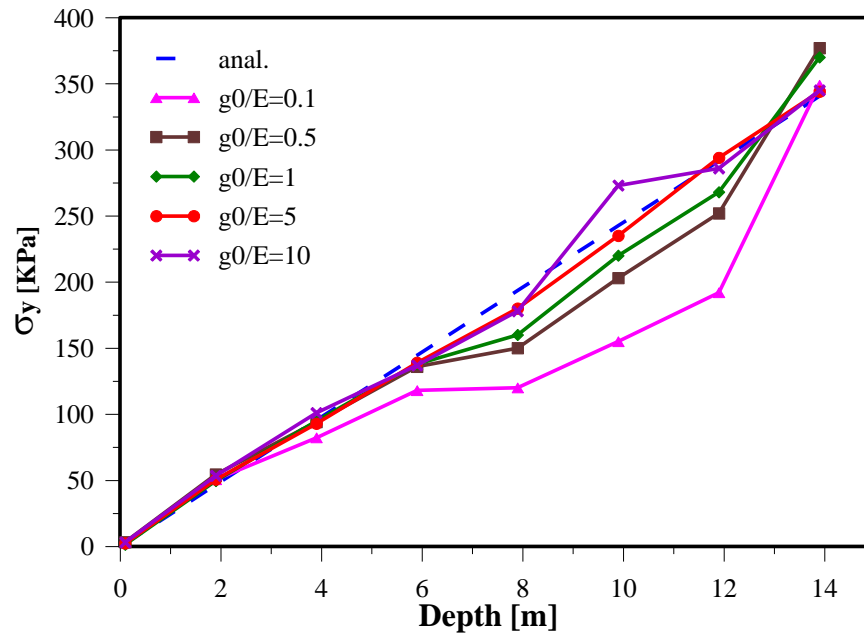


Figure 4.3. Comparison between results of analytical (dashed blue line) and NMM solutions: vertical stresses as a function of measurement point depth for assumed maximum displacement ratio of $g_2 = 0.0001$, and g_0/E ratios of 0.1, 0.5, 1, 5 and 10.

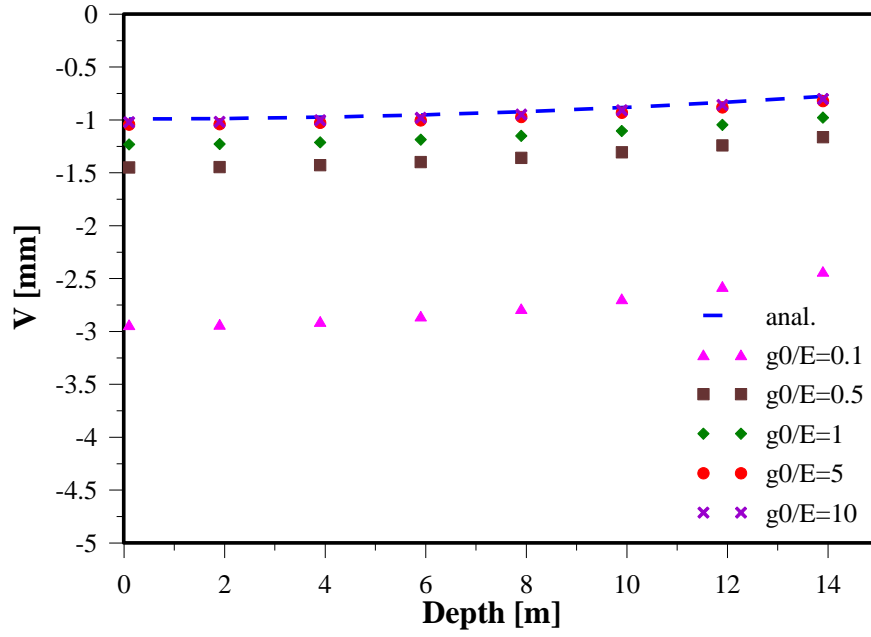


Figure 4.4. Comparison between results of analytical (dashed blue line) and NMM solutions: vertical displacements as a function of measurement point depth for assumed maximum displacement ratio of $g_2 = 0.0001$, and g_0/E ratios of 0.1, 0.5, 1, 5 and 10.

In order compare all 15 simulations in more convenient method while taking into consideration the effect of all eight measurement points, the root mean square (d_{RMS}) of the stresses and displacements in each simulation is calculated. The d_{RMS} gives the same weight for each measurement point since it does not include relative values, and is defined as

$$d_{RMS} = \sqrt{\frac{(d_1 - d_{N1})^2 + (d_2 - d_{N2})^2 + \dots + (d_n - d_{Nn})^2}{n}} \quad (4.1)$$

where d_i and d_{Ni} are analytical and numerical solutions of the i -th measurement point respectively, and n is the amount of measurement points.

The d_{RMS} of the horizontal stresses, vertical stresses and vertical displacements in all 15 simulations is presented in Figure 4.5, Figure 4.6 and Figure 4.7 respectively. Generally, d_{RMS} magnitude and rate decrease with increasing g_0/E ratio. The minimum d_{RMS} of the vertical displacements is obtained at g_0/E ratio of 10, and there is no significant difference between the results of the three maximum displacements ratios. However, for the horizontal and vertical stresses, the results are more complicated, and the minimum d_{RMS} is also depends on the maximum displacements ratio. The minimum d_{RMS} of the vertical stresses for $g_2 = 0.0001$ and $g_2 = 0.00025$ is obtained at g_0/E ratio of 5, while minimum d_{RMS} for $g_2 = 0.0005$ is higher, and is obtained in two g_0/E ratios: 5 and 10. The minimum d_{RMS} of the horizontal stresses for $g_2 = 0.00025$ is obtained at g_0/E ratio of 5, while minimum d_{RMS} for $g_2 = 0.0001$ and $g_2 = 0.0005$ is higher, and is obtained at g_0/E ratio of 10.

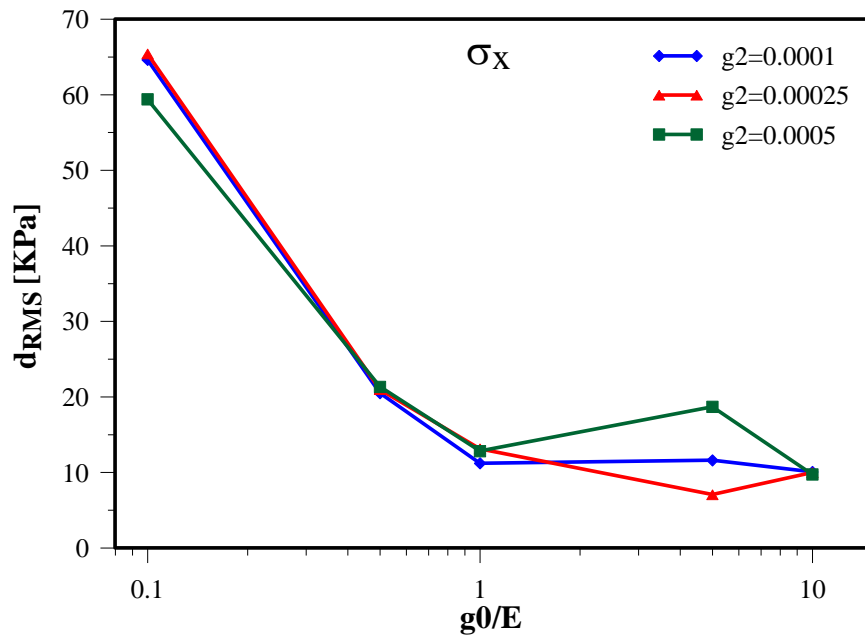


Figure 4.5. Root mean square of the horizontal stresses as a function of the ratio g_0/E for maximum displacement ratios of $g_2=0.0001$, $g_2=0.00025$, and $g_2=0.0005$.

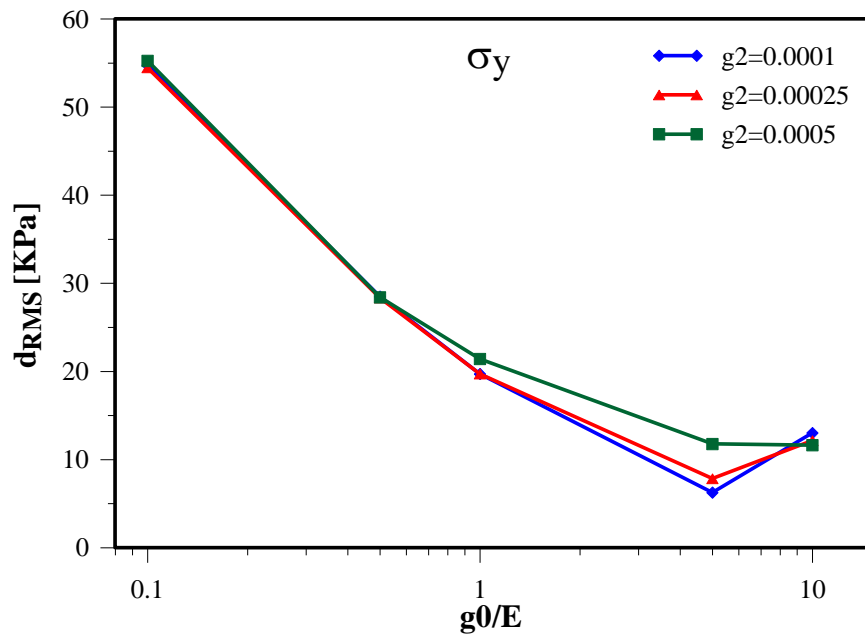


Figure 4.6. Root mean square of the vertical stresses as a function of the ratio g_0/E for maximum displacement ratios of $g_2=0.0001$, $g_2=0.00025$, and $g_2=0.0005$.

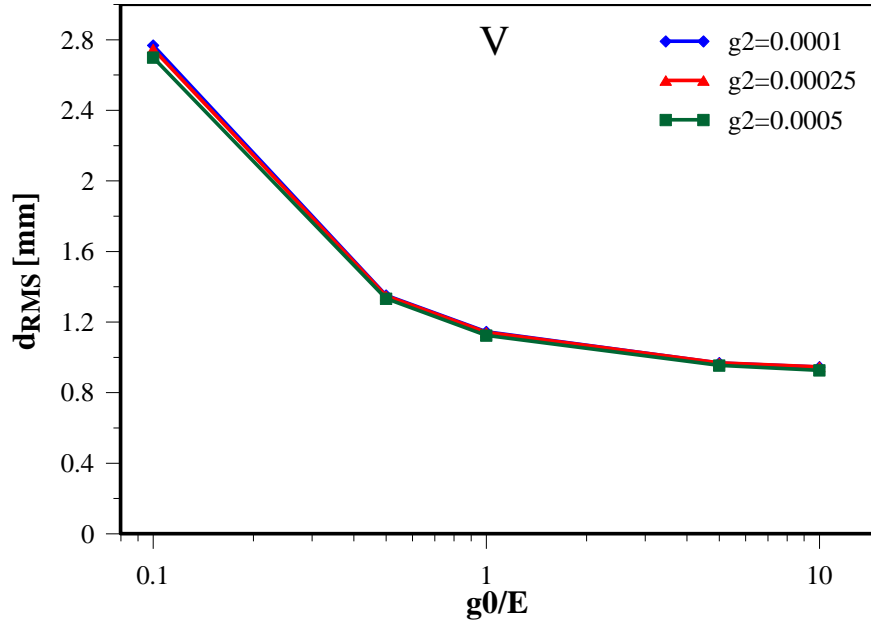


Figure 4.7. Root mean square of the vertical displacements as a function of the ratio g_0/E for maximum displacement ratios of $g_2=0.0001$, $g_2=0.00025$, and $g_2=0.0005$.

4.2.2 Average number of open-close iterations per time step

As mentioned in section 2.6, in order to satisfy the constraint of no penetration/no tension in all contacts, a method of open-close iterations is performed until a convergence of the solution is achieved. Thus, lower number of open close iterations leads to faster convergence of the solution. In addition, if open-close iterations cannot converge in 6 iterations the time step is reduced, and consequently the total time of the simulation might be significantly smaller than planned.

Figure 4.8 shows the average number of open-close iterations per time step (i_{av}) in all 15 simulations. The average number of open-close iterations increases with increasing maximum displacement ratio. For maximum displacement ratio of $g_2 = 0.0001$, i_{av} decreases with increasing springs stiffness, from 4 iteration per step at g_0/E ratio of 0.1 to 2.2 at g_0/E ratio of 5 and 10. On the contrary, for $g_2 = 0.00025$, i_{av} increases with increasing springs stiffness, from 3.4 at g_0/E ratio of 0.1 to 5.2 at g_0/E ratio of 1, where it stabilizes. For $g_2 = 0.0005$, i_{av} also increases with increasing springs stiffness: from 4.2 at g_0/E ratio of 0.1 to 11 at g_0/E ratio of 10.

Figure 4.9 shows the total time of simulation normalized by the planned total time (12.5 s) in all 15 simulations. The total time of the simulations is a mirror image of the i_{av} , i.e. in combination of g_0 and g_2 with high i_{av} , the normalized total time of simulation decreases significantly, where in the most extreme case the normalized total time decreases to 0.49. At combinations of g_0 and g_2 where i_{av} is lower than 4.5, the total time of the simulation is

approximately 12.5 s, except for the case of $g_2 = 0.0001$ and $g_0/E = 0.1$ where i_{av} is equal to 4, but the normalized total is 0.79 due to the penetration between the blocks.

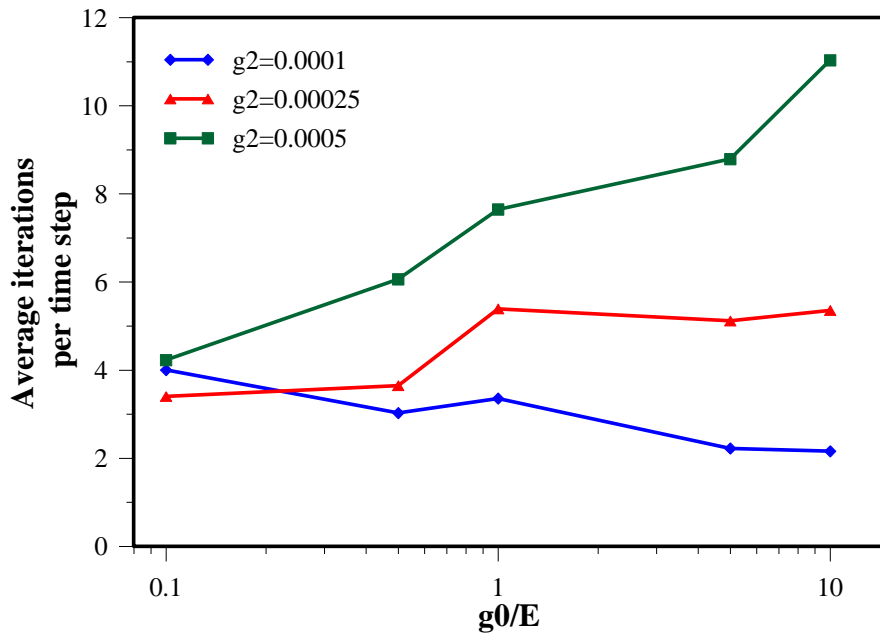


Figure 4.8. Average open-close iterations per time step as a function of g_0/E ratio for maximum displacement ratios of $g_2=0.0001$, $g_2=0.00025$, and $g_2=0.0005$.

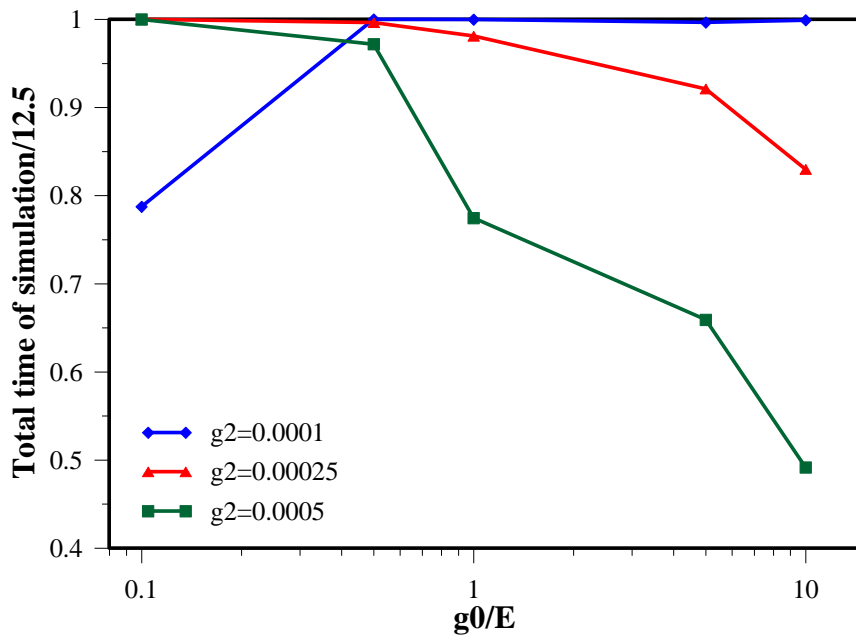


Figure 4.9. Total time of simulation normalized by the planned total time (12.5 s) as a function of g_0/E ratio for maximum displacement ratios of $g_2=0.0001$, $g_2=0.00025$, and $g_2=0.0005$.

4.2.3 Computing time (CPU time)

When analyzing a complex problem, computing time can be a critical issue. Figure 4.10 shows the CPU time in all 15 simulations. The CPU time increases with increasing maximum displacement ratio. For maximum displacement ratios of $g_2=0.0001$, the CPU time remains approximately 21 hours from g_0/E ratio of 0.1 to g_0/E ratio of 5, and then

increases to 29 hours at g_0/E ratio of 10. For $g_2=0.00025$, CPU time increases with increasing springs stiffness, from 25.6 hours at g_0/E ratio of 0.1 to 43.8 hours at g_0/E ratio of 10. For $g_2=0.0005$, the CPU time also increases with increasing springs stiffness, from 26 hours at g_0/E ratio of 0.1 to 84 hours at g_0/E ratio of 10.

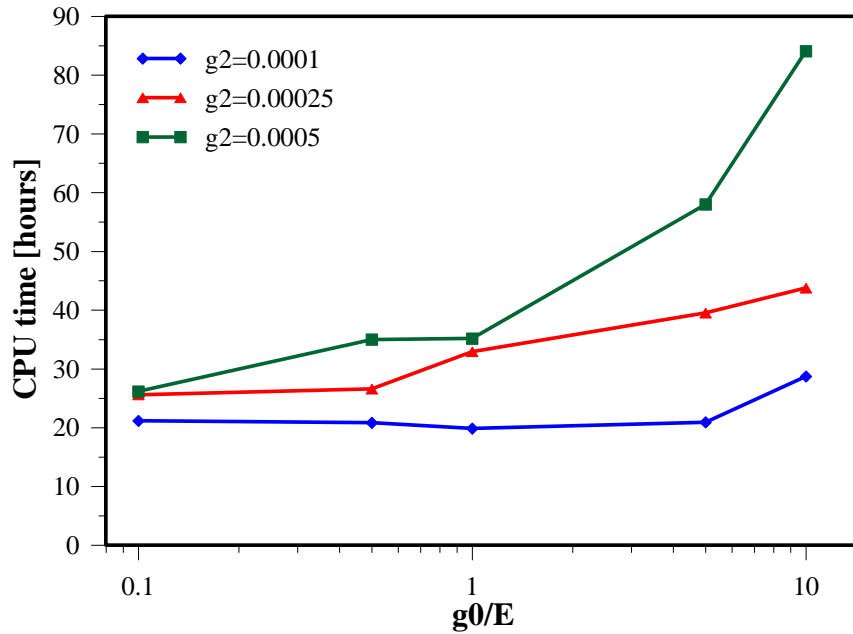


Figure 4.10. Simulation computing time as a function of g_0/E ratio for maximum displacement ratios of $g_2=0.0001$, $g_2=0.00025$, and $g_2=0.0005$.

4.2.4 Final selection of the numerical control parameters

Based on section 3.2.1, the most accurate results for the horizontal stresses, vertical stress and vertical displacements are obtained with spring's stiffness of $g_0 = 500000000 \text{ kN/m}$ and $g_0 = 1000000000 \text{ kN/m}$ ($g_0/E=5$ and 10). Based on section 4.2.2, the minimum average number of open-close iterations per time step is obtained at maximum displacement ratio of $g_2 = 0.0001$, and spring's stiffness of 500000000 kN/m and $g_0 = 1000000000 \text{ kN/m}$. Based on section 4.2.3, the minimum CPU time obtained at $g_0 =$ maximum displacement ratio of $g_2 = 0.0001$, and spring's stiffness of $g_0 = 10000000 \text{ kN/m}$, $g_0 = 500000000 \text{ kN/m}$, $g_0 = 100000000 \text{ kN/m}$ and $g_0 = 500000000 \text{ kN/m}$. Therefore, the maximum displacement ratio and contact stiffness which are chosen for the analysis are $g_2 = 0.0001$ and $g_0 = 500000000 \text{ kN/m}$ respectively.

4.3 Results

4.3.1 Original versus modified NMM

In order to compare the evolution of the analyzed opening under the modified NMM, where the underground opening is excavated during the simulation, and under the original NMM, where the underground opening is already excavated at the beginning of the simulation, seven simulations with friction angles of 10° , 15° , 20° , 25° , 30° , 35° and 40° are performed with each method. Figure 4.11 shows the underground openings at the end of the simulations. The modified NMM simulations are presented at the left hand side, and original NMM simulations are presented at the right hand side. For friction angle of $\phi = 10^\circ$, the opening is not stable in both method. For friction angles ranging from $\phi = 15^\circ$ to $\phi = 25^\circ$, the opening is not stable in the original NMM, but stable in the modified NMM. For friction angles ranging from $\phi = 30^\circ$ to $\phi = 40^\circ$, the opening is stable in both method. In two simulation, a severe deflection of the opening cover occurs (modified NMM $\phi = 25^\circ$, and original NMM $\phi = 30^\circ$). However, in both cases the displacements occur only at the beginning of the dynamic simulation (0.5-1 s), and then the opening is stable.

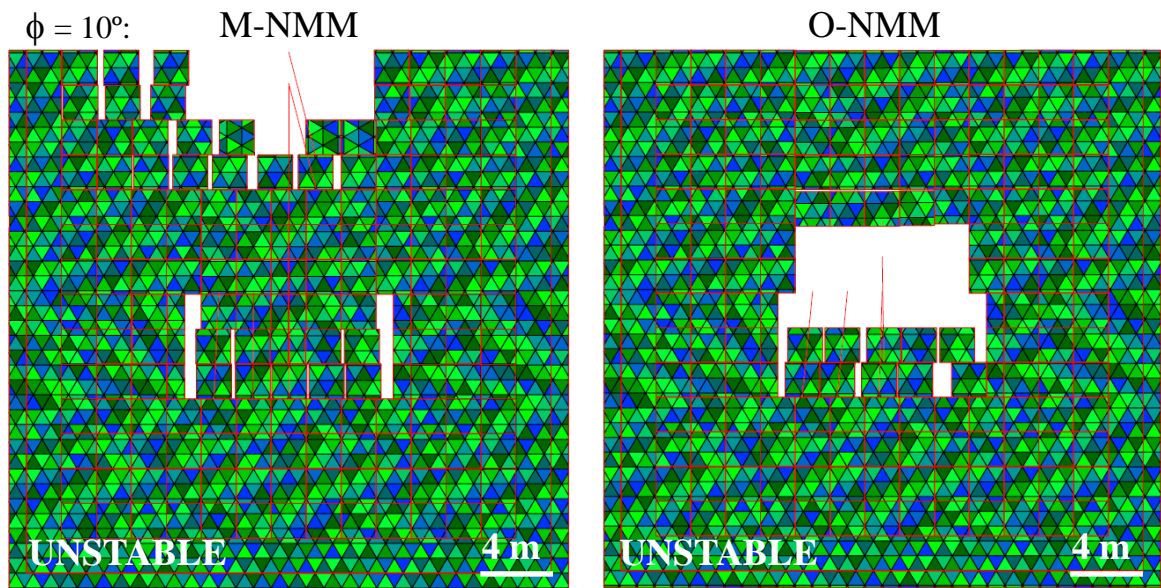


Figure 4.11. The analyzed opening at the end of the modified NMM simulations (left hand side), and at the end of the original NMM simulations (right hand side) for friction angles of 10° , 15° , 20° , 25° , 30° , 35° and 40° .

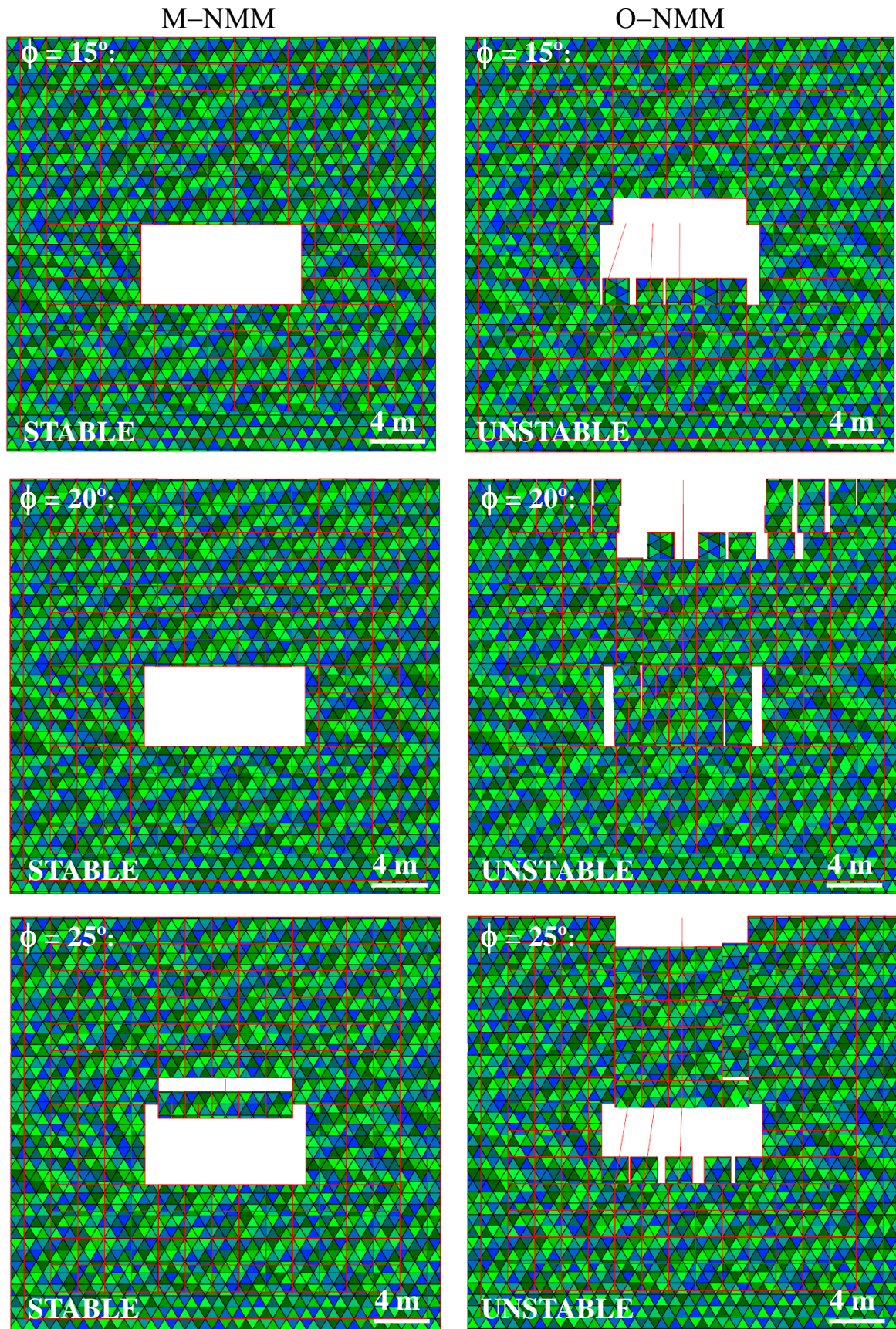


Figure 4.11 (cont.). The analyzed opening at the end of the modified NMM simulations (left hand side), and at the end of the original NMM simulations (right hand side) for friction angles of 10° , 15° , 20° , 25° , 30° , 35° and 40° .

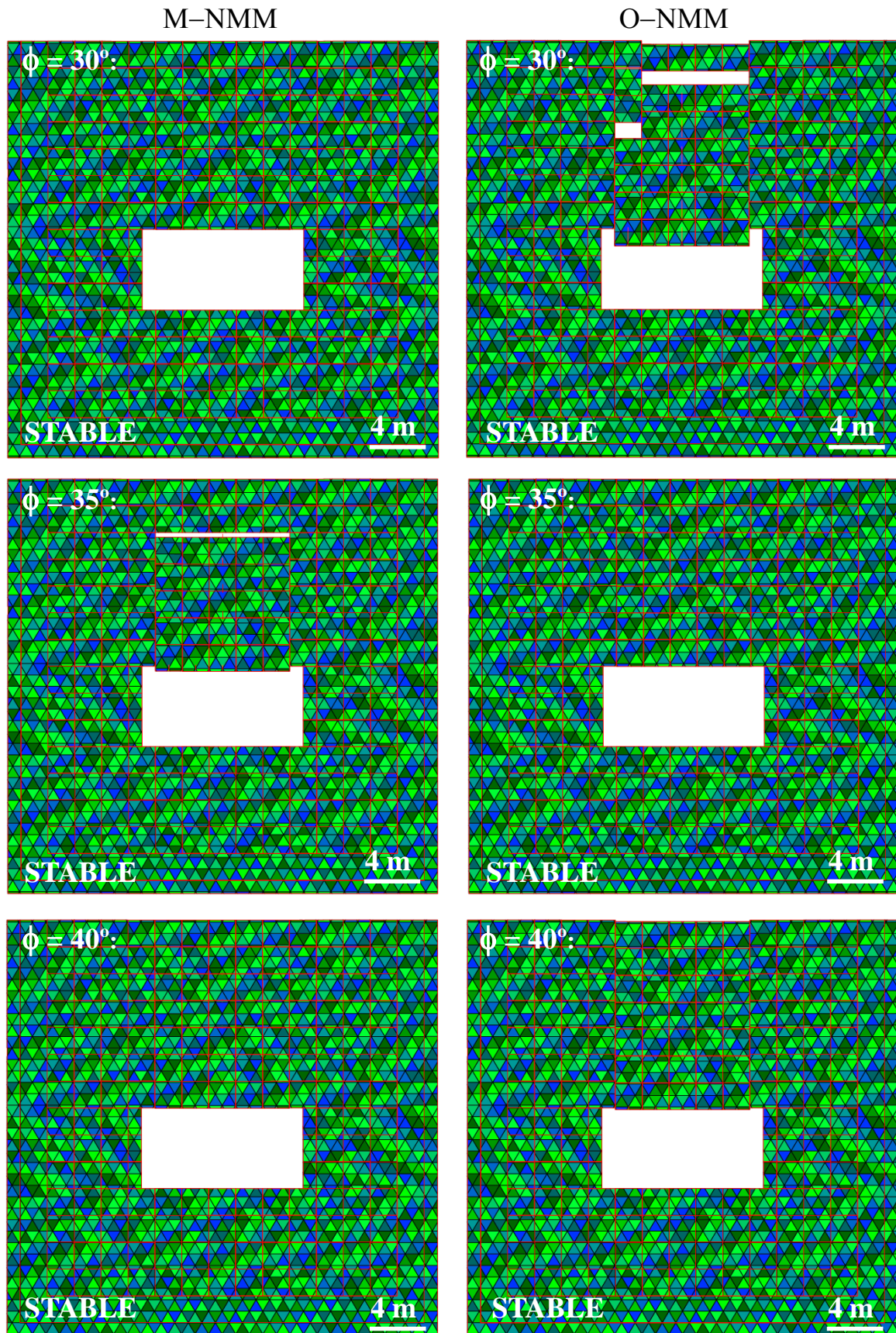


Figure 4.11(cont.). The analyzed opening at the end of the modified NMM simulations (left hand side), and at the end of the original NMM simulations (right hand side) for friction angles of 10° , 15° , 20° , 25° , 30° , 35° and 40° .

4.3.2 Analysis of a single block behavior during the simulation

At the previous section, the behavior of the whole blocky rock mass is analyzed. At this section, the behavior of the central block of the underground opening crown is analyzed. The modified NMM simulation with friction angle of $\phi = 30^\circ$ is applied again with two measurement points located at the upper part and at the lower part of the analyzed block. The horizontal stresses, vertical stresses and vertical displacements are recorded during the simulation. Figure 4.12 shows the analyzed domain at the end of the simulation with location of the specific analyzed block and the two measurement points. Inspection of the stress distribution (delineated in red) reveals that arching mechanism takes place in the roof of the underground opening.

Figure 4.13 shows the horizontal stresses at the two measurement points during the simulation. During the static stage (before the excavation), the block is subjected to compressive horizontal stresses which increase until they stabilize at values of 65 *KPa* at the upper part of the block and 80 *KPa* at the lower part of the block after 3 *s*. After the excavation ($t = 5$ *s*), the horizontal stress at the upper part of the block increases until it stabilizes on value of 1410 *KPa*. However, at the lower part of the block, the horizontal stress decreases and turns into tension of 122 *KPa*.

Although a comprehensive research on the behavior of a vertically jointed crown during the excavation is beyond the scope of this thesis, analysis of the horizontal stress distribution in the central block in the context of its neighboring blocks behavior (Figure 4.14) is performed in order to explain the obtained tensile stresses at the lower part of the block. The neighboring blocks undergo rotation inwards towards the center of the crown. Consequently, the central block undergoes 0.3 mm shortening at its upper part (Figure 4.14). Similarly to the Voussoir beam (Diederichs and Kaiser, 1999) and the multiple joint beam (Talesnick et al., 2007) a compressive arch evolves at the crown, and the central block is subjected to compressive loads at the upper part of its interfaces with the neighboring blocks. Because those loads are not completely horizontal and include also a small vertical component, the central block is subjected to moments which produce tensile stress and extension (0.03 mm) at its lower part.

Figure 4.15 shows the vertical stresses at the two measurement points during the simulation. During the static stage, the block is subjected to compressive vertical stresses which increase until they stabilize at values of 295 *KPa* at the upper part of the block and 340 *KPa* at the lower part of the block after 3 *s*. After the excavation, the vertical stresses at both parts of the block decrease. At the lower part of the block, near the free surface which is

created due to the excavation, the vertical stress is -8 KPa , while at the upper part of the block, the vertical stress is equal to -60 KPa .

Figure 4.16 shows the vertical displacements at the two measurements point during the simulation. During the static stage, small elastic deformations occur, with increasing vertical displacements in both parts of the block until a value of about 0.85 mm at $t = 2.5 \text{ s}$. After the excavation, the block undergoes an immediate settlement of 9 mm , and then it stabilizes with no additional displacements until the end of the dynamic stage.

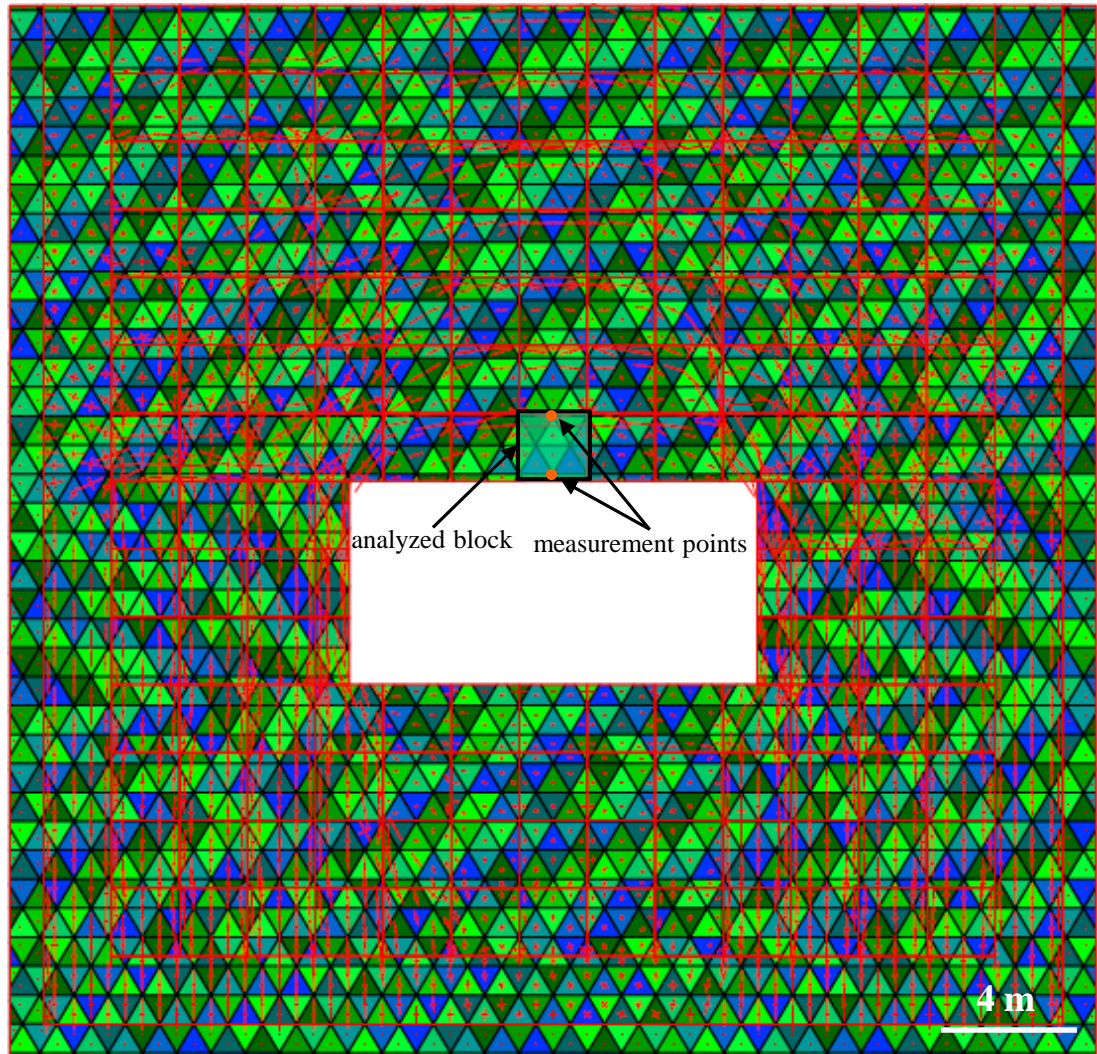


Figure 4.12. The modified NMM model at the end of the simulation with the locations of the analyzed block, and the two measurement points. Typical stress distribution result with scaled principal stress trajectories delineated in red.

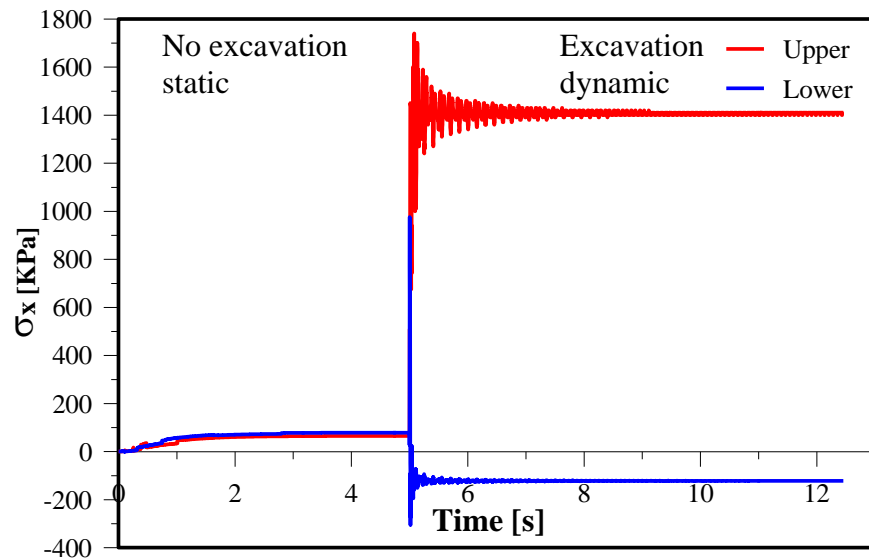


Figure 4.13. Horizontal stresses at the upper (red) and lower (blue) measurement points as a function of time for simulation with friction angle of $\phi = 30^\circ$ at all discontinuities.

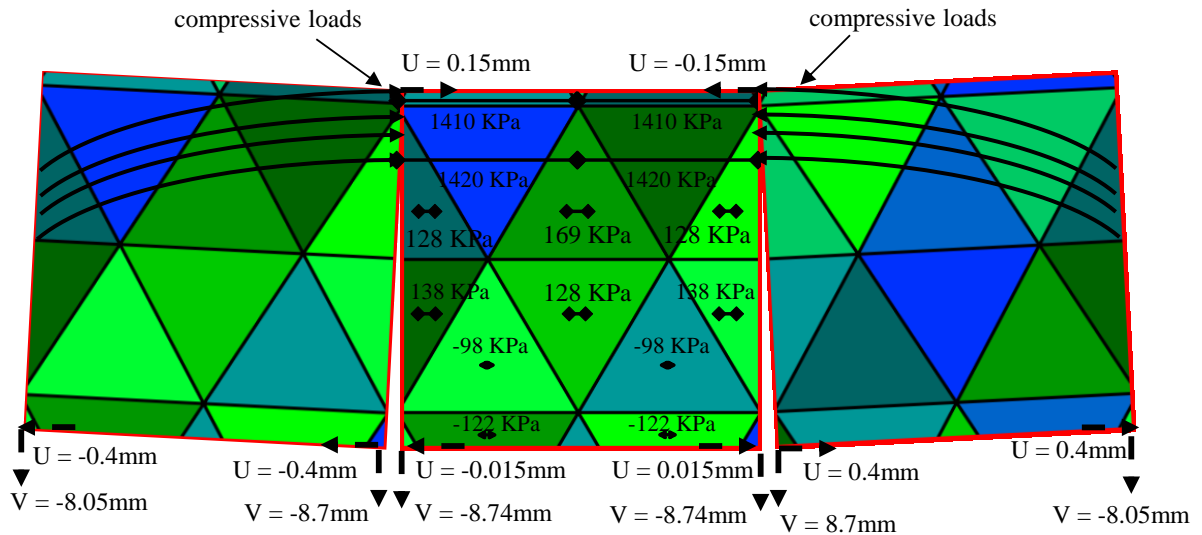


Figure 4.14. Analysis of the three central blocks of the crown at the end of the simulation, including: horizontal stresses distribution and displacements at the central block, and displacements at the lower part of its neighboring blocks.

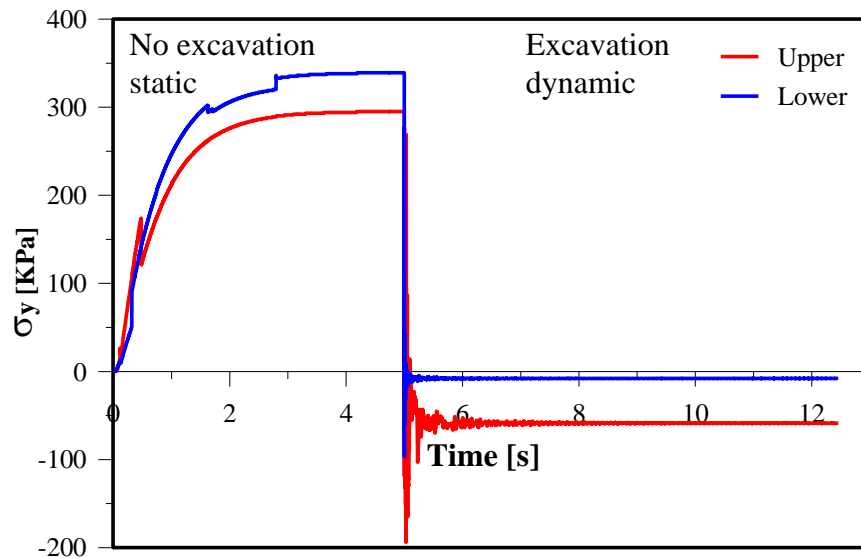


Figure 4.15. Vertical stresses at the upper (red) and lower (blue) measurement points as a function of time for simulation with friction angle of $\phi = 30^\circ$ at all discontinuities.

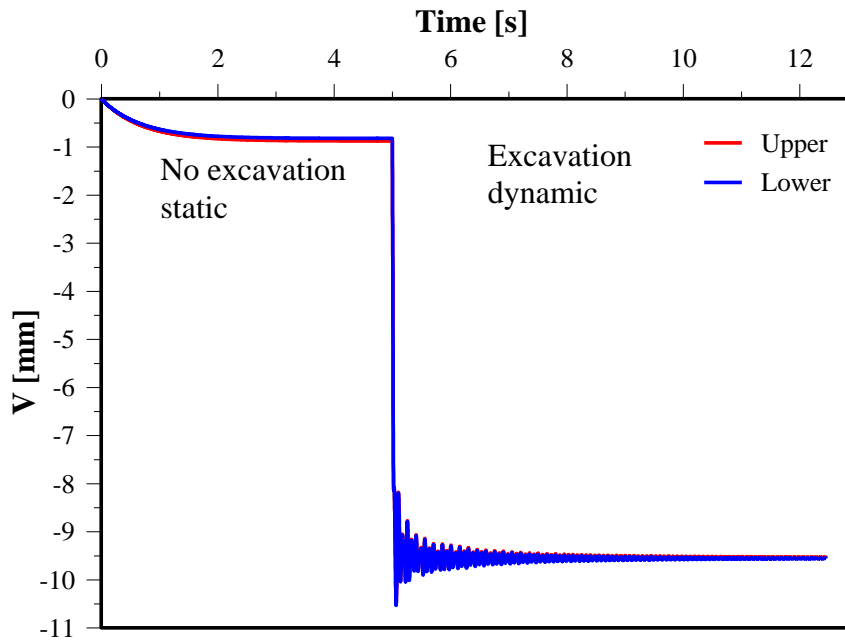


Figure 4.16. Vertical displacements at the upper (red) and lower (blue) points as a function of time for simulation with friction angle of $\phi = 30^\circ$ at all discontinuities.

4.4 Summary

The original NMM, where the underground opening is open from the beginning of the simulation, is limited when analyzing the stability of underground openings in blocky rock masses since local stresses do not exist yet. This limitation can lead to a wrong estimation of the stability of the underground opening, albeit, on the conservative side. The modified NMM solves this problem by allowing excavation during the simulation after the local stresses already exist and the elastic deformation has already occurred.

The importance of analyzing underground opening stability with the modified NMM, where the underground opening is excavated during the simulation, is demonstrated with an example of underground opening in a blocky rock mass. When analyzed with the modified NMM, the underground opening is stable when the discontinuities' friction angle is 15° and above. However, with the original NMM, stability is achieved only at friction angles of 30° and above. Analysis of the stresses in the central block of the underground opening crown during the simulation also demonstrates the importance of the new procedure. On the first stage of the simulation, the stresses reach to realistic values only after 2-3 s (8000-12000 time steps), and if the cavern would be opened earlier (and off course, if the cavern exist from the beginning of the simulation) the simulation would not reflect properly the real behavior of the rock mass during the excavation.

Chapter 5- The Zedekiah cave case study

The case of Zedekiah cave was previously analyzed with DDA by (Bakun-Mazor et al., 2009), based on field measurements and laboratory tests performed by (Eimermacher, 2004). Their results, based on 2D DDA modeling, showed that in the immediate roof of the cavern, a significant amount of vertical deflection (34 cm) is expected before stable arching is obtained, 3 s after the beginning of the simulation. A friction angle value of 41° was assumed for all discontinuities, and the analysis was performed under plane stress conditions.

In this study, the stability of Zedekiah cave is analyzed with the NMM under plane strain conditions which is a more appropriate boundary condition for modeling elongated underground openings such as the case of Zedekiah cave with a long axis two orders of magnitudes greater than the opening diameter. A comparison between the NMM and the modified NMM for a range of friction angle is performed to explore the relative significance of the excavation during the simulation procedure developed earlier in this thesis.

5.1 Site description

Zedekiah Cave has been used as an underground quarry below the city of Jerusalem from ca. 700 - 800 BC, and continuously until the end of the late Byzantine period, in order to extract high quality building stones for monumental constructions in Jerusalem and vicinity. The quarry is excavated underneath the old city of Jerusalem (Figure 5.1a) in a sub-horizontally bedded and moderately jointed, low strength, upper Cretaceous limestone of the Bina formation (Shadmaon, 1959). The underground quarry is 230 *m* long, with maximum width and height of 100 *m* and 15m respectively (Figure 5.1b).

The most striking feature of the quarry is certainly the 30 *m* span, unsupported central chamber, locally known as the "Freemasons Hall", because of ritual ceremonies taken place at the chamber by Freemasons in recent times (Figure 5.1c). Site investigations revealed that large roof slabs in several side chambers have collapsed over the years, but that the roof of the Freemasons hall has remained intact.

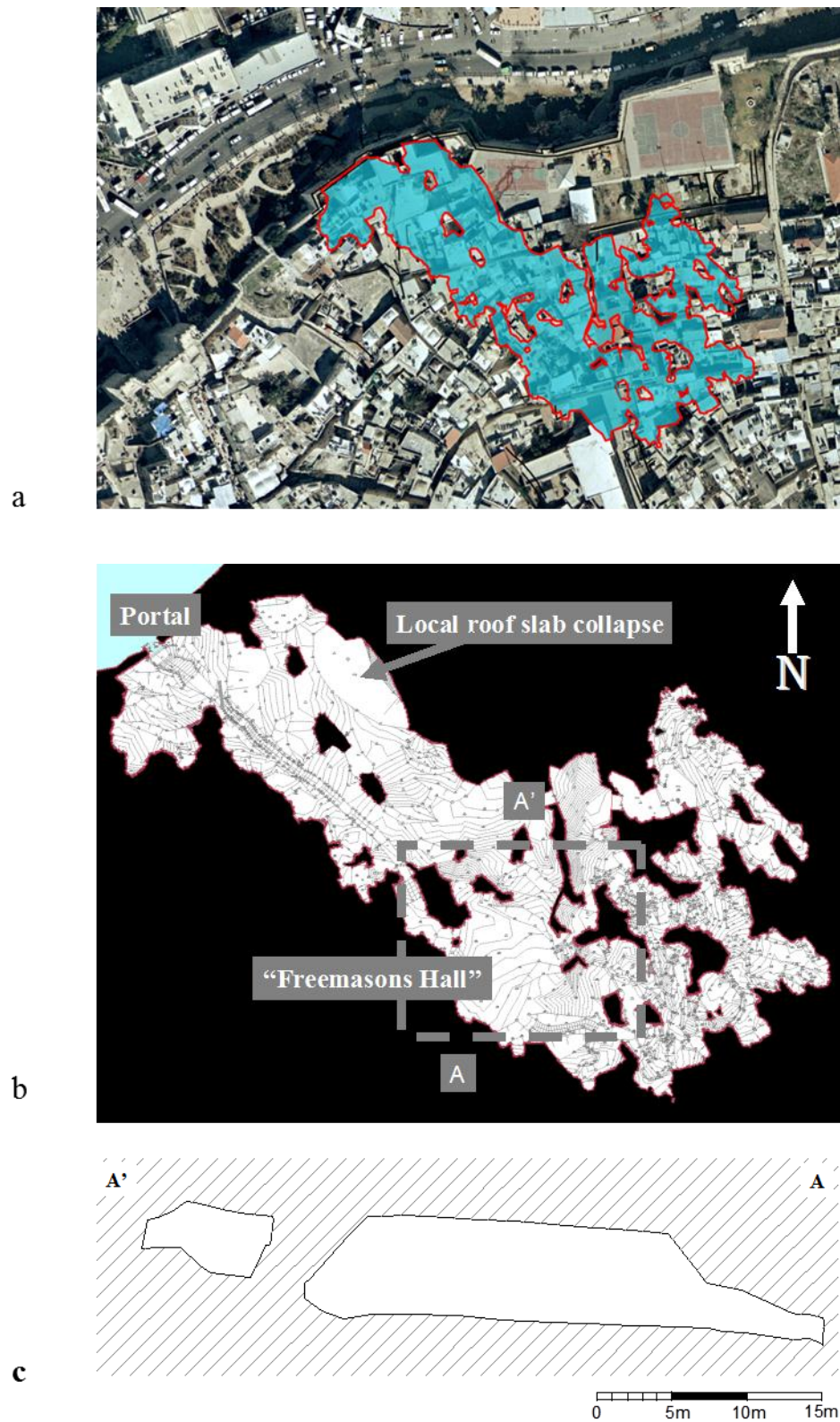


Figure 5.1. The 2000 year old cave of Zedekiah underneath the old city of Jerusalem. a) Layout of Zedekiah cave superimposed on the old city of Jerusalem, b) plan of Zedekiah cave, "Freemasons' Hall" delimited by dashed square, c) A cross section through Freemasons' Hall (after Eimermacher (2004)).

5.2 NMM model

The rock mass structure at Zedekiah cave consists of one set of sub-horizontal beds and three sets of inclined joints (Table 5.1). Since the NMM is restricted to a two-dimensional analysis, the fracture pattern has been simplified to two discontinuity sets: sub-vertical joints and horizontal bedding planes. The three sub-vertical joint sets are therefore replaced by a single representative vertical joint set with mean spacing of 1.5 *m*, trace length 8 *m*, and bridge length 0.2 *m*. Trace lines for the joint sets are generated synthetically by the line generation code of DDA (DL), in this case with a degree of randomness of 0.7 (for definition of the degree of randomness and the trace length generation algorithm employed in DL see Shi and Goodman 1989). Mesh generation is performed using the NMM cutting code (MC). Trace lines for the bedding planes are inserted manually to avoid undesired bedding plane locations, maintaining a mean bed thickness of 2 m in the mesh. The reason both joint set and bedding plane spacing is larger in the mesh than in the field is our desire to minimize the total number of blocks which will be computed without compromising on geometrical block characteristics. The resulting NMM mesh is therefore, to some extent, an idealized picture of the rock mass in the field with a smaller number of individual blocks than in reality. Careful examination of the "Freemasons' Hall" NMM model (Figure 5.2) reveals that discontinuity tips also exist. On the contrary to the DDA, the NMM cutting code (MC) allows the existence of discontinuity tips. However, those tips must be ended at the boundary of an element. An illustration of the differences between the DDA and the NMM cutting codes for the same data input is shown in (Figure 5.3).

Table 5.1. Rock mass structure at Zedekiah cave (after Eimermacher (2004))

Discontinuity set	Genetic type	Mean orientation	Mean spacing (m)
1	Bedding	08/091	0.85
2	Shears	71/061	0.79
3	Shears	67/231	1.48
4	Joints	75/155	1.39

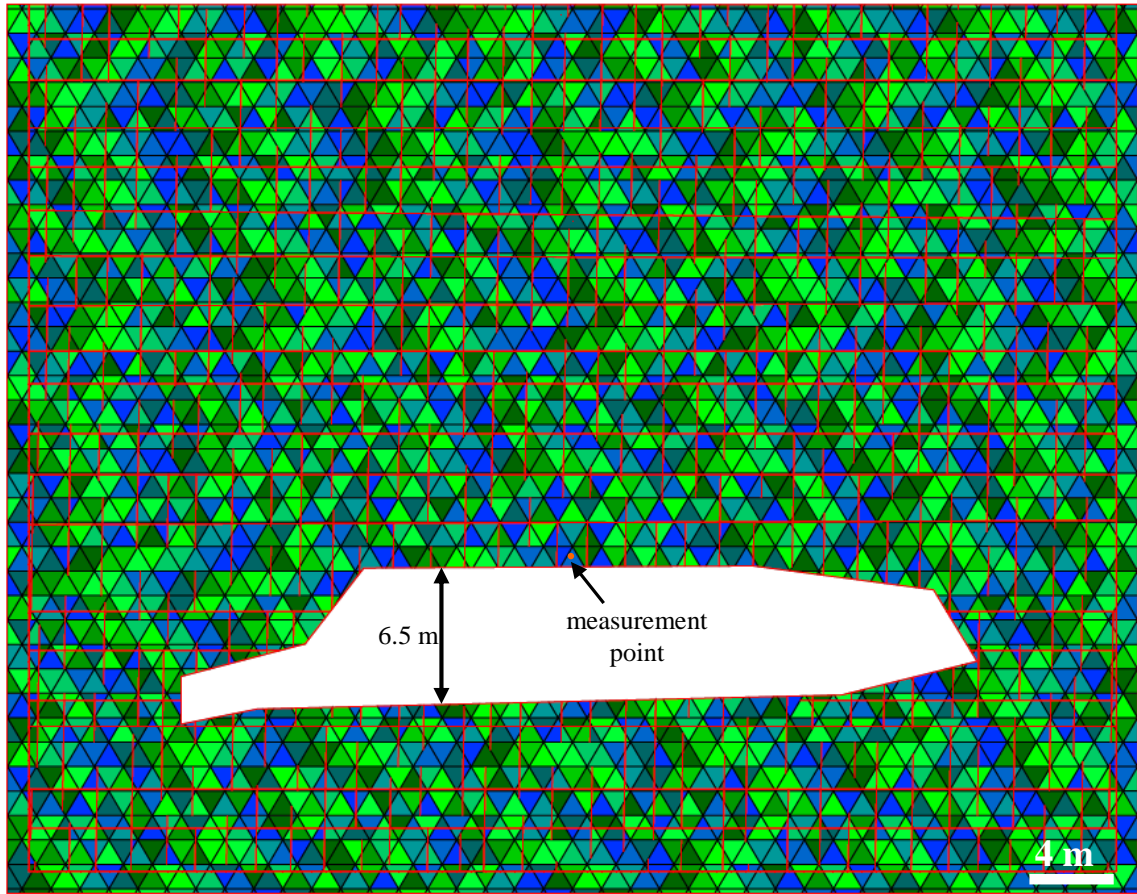


Figure 5.2. NMM model of the "Freemasons' Hall"

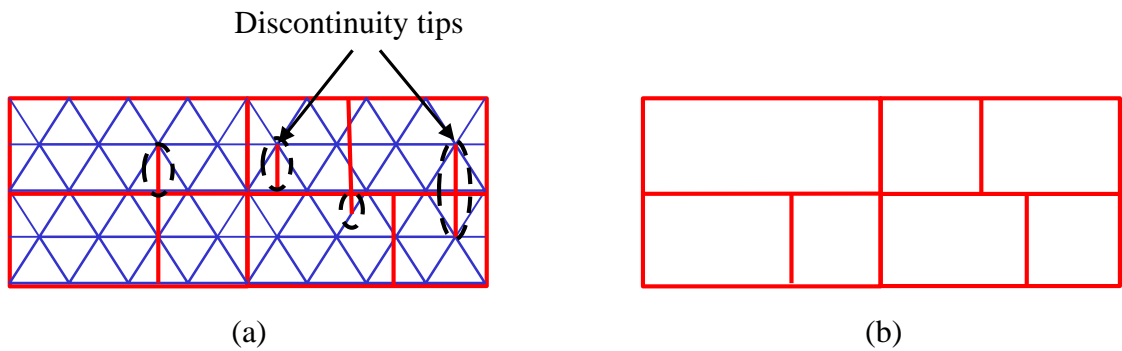


Figure 5.3. a) Schematic illustration of discontinuity tips in NMM mesh; and b) DDA mesh which were generated with the same input data.

5.3 NMM simulations

The stability of the "Freemasons' Hall" under gravitational loading is examined with both original NMM and modified NMM. In both methods, the duration of the dynamic simulations is 7.5 *s*, an equivalent of 30,000 NMM time steps ($g_1 = 0.00025$ *s*). The static stage in the modified NMM (before the excavation) lasts also 7.5 *s*. The spring's stiffness (g_0) and the assumed maximum displacement ratio (g_2) are identical to those chosen in Chapter 4-. The mechanical and numerical parameters in the simulations are presented in Table 5.2.

Table 5.2. Input parameters for NMM analysis of Freemasons' Hall in Zedekiah cave, Jerusalem

$K01$	$g2$	$g1$ [s]	$g0$ [kN/m]	e	E [GPa]	ν	γ [kN/m ³]
1	0.0001	0.00025	50000000	20	10	0.184	24.5

5.3.1 Friction angle value of 41°

Two simulations, one with the original and other with the modified NMM, are performed with friction angle value of 41° in all discontinuities based on tilt tests of saw cut planes and measured joint surface profiles in the field (Eimermacher, 2004). The cavern at the end of the 2 simulations with scaled principal stress trajectories delineated in red is shown in Figure 5.4. Inspection of the figure reveals that arching mechanism is obtained after small initial vertical deflection of the immediate roof: 7.5 *cm* in the original NMM simulation, and 3.8 *cm* in the modified NMM simulation. In both methods six blocks at the left side of the cavern and one small block at the right side of the cavern fall from the roof. Those blocks cannot remain attached in two dimensions analysis due to their initial configuration.

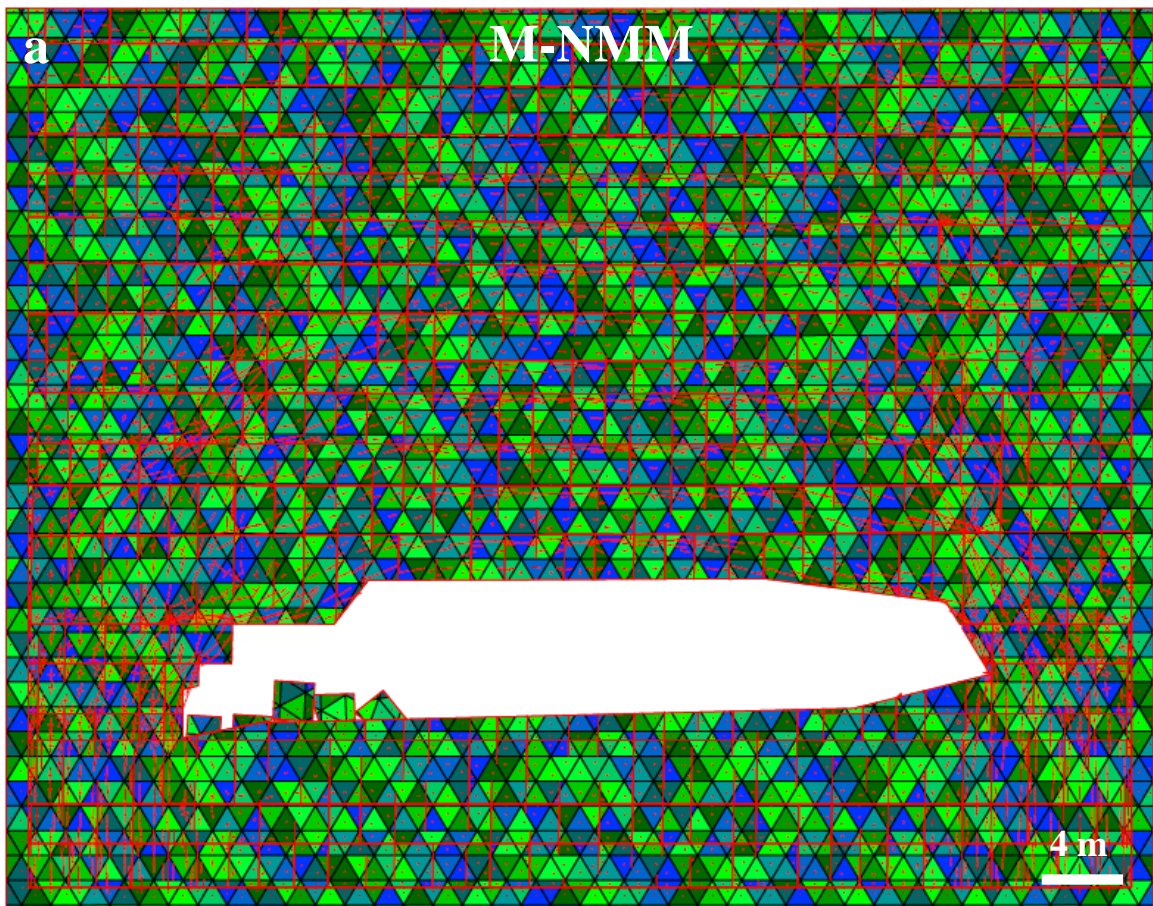


Figure 5.4. The "Freemasons' Hall" model at the end of the modified NMM simulations (a), and at the end of the original NMM simulations (b). Typical stress distribution result with scaled principal stress trajectories delineated in red.

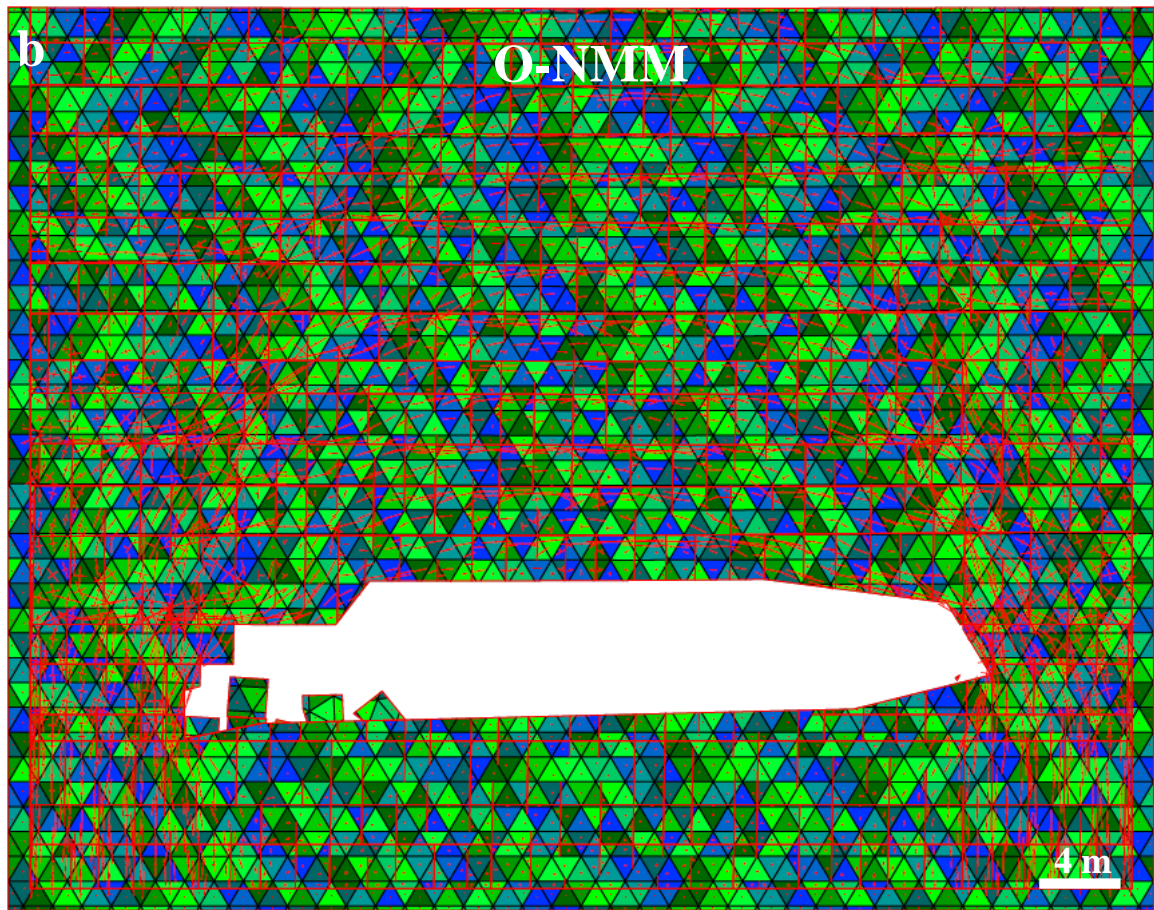


Figure 5.4 (cont.). The "Freemasons' Hall" model at the end of the modified NMM simulations (a), and at the end of the original NMM simulations (b). Typical stress distribution result with scaled principal stress trajectories delineated in red.

5.3.2 Required friction angle for stability

The assumed value of friction angle based on tilt tests of saw-cut planes and a measured joint surface profile in the field is not very accurate. Therefore, the stability of the "Freemasons' Hall" under gravitational loading is also examined with original and modified NMM for a range of assumed friction angles. This examination also enabled the comparison between the original and modified NMM in a real case study.

Eight simulations (four for each method) are performed with assumed friction angle values of 10° , 15° , 20° and 25° . The NMM models at the end of the 8 simulations are shown in Figure 5.5. The modified NMM simulations are presented at the left hand side, and original NMM simulations are presented at the right hand side. For a friction angle of 10° , the cavern is not stable in both methods: with original NMM the immediate roof and the layer above it falls, whereas with modified NMM only the immediate roof collapses. With an assumed friction angle of 15° the cavern is stable when analyzed with modified NMM with immediate roof deflection of 15 cm but with the original NMM the immediate roof collapses. With an

assumed friction angle of 20° the cavern is stable when analyzed with modified NMM with immediate roof deflection of 7 cm . With the original NMM, the deflection of the immediate roof is 17.7 cm after 7.5 s . However, careful examination of the deflection of the roof as a function of the time (Figure 5.6) during the simulation reveals that the roof is not completely stable at the end of the simulation, with a continuous increase of roof deflection. A continuous increase of roof deflection is obtained also when the same simulation is performed for 16 s , with roof deflection of 31.5 cm at the end of the simulation. Therefore, the cavern is defined as unstable for this friction angle. With an assumed friction angle of 25° the cavern is stable with both methods. The deflection of the immediate roof is 5 cm in the original NMM simulation, and 6.1 cm in the modified NMM simulation.

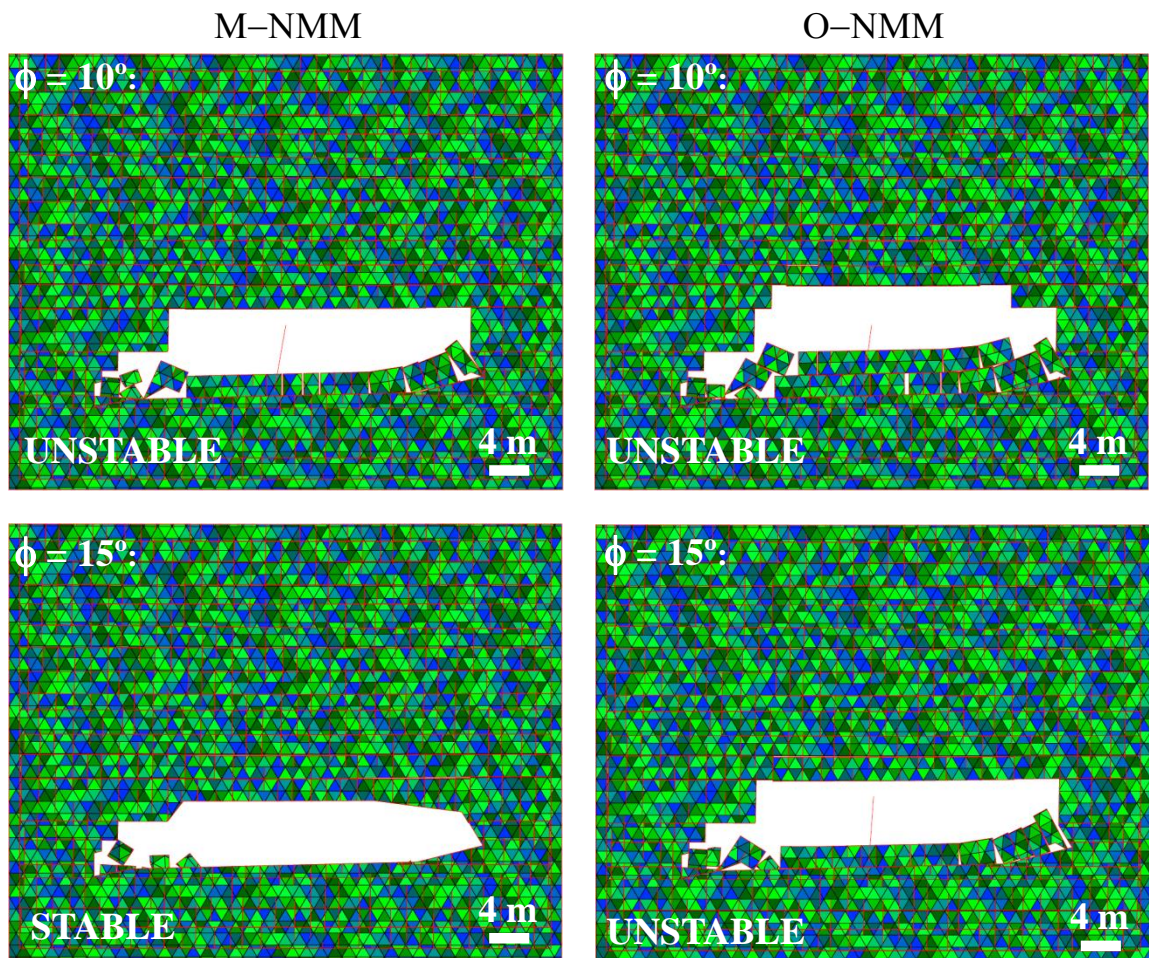


Figure 5.5. The "Freemasons' Hall" model at the end of the modified NMM simulations (left hand side), and at the end of the original NMM simulations (right hand side) for friction angles of 10° , 15° , 20° and 25° .

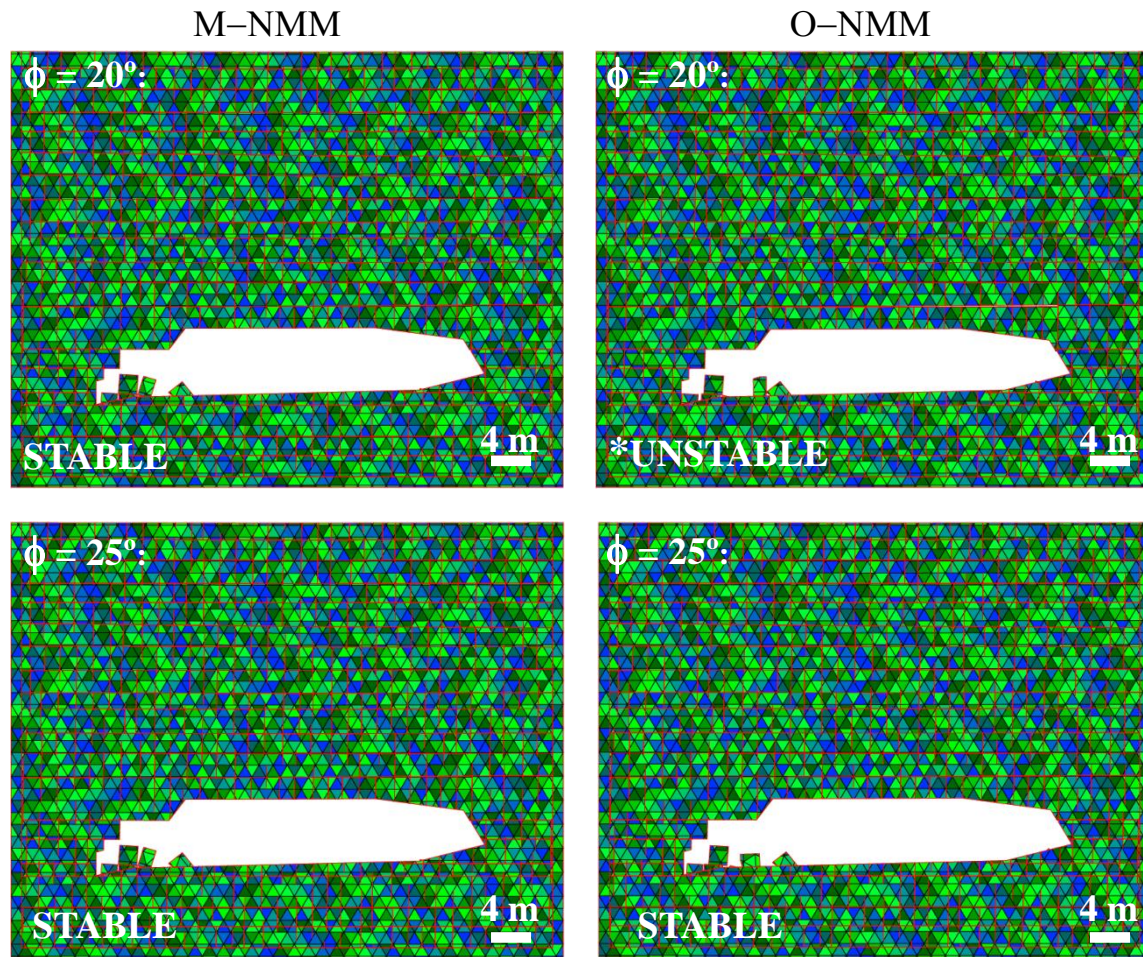


Figure 5.5 (cont.). The "Freemasons' Hall" model at the end of the modified NMM simulations (left hand side), and at the end of the original NMM simulations (right hand side) for friction angles of 10° , 15° , 20° and 25° .

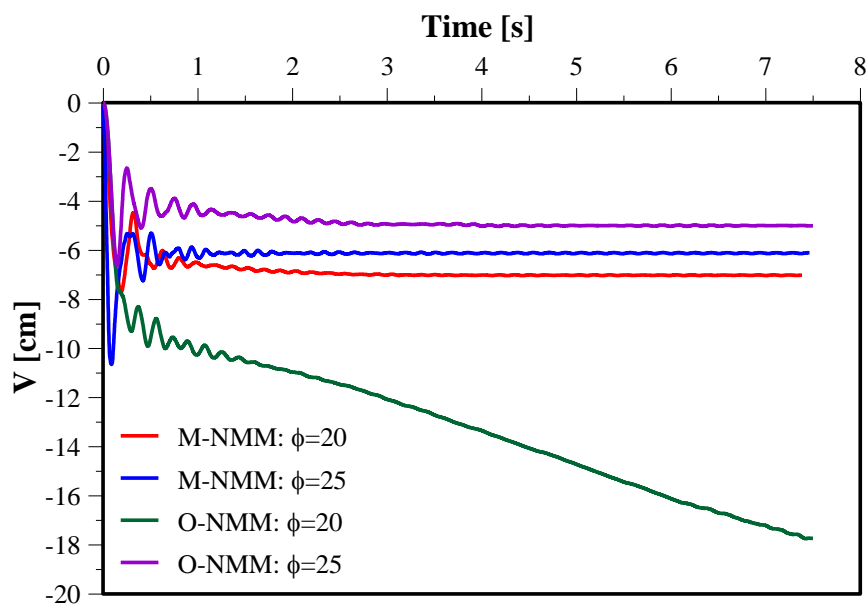


Figure 5.6. Roof deflection as a function of time during modified (the graph represents only the second dynamic stage) and original NMM simulations, for friction angles of, 20° and 25° .

5.4 Summary

Stability analysis of the “Freemasons hall” at Zedekiah cave with modified and original NMM reveals that the cavern is stable for the friction angle value obtained experimentally. The stability is attributed to the arching mechanism that develops in the layers of the immediate roof which are comprised of small, prismatic, blocks. These numerical results are supported by the fact that the roof of “Freemasons hall” has remained intact and un-supported since its excavation more than 2000 years ago. Moreover, the cavern is stable when analyzed with the modified and original NMM also for significantly smaller values of friction angles: 15° when analyzed with the modified NMM, and 25° when analyzed with the original NMM. This observation strengthens the conclusion that “Freemasons hall” is stable.

Chapter 6- Discussion and conclusions

This research focuses on the application and modification of the numerical manifold method (NMM) for the purpose of enhancing the analysis capability of underground openings embedded in discontinuous rock masses. As a hybrid method between numerical methods from the continuum (FEM) and discontinuum (DDA) approaches, the NMM is capable of modeling dynamic problems involving the interaction of multiple blocks including the stress distribution and deformations inside those blocks.

6.1 Verification and calibration of the NMM

The capability of the NMM to solve stresses and displacements in a continuous elastic medium is verified using three static problems: 1) a layered plate subjected to gravity, where the NMM is found capable of modeling problems which involve inhomogeneous (layered) media; 2) circular hole in an infinite plate subjected to remote constant stresses (Kirsch solution) where the capability of the NMM to model problems which involve stress concentrations is verified; and 3) in the case of beam under a concentrated load and volumetric force, the NMM suitability for solving problems which involve bending is checked. Generally, a good agreement between the NMM and the analytical solutions is obtained, with higher accuracy of the NMM solution for the displacements than its solution for the stresses.

The NMM uses linear displacement functions for its elements. Therefore, in cases where stresses change rapidly (e.g. the immediate region around the hole in Kirsch solution and along the beam under concentrated load and volumetric force), NMM results nicely follow the analytical solution for stresses, but a relatively dense mesh of elements is required in order to solve the stress distribution accurately. However, it is important to note that the NMM (this research as well) aims for complex problems where the displacement field is dominated by displacements along discontinuities rather than stresses and deformation in the continuous medium.

The NMM capability of modeling the interaction between blocks is tested using the case of dynamic sliding of a block on an inclined plane. In this verification, the influence of the spring's stiffness (g_0), time step size (g_1), and the assumed maximum displacement per time step ratio (g_2) on the NMM results is examined. For all time step sizes below $g_1 = 0.01$ s, a very good agreement between the NMM and analytical solution is obtained, without dependence on the numerical control parameters g_0 and g_2 . For the case of $g_1 = 0.01$ s, the relative errors are much higher and range from 5 % to 10 %. It is important to note, however,

that this verification is important as general benchmark tests for NMM, but its applicability to underground openings analysis is limited because it involves the interaction between only two blocks and it is performed under small stresses.

Analysis of underground openings in blocky rock masses demands careful selection of the numerical control parameters. The size of the time step should be chosen small enough to allow small displacements in a single time step without causing exceedingly long simulations. It is found that the spring stiffens should be chosen at least 5 times larger than the Young's modulus of the analyzed material. Otherwise, the stresses computed by NMM are underestimated, while the displacements computed by NMM are over-estimated. It is found also that for the chosen time step size in this thesis ($g1 = 0.00025 \text{ s}$), minimum number of open-close iterations before convergence of the numerical solution and the minimum CPU time are obtained for assumed maximum displacement ratio of $g2 = 0.0001$ and spring's stiffens of $g0 = 50000000 \text{ kN/m}$ (5 times larger than the Young's modulus). These findings can be used as guidelines for future NMM users.

6.2 Simulating the excavation sequence with NMM

In this work the original NMM is modified in order to improve its capability of analyzing the stability of underground openings in blocky rock masses. An algorithm for a two-stage procedure is implemented into the NMM code in order to allow tunnel excavation (second stage) during the NMM simulation, after the local stresses in the medium already exist and the medium has already experienced elastic deformation due to overburden stress (first stage). The validity of the modified NMM code is verified using the case of Kirsch solution.

The importance of analyzing underground opening stability in blocky rock masses with the modified NMM, where the underground opening is excavated during the simulation rather than the original NMM, where the underground opening is open from the beginning of the simulation, is demonstrated with an example of rectangular underground opening embedded in horizontally stratified and vertically jointed rock mass. The original NMM proves to be very conservative compared with the modified NMM: When analyzed with the original NMM, the underground opening is stable when the friction angle of all discontinuities is 30° and above. However, with the modified NMM, stability is achieved for friction angle of 15° and above.

An analysis of central block in the cavern crown during a modified NMM simulation with discontinuity friction angle of 30° also demonstrates the importance of the new procedure. During the static stage (before the excavation), the horizontal compressive stresses

evolve slowly and reach to realistic value which can reflect properly a real excavation process only after 2-3 s (8000-12000 time steps). After the excavation the compressive horizontal stresses increase significantly in the upper region of the block while at the lower part of the block small tensile stresses are obtained as part of global arching mechanism and rotation of neighboring blocks which stabilize the crown of the cavern.

The original and modified NMM are applied in this thesis to analyze the stability of the 30 m wide “Freemasons hall” at Zedekiah cave which is embedded in a blocky rock mass. When analyzed with friction angle value of 41° in all discontinuities, the rock mass above the cavern attains stable arching (except for six blocks which fall in the sides) after significantly smaller initial vertical deflection of the immediate roof than is obtained in previous simulation with DDA: 7.5 cm with the original NMM and 3.8 cm with the modified NMM compared with 34 cm in DDA simulation. This result demonstrates the importance of the NMM approach when the analyzed rock mass contains blocks with different sizes, some of them with one dimension much larger than the other. However, it is important to note that the NMM simulations are performed under plane strain boundary condition, while the DDA simulations were performed under plane stress boundary condition.

Stability analysis of the “Freemasons hall” with significantly smaller values of friction angles strengthens the conclusion that the cavern in its current configuration is stable. The difference between the modified and original NMM results for this case is less drastic than in the previous case but still significant: with the modified NMM the cavern is stable when the discontinuities’ friction angle is 15° and above, while with the original NMM the cavern is stable when the discontinuities’ friction angle is 25° and above.

6.3 Recommendations for further research

The main contribution of this research is the improvement of the NMM capability of modeling the behavior of underground openings in blocky rock masses. Future research can use this improvement to study the general behavior of underground openings embedded in blocky rock mass with respect to parameters such as joint spacing and orientation, elastic constants, cavern span, etc.

In this research the NMM is verified using relatively simple problems which have analytical solutions. In future research the validation of NMM should be performed under more complex conditions, using experimental models such as the centrifuge model used by Tsesarsky and Talesnick (2007) for DDA validation, or real case studies where the rock mass deformation due to excavation is monitored and documented.

References

- An, X.M., 2010, Extended numerical manifold method for engineering failure analysis: Nanyang, Nanyang Technological University.
- Bakun-Mazor, D., Hatzor, Y.H., and Dershowitz, W.S., 2009, Modeling mechanical layering effects on stability of underground openings in jointed sedimentary rocks: *International Journal of Rock Mechanics and Mining Sciences*, v. 46, p. 262-271.
- Barton, N., Lien, R., and Lunde, J., 1974, Engineering Classification of Jointed Rock Masses for the Design of Tunnel Support: *Rock Mechanics*, v. 6, p. 189-236.
- Bieniawski, Z.T., 1973, Engineering Classification of Jointed Rock Masses, *Transaction of the South African Institution of Civil Engineers*, Volume 15, p. 335-344.
- , 1989, *Engineering Rock Mass Classifications*: New York, John Wiley & Sons, 251 p.
- , 1997, Quo vadis rock mass classifications?: *Felsbau*, v. 15, p. 177–178.
- Brady, B.H.G., and Brown, E.T., 1993, *Rock Mechanics for Underground Mining*: London, Chapman and Hall.
- Chen, G.Q., Ohnishi, Y., and Ito, T., 1998, Development of high-order manifold method: *International Journal for Numerical Methods in Engineering*, v. 43, p. 685-712.
- Cheng, Y., Li, S., and Wu, Y.F., 2005, Numerical manifold method based on the method of weighted residuals: *Computational Mechanics*, v. 35, p. 470-480.
- Cheng, Y.M., and Zhang, Y.H., 2008, Formulation of a three-dimensional numerical manifold method with tetrahedron and hexahedron elements: *Rock Mechanics and Rock Engineering*, v. 41, p. 601-628.
- Cheng, Y.M., Zhang, Y.H., and Chen, W.S., 2002, Wilson non-conforming element in numerical manifold method: *Communications in Numerical Methods in Engineering*, v. 18, p. 877–884.
- Chikahisa, H., Kobayashi, K., Matsumoto, K., M., T., and Ohnishi, Y., 1997, Geological survey for DDA and its application to a large rock cavern, *The Second International Conference on Analysis of Discontinuous Deformation*: Kyoto, Japan.
- Chiou, Y.J., Lee, Y.M., and Tsay, R.J., 2002, Mixed mode fracture propagation by manifold method: *International Journal of Fracture*, v. 114, p. 327-347.
- Cundall, P.A., 1971, A computer model for simulating progressive, large scale movements in blocky rock system, *Symposium of International Society of Rock Mechanics*: Nancy, France, p. 11-18.
- Desai, C.S., Zaman, M.M., Lightner, J.G., and Siriwardane, H.J., 1984, Thin-Layer Element for Interfaces and Joints: *International Journal for Numerical and Analytical Methods in Geomechanics*, v. 8, p. 19-43.
- Diederichs, M.S., and Kaiser, P.K., 1999, Stability of large excavations in laminated hard rock masses: the voussoir analogue revisited: *International Journal of Rock Mechanics and Mining Sciences*, v. 36, p. 97-117.
- Eimermacher, C., 2004, Stability of high span openings in discontinuous rock, case history: Zedekiah's cave - Jerusalem: Beer-Sheva, Ben-Gurion University of the Negev.

- Goodman, R.E., Taylor, R.L., and Brekke, T.L., 1968, A model for the mechanics of jointed rock Journal of the Soil Mechanics Division, v. ASCE 94, p. 637–659.
- Harrison, J.P., and Hudson, J.A., 2000, Engineering rock mechanics. Part 2: Illustrative worked examples: Oxford, Pergamon.
- Hatzor, Y.H., and Benary, R., 1998, The stability of a laminated Voussoir beam: Back analysis of a historic roof collapse using DDA: International Journal of Rock Mechanics and Mining Sciences, v. 35, p. 165-181.
- Hatzor, Y.H., Wainshtein, I., and Bakun Mazor, D., 2010, Stability of shallow karstic caverns in blocky rock masses: International Journal of Rock Mechanics and Mining Sciences, v. 47, p. 1289-1303.
- He, L., and Ma, G.W., 2010, Development of 3d Numerical Manifold Method: International Journal of Computational Methods, v. 7, p. 107-129.
- Jiang, Q.H., Zhou, C.B., and Li, D.Q., 2009, A three-dimensional numerical manifold method based on tetrahedral meshes: Computers & Structures, v. 87, p. 880-889.
- Jing, L., 2003, A review of techniques, advances and outstanding issues in numerical modelling for rock mechanics and rock engineering: International Journal of Rock Mechanics and Mining Sciences, v. 40, p. 283-353.
- Kamai, R., and Hatzor, Y.H., 2008, Numerical analysis of block stone displacements in ancient masonry structures: A new method to estimate historic ground motions: International Journal for Numerical and Analytical Methods in Geomechanics, v. 32, p. 1321-1340.
- Katona, M.G., 1983, A Simple Contact Friction Interface Element with Applications to Buried Culverts: International Journal for Numerical and Analytical Methods in Geomechanics, v. 7, p. 371-384.
- Kirsch, G., 1898, Die theorie der elastizitat und die bedurfnisse der festigkeitslehre: Veit. Ver. Deut. Ing., v. 42, p. 797-807.
- Ma, G.W., An, X.M., and He, L., 2010, The Numerical Manifold Method: A Review: International Journal of Computational Methods, v. 7, p. 1-32.
- Miki, S., Sasaki, Y., Ohnishi, Y., and Nishiyama, S., 2007, Application of manifold method to geotechnical problems involving excavations, Proceedings of the eighth international international conference on Analysis of Discontinuous Deformation (ICADD-8): Beijing, China p. 275-280.
- Riedmüller, G., and Schubert, W., 1999, Critical comments on quantitative rock mass classifications: Felsbau, v. 17, p. 164-167.
- Shadmaon, A., 1959, The Bi'na limestone, in Bulletin 24: Jerusalem, Geological Survey of Israel.
- Shi, G.H., 1988, Discontinuous Deformation Analysis – a new numerical method for the statics and dynamics of block system: Berkley, University of California.
- , 1996a, Manifold method, Proceedings of the first international forum on discontinuous deformation analysis (DDA) and simulations of discontinuous media: Albuquerque, New Mexico, USA, TSI Press, p. 52-204.
- , 1996b, Simplex integration for manifold method, FEM, DDA and analytical analysis, Proceedings of the first international forum on discontinuous deformation analysis (DDA) and simulations of discontinuous media: Albuquerque, New Mexico, USA, TSI Press, p. 205-262.

- Talesnick, M.L., Bar Ya'acov, N., and Cuitoro, A., 2007, Modeling of a multiply jointed Voussoir beam in the centrifuge: *Rock Mechanics and Rock Engineering*, v. 40, p. 383-404.
- Tsay, R.J., Chiou, Y.J., and Chuang, W.L., 1999, Crack growth prediction by manifold method: *Journal of Engineering Mechanics-Asce*, v. 125, p. 884-890.
- Tsesarsky, M., and Hatzor, Y.H., 2006, Tunnel roof deflection in blocky rock masses as a function of joint spacing and friction - A parametric study using discontinuous deformation analysis (DDA): *Tunnelling and Underground Space Technology*, v. 21, p. 29-45.
- Tsesarsky, M., and Talesnick, M.L., 2007, Mechanical response of a jointed rock beam - Numerical study of centrifuge models: *International Journal for Numerical and Analytical Methods in Geomechanics*, v. 31, p. 977-1006.
- Wu, J.H., Ohnishi, Y., and Nishiyama, S., 2004, Simulation of the mechanical behavior of inclined jointed rock masses during tunnel construction using Discontinuous Deformation Analysis (DDA): *International Journal of Rock Mechanics and Mining Sciences*, v. 41, p. 731-743.
- Zhang, H.H., Li, L.X., An, X.M., and Ma, G.W., 2010, Numerical analysis of 2-D crack propagation problems using the numerical manifold method: *Engineering Analysis with Boundary Elements*, v. 34, p. 41-50.
- Zienkiewicz, O.C., Best, B., Dullage, C., and Stagg, K., 1970, Analysis of nonlinear problems in rock mechanics with particular reference to jointed rock systems, *Proceedings of the Second International Congress on Rock Mechanics Belgrade, Yugoslavia*.